United Arab Emirates University
Scholarworks@UAEU

Dissertations | Electronic Theses and Dissertations

3-2022

RADAR REMOTE SENSING FOR LAND SURFACE STUDIES OVER THE UNITED ARAB EMIRATES

Muhagir Hisham Elkamali

Follow this and additional works at: https://scholarworks.uaeu.ac.ae/all_dissertations

 Part of the Geography Commons

جامعة الإمارات العربية المتحدة
United Arab Emirates University

DOCTORATE DISSERTATION NO. 2022: 1

College of Humanities and Social Sciences

Department of Geography and Urban Sustainability

RADAR REMOTE SENSING FOR LAND SURFACE STUDIES OVER THE UNITED ARAB EMIRATES

Muhagir Hisham Hashim Elkamali

March 2022

United Arab Emirates University

College of Humanities and Social Sciences

RADAR REMOTE SENSING FOR LAND SURFACE STUDIES OVER THE UNITED ARBA EMIRATES

Muhagir Hisham Hashim Elkamali

This dissertation is submitted in partial fulfillment of the requirements for the degree of Doctor of Philosophy

Under the Supervision of Dr. Abdelgadir Abuelgasim

March 2022

Declaration of Original Work

I, Muhagir Hisham Hashim Elkamali, the undersigned, a graduate student at the United Arab Emirates University (UAEU), and the author of this dissertation entitled "*Radar Remote Sensing for Land Surface Studies over the United Arab Emirates*", hereby, solemnly declare that this dissertation is my own original research work that has been done and prepared by me under the supervision of Dr. Abdelgadir Abuelgasim, in the College of Humanities and Social Sciences at UAEU. This work has not previously formed the basis for the award of any academic degree, diploma or a similar title at this or any other university. Any materials borrowed from other sources (whether published or unpublished) and relied upon or included in my dissertation have been properly cited and acknowledged in accordance with appropriate academic conventions. I further declare that there is no potential conflict of interest with respect to the research, data collection, authorship, presentation, and/or publication of this dissertation.

Student's Signature:  Date: 18-03-2022

Copyright © 2022 Muhagir Hisham Hashim Elkamali
All Rights Reserved

Advisory Committee

1) Advisor: Abdelgadir Abuelgasim

Title: Associate Professor

Department of Geography and Urban Sustainability

College of Humanities and Social Sciences

2) Co-advisor: Hakim Saibi

Title: Professor

Department of Geosciences

College of Science

3) Member: Ala Aldahan

Title: Professor

Department of Geosciences

College of Science

4) Member: Constantinos Loupasakis

Title: Associate Professor

Name of organization: National Technical University of Athens, Greece

Approval of the Doctorate Dissertation

This Doctorate Dissertation is approved by the following Examining Committee Members:

1) Advisor (Committee Chair): Abdelgadir Abuelgasim
   Title: Associate Professor
   Department of Geography and Urban Sustainability
   College of Humanities and Social Sciences
   Signature  Date 18-03-2022

2) Member: Dalal Matar Alshamsi
   Title: Associate Professor
   Department of Geosciences
   College of Science
   Signature  Date 18-03-2022

3) Member: Nazmi Saleous
   Title: Associate Professor
   Department of Geography and Urban Sustainability
   College of Humanities and Social Sciences
   Signature  Date 18-03-2022

4) Member (External Examiner): Hatim Sherif
   Title: Professor
   Department of Civil and Evnironmental Engineering
   Institution: University of Texas at San Antonio
   Signature  Date 18-03-2022

This Doctorate Dissertation is accepted by:

Dean of the College of Humanities & Social Sciences: Professor Hassan Alnaboodah

Signature  Date 29/04/2022

Dean of the College of Graduate Studies: Professor Ali Al-Marzouqi

Signature  Date 29/04/2022

Copy ____ of ____

Abstract

This dissertation is concerned with the land surface deformations related to anthropogenic activities and how a monitoring strategy can be established for nationwide studies. The main objective of this dissertation is to study land surface fluctuations in regional and local scales over the dry semi-arid climate of the United Arab Emirates with the relation to subsurface layers mechanisms and groundwater dynamics. Radar Interferometry techniques have been developed to detect and monitor land surface movement from space with very high accuracy. This dissertation investigates the implementation of these techniques over highly decorrelated surfaces. The detected land surface movements have been correlated with groundwater and geophysical data. The study shows significant findings of various land surface subsidence zones with extensive subsidence over desert landcover. The study detected a maximum land surface subsidence rate over two distinctive zones of Remah and Al Wagan with a subsidence rate of -60 mm/year and -55 mm/year, respectively with an accuracy measurement of ±2 mm/year in the period between 2017 to 2021. Results from Radar Interferometry have been confirmed by field observations where clear signs for ground movement have been observed. This dissertation implements Radar Interferometry techniques using the parallelization concept which aims to reduce the processing time that is always challenging for Radar Interferometry processing. Also, this dissertation processed time-series of radar imageries to observe smaller ground movement with reliable accuracy. Moreover, this dissertation holds an integration between radar remote sensing and geophysical investigation which unveils a hidden relationship between ground motion from space and subsurface mechanisms. This dissertation shows that the land surface subsidence detected in the previous study by (Liosis et al., 2018) is still active and more severe than before. Also, land surface movement over new areas that are unknown before have been detected and fully investigated with ground truth data.

Keywords: Radar Interferometry, Synthetic Aperture Radar, Groundwater, Surface Subsidence, Microgravity, Big data.

Title and Abstract (in Arabic)

الإستشعار عن بعد بالرادار لدراسة سطح الأرض فوق الإمارات العربية المتحدة

الملخص

هذه الأطروحة تركز على دراسة تشوهات مستوى سطح الأرض و علاقته بالممارسات المختلفة للإنسان و كيفية وضع إستراتيجية لمراقبة تلك التغييرات على مستوى يشمل الدولة بأكملها. إن الغرض الأساسي من هذه الأطروحة هو دراسة تغيير مستوى سطح الأرض على المستوى المحلي و الإقليمي في المناخ الجاف و شبه الصحراوي لدولة الإمارات و علاقته مع آلية تغيير الطبقات تحت سطح الأرض و تغيير مستوى المياه الجوفية. اعتمدت الدراسة بصورة أساسية على تقنيات قياس التداخل بالانتثار عن طريق الرادار التي تتميز بدقة عالية جدا لكشف و مراقبة تغييرات الهبوط و الإرتفاع لمستوى سطح الأرض. هذه الاطروحة تختبر التطبيق العملي لهذه التقنيات على أماكن تتميز بعدم ثبات الانتثار. نتائج تغييرات الهبوط و الإرتفاع لمستوى سطح الأرض تم ربطها بيانات المياه الجوفية و الجيوفيزياء. هذه الدراسة وجدت نتائج مهمة لنطاقات هبوط سطح الأرض مع إكتشاف هبوط حاد لمستوى سطح الأرض لمنطقة صحراوية تتوسطها بعض المزارع. أقصى معدل هبوط كشفت عنه هذه الدراسة كان بمقدار -60 مم بالسنة بمعدل تغيير ± 2 مم بالسنة في الفترة بين عامي 2017 و 2021. النتائج المكتشفة تم تأكيدها بعمل مسح حقلي لمعاينة نطاقات الهبوط حيث تم رصد دلائل لهبوط مستوى سطح الأرض. في هذه الأطروحة تم معالجة المرئيات المسجلة عن طريق تقنية قياس التداخل بالانتثار عن طريق الرادار بإستخدام مفهوم الموازاة حيث يهدف لتقليل زمن المعالجة لعدد كبير من المرئيات و اللذي يعتبر عائقا و تحديا في معالجة مرئيات الرادار بتقنية قياس التداخل بالانتثارعن طريق الرادار. أيضا هذه الأطروحة تطرقت لطرق معالجة البيانات الكبيرة للمرئيات المسجلة عن طريق مجسات الرادار بهدف اكتشاف درجات هبوط سطح الأرض الصغيرة مع الحفاظ على الدقة العالية للنتائج. هذه الأطروحة أيضا تضم دمج لتقنيات الاستشعار عن بعد بالرادار و الجيوفيزياء، حيث ساعد هذا الدمج على التعرف على علاقات جديدة بين نتائج معالجة الاستشعار عن بعد و حركة الطبقات تحت سطح الأرض. هذه الدراسة توضح ايضا أن هبوط مستوى سطح الأرض اللذي تم اكتشافه في الدراسات السابقة ما يزال مستمرا و بإزدياد في معدل الهبوط. كما أنه تم اكتشاف مناطق جديدة لظاهرة الهبوط و الإرتفاع لمستوى سطح الأرض لم يتم الكشف عنها مسبقا و قد تم عمل دراسة تفصيلية حول تلك المناطق بالإستعانة بالبيانات الحقلية.

مفاهيم البحث الرئيسية: قياس التداخل للرادار، الرادار ذو الفتحة الإصطناعية، المياه الجوفية، هبوط سطح الأرض، مايكرو الجاذبية، البيانات الكبرى.

Acknowledgments

First, I am grateful to my advisor Dr. Abdelgadir Abuelgasim who guided me through these long years and advised me during the hard times. Many thanks go to my advising committee, Prof. Hakim Saibi and Prof. Ala Aldahan who helped me with their knowledge and encouraged me through the Ph.D. journey.

I would like to thank Dr. Ioannis Papoutsis and Dr. Constantinos Loupasakis for their consistent support and this work was not possible without both of them. Many thanks to the National Water and Energy Center for funding this study. Also, I would like the staff of the HPC unit at the United Arab Emirates University for their technical support.

I would like to thank all members of the Department of Geography and Urban Sustainability at the United Arab Emirates University for assisting me all over my studies and research.

Special thanks go to my famity and friends who supported me endlessly along the way.

Dedication

To my beloved family and friends…

Table of Contents

List of Tables

List of Figures

List of Acronyms & Abbreviations

1D	One-dimensional
2D	Two-dimensional
3D	Three-dimensional
a.s.l	Above Sea Level
AGDC	Australian Geoscience Data Cube
ALOS	Advanced Land Observing Satellite
ARD	Analysis Ready Data
CNN	Convolutional Neural Network
COSMO-SkyMed	COnstellation of small Satellites for the Mediterranean basin Observation
CSDC	Common Sensing Data Cube
CSI	Coherent Scatterer InSAR
DEM	Digital Elevation Model
DIAS	Data and Information Services
DInSAR	Differential Interferometric Synthetic Aperture Radar
DS	Distributed Scatterers
DTAR	Distributed Targets Ambiguity Ratio
EAD	Environment Agency of Abu Dhabi
EAWS	Earth on Amazon Web Services
ENVISAT	Environmental Satellite
EODC	EO Data Cube
ERS	European Remote Sensing Satellite
ESA	European Space Agency
ESD	Enhanced Spectral Diversity
ESDC	Earth System Data Cube
GB	Gigabyte
GBSAR	Ground-Based Synthetic Aperture RADAR
GEE	Google Earth Engine
GNSS	Global Navigation Satellite System
G-POD	Grid Processing on Demand
GPS	Global Positioning System

GPU	Graphic Processing Unit
GRACE	Gravity Recovery And Climate Experiment
InSAR	Interferometric Synthetic Aperture Radar
IW	Interferometric Wide Swath
LOS	Line-of-Sight
MODIS	Moderate Resolution Imaging Spectrometer
NASA	National Aeronautics and Space Administration
NDVI	Normalized Difference Vegetation Index
ODC	Open Data Cube
PPP	Public-Private-Partnership
PS	Persistent Scatterer
P-SBAS	Parallel Small Baseline Subset
PSI	Persistent Scatterer Interferometry
PTA	Phase Triangulation Algorithm
QCT	Quasi-Coherent Target
Radarsat	Radar Satellite
SAR	Synthetic Aperture Radar
SBAS	Small BAseline Subset
SDFP	Slowly Decorrelated Filtered Phase
SHP	Statistically Homogenous Pixels
SNAP	SeNtinel Application Platform
SNAPHU	Statistical Cost Network-Flow Algorithm for Phase Unwrapping
SNR	Signal-to-Noise Ratio
SRTM	Shuttle Radar Topography Mission
SSEP	Super Sites Exploitation Platform
StaMPS	Stanford Method for Persistent Scatterer
SVD	Singular Value Decomposition
TB	Terabyte
TCP	Temporarily Coherent Point
TEP	Thematic Exploitation Platform
TLMG	Time-Lapse Microgravity
TOPS	Terrain Observation with Progressive Scans
TRAIN	Toolbox for Reducing Atmospheric InSAR Noise

List of Symbols

A	Amplitude
μ_A	Amplitude Mean
B	Baseline
$B_\perp$	Perpendicular Baseline
D_A	Amplitude Dispersion
e	Radar Image
g_0	Gravity Field at the Equator
g_ϕ	Theoretical Gravity at ϕ Latitude
H	Satellite altitude
H	Ground Elevation
P	Radar Reflectivity
R	Range Distance
T	Acquisition Time
γ	Coherence
γ_{geom}	Coherence due to geometric decorrelation
γ_{noise}	Coherence due to system noise
γ_{temp}	Coherence due to temporal decorrelation
Δg	Measured corrected gravity
ΔG_B	Bouguer correction
ΔG_E	Elevation correction
ΔG_F	Free-air correction
Δr	Topographic change in Slant Range
$\Delta\phi$	Interferometric Phase Angle
$\Delta\phi_{atm}$	Atmospheric Phase
$\Delta\phi_{disp}$	Surface Displacement Phase
$\Delta\phi_{err}$	Uncertainty Phase
$\Delta\phi_{noise}$	Noise Phase
$\Delta\phi_{topo}$	Topography Phase
θ	Incidence Angle
λ	Wavelength
ρ	Rock density

σ_A	Amplitude Standard Deviation
ϕ	Phase Angle Difference

Chapter 1: Introduction

1.1 Overview

Land surface monitoring plays a crucial role in understanding the environment and changes that happened on the Earth such as global warming, ice melting, sea level rising, forest fires, and climate changes. Observing land surface changes over a very wide area can be difficult and confusing especially using a traditional field survey. Remote sensing satellites provide very wide coverage with consistent temporal acquisitions which ease the land surface monitoring. In recent years, scientists all around the world used satellite imageries for land surface monitoring such as land use and landcover changes (El Jazouli et al., 2019; MohanRajan, Loganathan, and Manoharan, 2020; Olorunfemi et al., 2020), vegetation health (Fang et al., 2019; Kureel et al., 2021; Petersen, 2018), geological exploration (Bikeeva et al., 2021; Frutuoso, Lima, and Teodoro, 2021; Rajan Girija et al., 2019; Svigkas et al., 2017), land surface deformations (Imamoglu et al., 2019; Pawluszek-Filipiak and Borkowski, 2020; Peng et al., 2019), and ice sheet studies (Baumhoer et al., 2018; Liang, Li, and Zheng, 2019; Sasgen et al., 2019).

Land surface deformations phenomena can be categorized as catastrophic events that can result in the loss of lives and infrastructures. Land surface deformations can occur from either natural causes, e.g. earthquake and volcanic activities, or anthropogenic activities, e.g. underground mining, extraction of underground resources (pumping groundwater, oil, gas, etc.), and underground constructions (He et al., 2020; Kim et al., 2007). The land surface subsidence refers to the moving of the Earth's surface downward relevant to a reference location (Holzer et al., 2005).

The rapid population growth in the world changed natural land covers to urban areas and depleted the natural resources due to overconsumption. The United Arab Emirates (UAE) is one of the fastest developing countries in the world during the last two decades. The population of the UAE has increased gradually from 3 million in 2000 to 10 million in 2020. This growth urged the demand to increase urban areas, farming activities, and water supply. These anthropogenic activities can impact the land surface negatively with overloading the soil, dumping the garbage, and extracting the underground resources.

Radar remote sensing techniques have been developed in the last decades to detect and monitor land surface deformations by the interferometry technique. This technique, also known as Synthetic Aperture Radar Interferometry (InSAR), relies mainly on measuring the distance difference between the radar sensor in the space and ground targets from two different locations. This technique allowed the detection of the first land surface deformations from an earthquake over Landers, California (Massonnet et al., 1993). The development of the InSAR techniques through time has been utilized to study land surface deformations due to landslides (Dong et al., 2019; Tong and Schmidt, 2016), volcanic activities (Papoutsis et al., 2013 ; Pepe et al., 2019), extraction of underground resources (Chen et al., 2020; Fokker et al., 2016; Staniewicz et al., 2020), and urbanization (Dong et al., 2014; Papoutsis, Kontoes, and Paradissis, 2017).

1.2 Research Objectives

The main objective of this research is to study land surface fluctuations, moving up or down, in regional and local scales over the dry semi-arid climate of the UAE using the Synthetic Aperture Radar Interferometry technique. The land surface

of the UAE can be considered stable tectonically and there are no active faults have been found; therefore, any land surface deformations detected could be caused by anthropogenic activities. Except for the northern emirates can be affected by tectonic events in neighboring countries.

The specific research objectives are:

1) To detect and monitor land surface subsidence and uplift over the whole territory of the UAE using Radar Interferometry techniques.
2) To investigate which landcover types are affected and define the driving mechanisms for the land surface movement.
3) To investigate the subsurface mechanism and its relation to the surface movement detected from space.

1.3 Dissertation Organization

This dissertation is composed of six chapters and is organized based on the outcomes of the three papers listed below. Chapter one introduces the research problem with a clear definition for the research objectives alongside how the dissertation is organized. Chapter two presents a concise review of radar remote sensing techniques for monitoring land surface studies with an outlook for big radar imageries data processing. Chapter three presents the methods and techniques that were applied and developed along with the outcomes of the observed land surface deformations over the whole territory of the UAE. Chapter four presents a case study of monitoring land surface subsidence using radar remote sensing and ground truth data over agricultural areas. Chapter five presents an integration of radar remote sensing with geophysical methods with a case study over the Al Ain city. Chapter six presents a summary and conclusion with an outlook for future research.

1. El Kamali, M., Papoutsis, I., Loupasakis, C., Abuelgasim, A., Omari, K., and Kontoes, C., 2021. Monitoring of land surface subsidence using persistent scatterer interferometry techniques and ground truth data in arid and semi-arid regions, the case of Remah, UAE. Science of The Total Environment. 776, 145946.

2. El Kamali, M., Abuelgasim, A., Papoutsis, I., Loupasakis, C., and Kontoes, C., 2020. A reasoned bibliography on SAR interferometry applications and outlook on big interferometric data processing. Remote Sensing Applications: Society and Environment. 19, 100358.

3. El Kamli, M., Saibi, H., and Abuelgasim, A. Groundwater and Land Surface Deformations Monitoring in Al-Ain Arid Region (UAE) using Microgravity and SAR Interferometry Surveys. Environmental Research. Under review.

Chapter 2: Satellite Radar Interferometry

2.1 Synthetic Aperture Radar Interferometry

In recent years the advantages of radar remote sensing systems over optical systems have been clearer and more noticeable. One of these advantages is the ability to measure the phase along with the amplitude of the backscattered signal from the Earth's surface. Signal amplitude is the scattering characteristic of the targeted pixels which is controlled by the scattering mechanisms. While the phase of a signal is related to the distance between the radar satellite and the target where the signal has been scattered back to the satellite. Thus, in radar remote sensing to discriminate between pixels, data of amplitude and phase were sampled for each pixel. Mathematically, the signal is expressed by complex numbers due to the necessity of measuring and processing two linked variables; amplitude and phase. Then the reflectivity of a pixel in a radar satellite image can be expressed by

$$p = |A^2|e^{j\emptyset} \tag{2.1}$$

where A is the amplitude recorded for that pixel and $\emptyset$ is the phase difference between transmitted and backscattered signals from the pixel. Accordingly, separated targets will be discriminated clearly in the radar image if there is a difference in their phase difference angles. If the distance between the radar sensor and ground target can be expressed by R, also known as slant range distance, then the signal traveled a distance of 2R when transmitted from the sensor to when recorded at the radar sensor, and it can be expressed by

$$\emptyset = \frac{4\pi}{\lambda} R \tag{2.2}$$

where λ is the wavelength. Phase measurements are the basis of radar interferometry.

Imaging the same Earth's surface location with two radar sensors, or apertures, with the same characteristics but from different locations in space rise the opportunity to image the same target with different angles. Thus, the same target on the Earth's surface will have two phase difference angles due to the different range distances. From Figure 2.1 we can assume that we have ϕ_1 and ϕ_2 as the phase difference angles, R_1 and R_2 as the range distances, for acquisition 1 and acquisition 2, and θ is the incidence angle, then we can express the difference between the two phase angles as

$$\Delta\emptyset = \emptyset_1 - \emptyset_2 = \frac{4\pi}{\lambda}(R_1 - R_2) = \frac{4\pi}{\lambda}\Delta R \qquad 2.3$$

this measurement is known as Interferometric Phase Angle.

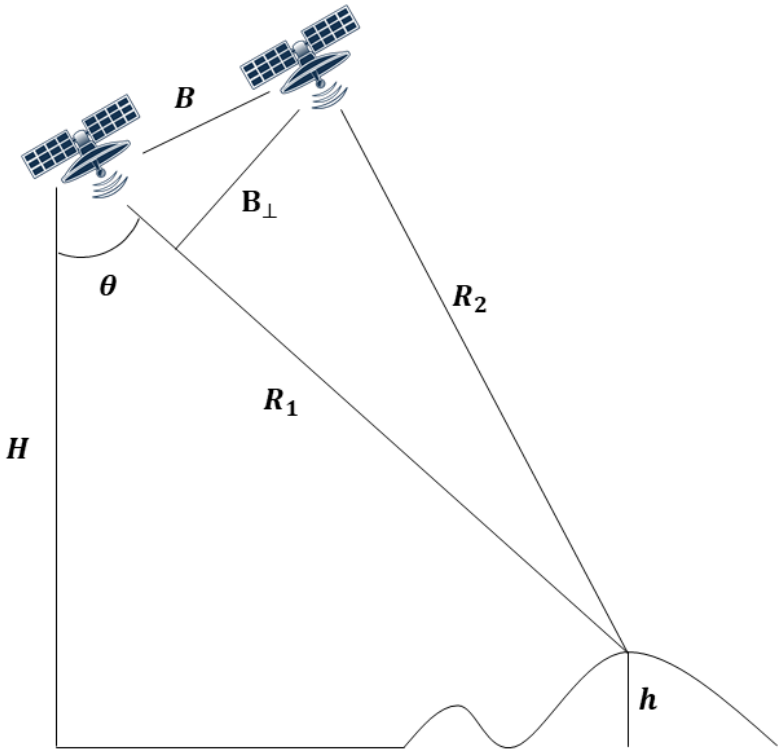

Figure 2.1: InSAR viewing geometry.

For more practical uses the interferometric phase angle is expressed in system parameters instead of the range distant. The separation between the two radar sensors is known as a baseline (B) and the normal between the two range distances is known as a perpendicular baseline ($B_{\perp}$) (Figure 2.1). Thus, Equation 2.3 can be written as

$$\Delta\emptyset = \frac{4\pi B \sin\theta}{\lambda} \qquad 2.4$$

Interferometry techniques were applied from the product of one image by the complex conjugate of the second image pixel by pixel. The complex conjugate of a complex number is the complex number with the negative sign to the Imaginary part of that complex number. So, the formed image from this product is a complex number where it is Real part is the product of the two images intensity while it is Imaginary part is the phase difference between the two images, the interferometric phase angle. This product is called Interferogram and can be expressed mathematically by

$$i(x,y) = \rho_1\rho_2 e^{j\Delta\phi} \qquad 2.5$$

Since the interferometric phase angle is incidence angle dependent, then the interferogram will vary across swath in the range direction without any variation in elevation. This is known as the Flat Earth Phase component.

From the baseline point of view, radar interferometry can be achieved by separating antennas in either the cross-track direction or the along-track direction, and so-called Cross-Track Interferometry or Along-Track Interferometry. Also, interferometry can be achieved either in a single-pass where the platform carries two separated antennas or repeat-pass where the platform collected radar images in two separate passes at different times. Both Cross-Track and Along-Track Interferometry can operate in single-pass and repeat-pass, while Cross-Track Interferometry single-

pass is sensitive to height variations, Along-Track Interferometry repeat-pass is very sensitive to elevation changes between passes.

Coherence is an important statistical measure for the interferogram to be considered significant. It is the degree of correlation between the two images that formed the interferogram. Assuming that the interferogram was formed from two images e_1 and e_2, then the coherence (γ) is the complex cross-correlation between the two images and can be expressed by

$$\gamma = \frac{|e_1 e_2^*|}{\sqrt{|e_1|^2 |e_2^*|^2}} \qquad 2.6$$

Coherence ranges from 0 to 1, where 0 indicates no statistical correlation between the two images and also this case called decorrelated images, while 1 indicates a statistical correlation between the images and known as fully correlated.

Coherence measurement can be decomposed into various components where each component is attributed to a specific decorrelation mechanism. The first component is related to the geometry of the radar interferometry (Figure 2.1), the interferometric phase angle is dependent on the baseline and the incidence angle (Equation 2.4). The incidence angle varies with topography and across the swath (varied from pixel to pixel) but the baseline is a system parameter and can be known for each interferogram generated. A greater baseline will result in a higher interferometric phase angle which means a higher interferometer sensitivity but in order to convert the elevation changes between pixels, the interferometric phase angle changes from pixel to pixel should not exceed 2π. This can be achieved by calculating the baseline from Equation 2.4 when the $\Delta\phi$ is equal to 2π and the other parameters are fixed for any radar system. This measure is known as the Critical Baseline where

beyond this value the inter-pixel phase change cannot be recognized. This component is known as geometry or baseline decorrelation (γ_{geom}).

The second component of coherence is related to the scattering change in the pixel between acquisitions. This change can occur either from changing the looking angle between acquisitions or changes that occurred at the land cover resulting in a different scattering mechanism. Land cover changes are not necessary to change from type to type it can be during the phenological cycle of vegetation, glacier movement, or moisture content changes. This coherence component is called Temporal Decorrelation (γ_{temp}) because these factors are time-dependent and occur between the acquisitions.

The next coherence component is related to the noise in the radar systems that have been used. One way to measure that is by using the Signal-to-Noise ratio (SNR) of the two radar receivers. High SNR indicates less noise which means low decorrelation between images. This component is known as Noise Decorrelation (γ_{noise}). The coherence of an interferogram can be generated by multiplying all decorrelation components

$$\gamma = \gamma_{\mathrm{geom}}\gamma_{\mathrm{temp}}\gamma_{\mathrm{noise}} \tag{2.7}$$

The interferometric phase angle, also known as total interferometric phase difference, is related to the range difference between the two acquisitions as derived in Equation 2.3. In practice, the interferometric phase can be divided into several components where each one contributes to the total interferometric phase difference and they can be expressed by

$$\Delta\phi = \Delta\phi_{topo} + \Delta\phi_{disp} + \Delta\phi_{atm} + \Delta\phi_{noise} + \Delta\phi_{err} \tag{2.8}$$

where $\Delta\phi_{topo}$ is the phase component related to topography, $\Delta\phi_{disp}$ is the phase component related to surface displacement, $\Delta\phi_{atm}$ is the phase component related to the signal delay in the atmosphere, $\Delta\phi_{noise}$ is the phase component related to the noise in the radar systems, and $\Delta\phi_{err}$ is the phase results from uncertainty.

The range difference is the key for topography mapping using radar remote sensing from space. Utilizing the trigonometry with the radar interferometry geometry shown in Figure 2.1 the change in elevation (h) from pixel to pixel can be related to the total interferometric phase difference between pixels as

$$\frac{d(\Delta\phi)}{dh} = \frac{4\pi B_{\perp}\cos\theta}{\lambda H\sin\theta} \Rightarrow \Delta\phi_{topo} = \frac{4\pi B_{\perp}\cos\theta}{\lambda H\sin\theta}\Delta h \qquad 2.9$$

where H is the radar satellite altitude.

If there is a topographic movement between the acquisitions t_1 and t_2 then the total interferometric phase difference will be related to the topography and the topographic movement. These two relations can be expressed by

$$\Delta\phi = \Delta\phi(h, \Delta r) \qquad 2.10$$

where Δr is the topographic change in slant range direction. The first order of the previous can result in

$$\Delta\phi = \frac{4\pi B_{\perp}\cos\theta}{\lambda H\sin\theta}\Delta h + \frac{4\pi}{\lambda}\Delta r \qquad 2.11$$

where the second term is the surface displacement phase component ($\Delta\phi_{disp}$).

In most cases, the radar interferometry is applied to either for mapping topography or detecting surface displacement, the first and second phase components in Equation 2.8. Mapping topography can be achieved by utilizing cross-track interferometry in a single-pass in order to avoid temporal changes on the ground or

elevation such as Shuttle Radar Topography Mission (SRTM) which produces the global Digital Elevation Model (DEM). On the other hand, detecting land surface displacement is achieved better with along-track interferometry and repeat-passes where the phase component related to the topography is minimal. In practice, the radar sensors in repeat-passes interferometry will be separated in both cross-track and along-track. Thus, for detecting land surface displacement removing the phase component related to the topography is required. This is known as Differential Synthetic Aperture Radar Interferometry (DInSAR). The topographic phase can be estimated by two methods; the first is by utilizing three SAR images two images to generate the topography phase component (Equation 2.9), while the second method is by using DEM data to generate the topography phase component, then subtracting it from the total phase interferometric difference. Noteworthy, the total interferometric phase difference contains other phase components than the topography phase as shown in Equation 2.8, so detecting land surface displacement with high precision requires estimating and removing each of these phase components. Furthermore, a small phase component related to noise can be achieved by performing the DInSAR process on pixels that exhibit small phase noise.

The remaining phase after removing all phase components and leaving only the phase component related to the land surface displacement ranges from 0 to 2π due to the sinusoidal function of the radar wave. This type of phase is called the wrapped phase where this signal records the same interferometric phase difference for each difference equal to the wavelength of the signal (Figure 2.2). The wrapped phase appears in the image as repeated cycles of, or discontinuities in, the phase angle wherever its value exceeds 2π. This leads to an ambiguity in number cycles that the

signal traveled between the radar sensor and the target and it is affecting the precision of detecting land surface displacement and mapping topography.

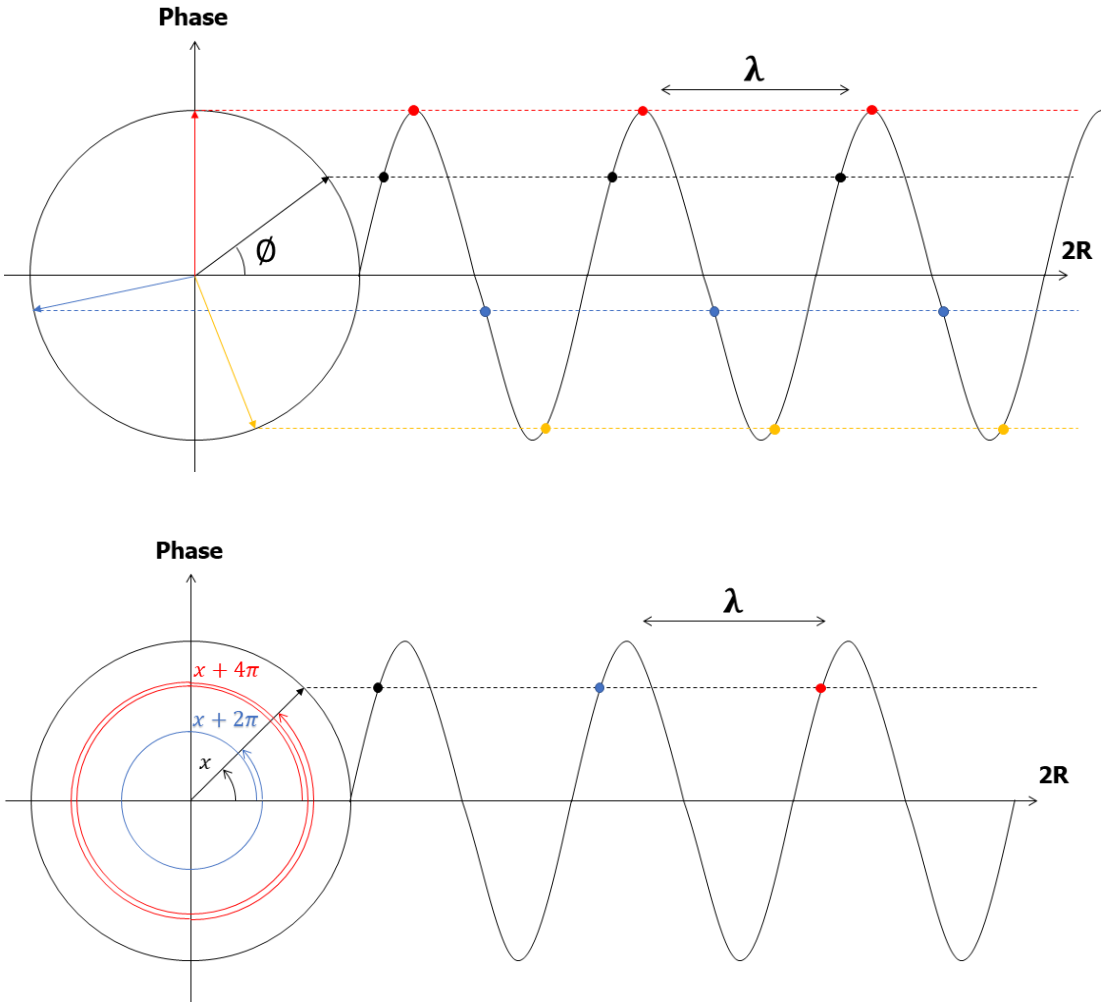

Figure 2.2: Wrapped phase of the radar wave.

Discontinuities in the interferometric phase can be converted to a continuous phase to resolve the ambiguity in the wrapped phase, this process is called the phase unwrapping. It is considered to be the most challenging step in the radar interferometry techniques because in most cases there is a change between pixels exceeding 2π which makes it difficult to generate a continuous surface. For simple cases the phase jumps

can be determined between each cycle, then 2π can be added or subtracted based on the gradient of the phase along each transect.

2.2 InSAR Time-Series Techniques

As above mentioned, processing pixels or targets with small phases will result in smaller phase components related to noise then more reliable surface displacement measurement. Selecting those pixels was a challenge in the development of radar interferometry processing techniques in the late 1990s and the beginning of the 2000s. Research studies showed two approaches to select pixels where their phase noise at minima, the first is determining a strong target scatterer in the pixel where its response remains constant for a long period of time and this is called the Persistent or Permanent Scatterer (PS), while the second is determining pixels with a constant response for a period of time from different targets within the pixel and this is called the Distributed Scatterer (DS). The developed DInSAR techniques over the last two decades employed either PSs, DSs, or combined both. Moreover, the DInSAR techniques can be classified based on the deformation model utilized to convert the displacement phase component into surface deformation time-series. Most of the techniques performed linear deformation model to the sake of it is simple assumption while other techniques performed a non-linear deformation model by applying spatial smoothness or deploying different deformation models.

The first approach to select PSs, which paved the road for the advanced approaches, was proposed by (Ferretti, Prati, and Rocca, 2001) by testing the time-series of the amplitude values for pixels rather than spatial averaging over many pixels. They proposed computing the Amplitude Dispersion (D_A) for each target, or pixel, in all available SAR images as follow

$$D_A = {}^{\sigma_A}/_{\mu_A} \qquad 2.12$$

where σ_A and μ_A represent the standard deviation and mean of the pixel amplitude values. The main two advantages of this approach are being fast processing since the equation is quite simple and there is no resolution loss as in spatial averaging. This technique is called the Persistent Scatterer Interferometry (PSI) technique. This technique requires large temporal (five to six years) and geometrical baselines (near the critical baseline) with SAR images of more than 30 in order to be able to reduce the phase component related to the atmospheric contribution and detect land displacement at a millimetric level. The accurate estimation of the atmospheric phase contribution depends on the number of available images and PSs density. Interferograms were generated between the available images and one selected reference image known as a master image. Moreover, this technique assumes that the land displacement is constant over time, as many geophysical modeling and uses linear deformation model in time.

The disadvantages of the PSI technique were the low PSs density in non-urban or vegetated areas and the continuous SAR images are not available everywhere, in some cases, there are some gaps in SAR acquisitions which is degrading the displacement measurement accuracy. The second approach proposed by (Berardino et al., 2002) to solve the gaps in SAR acquisitions by dividing the available SAR images into small subsets to generate higher number of interferograms, then link all small subsets to fill the gaps between the subsets, this technique is called Small Baseline Subset (SBAS). The pixel selection process in this technique is achieved by selecting the pixels with coherence higher than a specified threshold. The interferograms generated by this technique are much higher than those generated by the PSI technique

which means a larger number of unknowns and infinite numbers of solutions to estimate the land displacement. For this purpose, the Singular Value Decomposition (SVD) was suggested to solve the problem and convert the phase into land displacement with the assumption of spatial smoothness deformation. This technique provided a solution for non-urban and vegetated areas where they appear highly decorrelated in the previous technique, but this technique lacks the sensitivity to detect local deformation because it is performed on multi-looked data which results in resolution loss.

The solution for this limitation has been provided by Lanari et al. (2004) by dividing the SBAS processing single-look and multi-look interferograms into low-pass and high-pass components. This approach showed a successful solution for the local deformation detection problem which suggested on the first hand generating low-pass components with the same procedures proposed by (Berardino et al., 2002) using multi-look interferograms which include large-scale deformations, low-pass topographic errors, and atmospheric phase components. On the other hand, high-pass components were generated by subtracting multi-look interferograms from single-look interferograms, thus processing high-pass components to estimate high-pass topographic signal, deformation velocity, and non-linear deformation velocity where the latter was achieved by implementing the SVD technique.

An extension to the PSI technique has been developed by (Hooper et al., 2004) by enhancing the PS selection step in order to increase the PS density in natural and non-urban areas. Hooper et al. (2004) proposed selecting PS candidates based on their phase characteristics and not only based on the amplitude dispersion where it works with the pixels characterized by high SNR. They proposed forming the differential

interferograms first, then subtracting the phase of each pixel from the averaging phase of neighbor pixels over a specified distance and measuring the temporal coherence for that pixel as a phase stability indicator. Moreover, they suggested the 3D phase unwrapping (2D in space as conventional InSAR and 1D in time) by calculating the phase differences for each PS in time, then unwrapping from a reference PS in space, finally integrating in time to generate unwrapped phase time-series. Furthermore, unlike the assumption of the linear deformation model proposed by (Ferretti et al., 2001), this approach requires no assumption about the temporal deformation and models the deformation by its naturally spatial correlation. This technique has been enhanced in many steps to achieve more reliable displacement measurements, this enhancement results in one of the most using InSAR software packages the Stanford Method for Persistent Scatterer (StaMPS) (Hooper, Segall, and Zebker, 2007).

The co-registration step has been enhanced by estimated mapping functions by using an amplitude-based algorithm to estimate the offset between each slave image and the master image. Furthermore, the phase stability estimation has been improved by developing band-pass filtering that depends on the phase gradient rather than averaging over specified distance as in (Hooper et al., 2004). Then, subtracting the modeled phase correlated in space, estimated from the previous filtering, leave the phase uncorrelated in space which includes the look angle error and the noise phases. The former was estimated using least-squares inversion then subtracted from the remaining phase, the variation of this residual phase was considered as a measure of coherence in time. Finally, PS pixels have been selected based on the coherence and amplitude dispersion probability of each pixel to be PS pixel. This technique suggested that the phase unwrapping step is better to be applied via one of the unwrapping algorithms proposed in (Hooper and Zebker, 2007).

An approach that combined PS and DS scatterers has been proposed by (Hooper, 2008) to increase the processed pixels which increased the reliability of the detected displacement. Hooper (2008) suggested that to select pixels from each technique separately then combining all candidates before the phase unwrapping process. For the PS technique, PS candidates were the same as in (Hooper et al., 2007), while for the SBAS technique a new method was proposed to select pixels, called Slowly Decorrelated Filtered Phase (SDFP) pixels. SBAS interferograms were generated to minimize perpendicular, temporal, and doppler baselines, then a filter in azimuth direction was applied followed by a filter in range direction. Finally, SDFP pixels were selected with the same approach as PS pixels in (Hooper et al., 2007) but from different data sets.

Another approach that combines PS and DS scatterers has been developed by (Ferretti et al., 2011) and the technique was called SqeeSAR. In this technique, the DS scatterers have been selected by an algorithm called DespecKS developed to identify the Statistically Homogenous Pixels (SHP) groups around each pixel. DS scatterers have been defined by SHP pixels over a specified threshold. Then, all selected DSs were linked by a Phase Triangulation Algorithm (PTA) and refined the DS selection by a coherence threshold. Finally, process the selected PSs and DSs with the conventional PSI processing chains (Ferretti et al., 2001).

2.3 InSAR Applications over Different Landcover Types

InSAR techniques have been performed to detect and monitor land surface deformations in so many cases; land subsidence, uplift, volcanic activities, landslides, earthquakes, and material abstraction from undergrounds such as oil, gas, and groundwater. Moreover, these techniques have been applied to different deformation

scales such as over wide area on small scale like surface deformations from earthquakes (Massonnet et al., 1993) and a small area on large scale like displacement in an individual infrastructure (Yang et al., 2016). InSAR time-series techniques rely mainly on identifying a high density of scatterers, PSs or DSs, in order to achieve reliable surface displacement measurements. The density of PSs and/or DSs depends, of course, on the method of scatterers identification as explained in the previous section, but choosing which method to use depends on the ground target of the area under investigation, i.e., landcover types. In the following sections, a bibliography on InSAR applications over different landcover types is provided.

2.3.1 Desert

Desert areas are characterized by similar targets which have less decorrelation to shorter radar wavelengths. In the case of the desert with dominant rocks, performing PSI on X-band or C-band to observe ground displacement over desert areas is very efficient because there is a great possibility to obtain high PS density. In the case of the desert with dominant sand, especially sand dunes, the StaMPS technique can achieve higher PS density because it analyzes the phase history. Gonnuru and Kumar (2018) and Chang, Ku, and Hanssen (2018) studied surface deformations over an oil field in desert areas using X-band SAR data obtained from TerraSAR-X. The former study investigated the land surface subsidence in the Burgan oil field, Kuwait in the period between 2008 and 2011 using the PSI technique and concluded that there is a subsidence rate of 7.2 – 10 mm/year during the mentioned period. The latter study aimed to detect and monitor land surface deformations due to hydrocarbon activities by generating a spatiotemporal variogram model for the InSAR measurements. The time-series results showed that the spatial pattern was smoothly subsiding during oil

extraction and then it had sudden upward movement after the injection activities and finally went down when the mine closed. The study on a hydrocarbon extraction area demonstrated that this method can better model the InSAR deformation time series, and identify sudden uplift or subsidence, at most about 4 cm, due to hydrocarbon production activities.

Another study over desert landcover was performed by Amighpey and Arabi (2016) in Yazd-Ardakan desert, central Iran by utilizing the SBAS technique with ENVISAT C-band SAR data between 2003 and 2006. This study concluded a positive correlation between the rate of water level reduction and the land surface subsidence attributed to aquifer-system compaction.

2.3.2 Glaciers

Glacier surfaces are considered moving fast relative to other landscapes, so selecting which radar frequencies to detect and monitor glacier motion is less significant. Glacier surface motion over Viedma icefield, Argentina has been estimated by utilizing SBAS technique with COSMO-SkyMed X-band SAR data between April 2012 to January 2013 by Euillades et al. (2016). This study concluded that the technique's capability to obtain a high ice displacement rate with a mean surface velocity of 800 mm/year with a high spatial correlation between the topographic slope and displacement mean velocity. Short et al. (2014) aimed to quantify the seasonal ground deformation over permafrost terrain using DInSAR measurements at Iqaluit airport in Nunavut region, Canada using Radarsat-2 C-band SAR data. This study revealed land subsidence up to 12.5 cm with a strong correlation with the surface geology and field electrical conductivity measurements.

Unlike the previous study, Strozzi, Antonova, Günther et al. (2018) utilized Sentinel-1 C-band SAR data to investigate ground deformations over permafrost landscapes. This investigation concluded that near-surface soil properties control seasonal subsidence and there is a relationship between ground thermal and subsidence measurements. Singhroy et al. (2014) and Singhroy and Li (2015) studied the surface deformations from steam injected to the subsurface in the process of oil sands over Athabasca and Alberta respectively, Northern Canada. Both studies used RADARSAT-2 and COSMO-SkyMed with SBAS algorithm, leveling, gravimeters, tiltmeters, inclinometers, and GPS. Both studies showed a strong correlation between the uplift rates over the horizontal injector wells and the rate of steam injection. Moreover, the reservoir thickness and surface deformations are not correlated.

2.3.3 Mountains

Mountainous areas have a high probability to identify high PS density from various radar frequencies and InSAR techniques due to the high coherence and phase stability of their rocky surface. In the case of vegetation cover, lower frequency, higher wavelength, is preferable due to its ability to penetrate through leaves. Also, larger frequencies, like X-band, have a higher atmospheric contribution due to high terrain and redirecting the radar signal.

Investigations over the Kilauea volcano in Hawaii islands were conducted by Hue et al. (2017) and Jo, Jung, and Won (2017) to detect land displacement from volcanic activities. The former constructed a joint model to measure 3D surface displacement from the traditional InSAR stacking measurements using L-band ALOS SAR data. This study showed higher accuracy than the traditional InSAR technique and succeeded to retrieve a vertical displacement with a maximum of -16 cm and

horizontal displacement toward the caldera by -6 cm. The limitations of this model are that it requires prior knowledge about the study area and the model requires to be reconstructed for each radar frequency. While the latter investigation assessed the surface displacement generated from X-band TerraSAR-X using the traditional InSAR stacking by comparing its surface displacement to GPS measurements. This comparison showed a lower accuracy due to the high atmospheric contribution in X-band measurement over mountainous terrain with RMS for the deformation measurement was 3.26 ±1.32 cm and 2.95 ± 0.77 cm from ascending and descending datasets, respectively.

Other studies retrieved surface deformations successfully from X-band TerraSAR-X. Raucoules, Michele, Malet, and Ulrich (2013) performed the offset tracking technique to detect landslides over La Valette landslide, South French Alps between 2010 and 2011. This study observed maximum horizontal displacement rate maximum vertical displacement rates of 14 m/year and 11 m/year, respectively, in agreement with the ground-based observations. Gama et al. (2017) investigated land surfaced deformations over Carajás open-pit iron mine in Brazil using the SBAS technique and the study observed up to 500 mm/year surface deformations and validated with leveling measurements.

Baek, Jung, and Chae (2018) and Kimura (2017) studied land surface deformations due to the Kumamoto earthquake using L-band ALOS-2 SAR data acquired along ascending and descending orbits. The former applied the traditional InSAR stacking technique and retrieved surface deformations of 2 m in vertical and horizontal directions. While the latter study decomposed surface deformations into three components with 70, 50, and 30 cm for eastward, northward, and upward,

respectively. The comparison between InSAR deformations components and GNSS measurements showed strong agreement with eastward and upward components and less agreement with the northward component.

A combination of X-band and C-band SAR data has been applied to detect land surface deformations (Polcari et al., 2017; Sansosti et al., 2014). An investigation of small effects from the central Italy seismic sequence 2016-2017 using X-band COSMO-SkyMed and C-band Sentinel-1 SAR data with traditional InSAR stacking technique (Polcari et al., 2017). The same SAR data combination, but with C-band ERS1/2 and ENVISAT instead of Sentinel-1, has been utilized with SBAS technique to investigate surface displacements over Campi Flegrei and Mountain Etna, also L-band ALOS SAR data added, volcanic areas in Italy (Sansosti et al., 2014). Involving X-band SAR data allowed to unveil the driving process behind the deformation while the SBAS technique retrieved the non-linear deformations.

An integration between InSAR measurements and GRACE (Gravity Recovery And Climate Experiment) has been performed by Zheng et al. (2018) in order to analyze surface deformations over Xuzhou coalfield, China. This study is based on Temporarily Coherent Point (TCP) InSAR which does not require the TCP to be coherent during the entire monitoring period and does not require phase unwrapping. This integration allowed to understand the relationship between groundwater storage change and surface deformation. This study concluded that the main reason for surface subsidence, with a rate of -25.6 mm/year, was underground mining and the main reason for the surface uplift, with a rate of 10.3 mm/year, was groundwater rise after closing the mine.

StaMPS technique has been performed with C-band ENVISAT SAR data by Dwivedi et al. (2017) and Papoutsis et al. (2013). The first one proposed PTA to provide wrapped the interferometric phase before phase unwrapping in StaMPS. This methodology successfully extracted enough measurement pixels in non-urban areas compared to standalone PSI processing with detected surface displacements of -20 to 25 mm/year. The latter one investigated the inflation episode in Santorini Island, Greece by combining both PSI and SBAS on the StaMPS approach. This study retrieved land surfaced displacements ranging from -10 to 150 mm/year in agreement with GPS velocity measurements.

The combination of poly-interferogram rate and time-series estimator algorithm (Π-RATE) were applied on SAR data acquired over Linfen-Yuncheng Basin, China, and allowed to observe the surface displacement of the basin (Zhao et al., 2018). Π-RATE employs a pixel-wise approach to calculate deformations rates at pixels that are coherent in different numbers of interferograms, thus ensuring that useful information about the magnitude and spatial extent of the deformations field can be retrieved.

2.3.4 Rural

Rural areas are characterized by aspects from urban areas such as buildings that produce permanent scatterers for a long time either from building materials or corner reflection mechanisms. Also, rural areas have some aspects from desert areas where distributed scatterers are located. Thus, in order to obtain a significant PS density over rural areas StaMPS approach is effective due to its ability to identify PS scatterers based on amplitude, works well with urban aspects, and based on phase stability, captures good PS density in desert areas.

Raucoules, Cartannaz, Mathieu, and Midot (2013) delineated subsidence over Hilsprich village, north of France, by performing PSI technique with C-band ENVISAT and L-band ALOS-1 SAR data. This study was conducted over a small rural area of 0.3 km^2 and retrieved a subsidence rate of 9 cm/year. Zhang et al. (2014) as well performed the PSI technique but with X-band TerraSAR data over Tianjin city of China and applied the LOS deformations to an integrated model in order to separate it into main and periodic deformations.

Strozzi, Klimeš, Frey et al. (2018) combined C-band SAR data from ENVISAT and Sentinel-1 with L-band ALOS-1 SAR data to observe landslides over Carhuaz, Peru using the PSI technique. This study classified 27% of the study area as landslides with 42 landslides divided into active state motion, continuously active landslides, and episodic active landslides. Demonstration of the potential of the Quasi-Coherent Targets (QCTs) based InSAR analysis using ALOS-1 in the subsidence monitoring of large scale over Tianjin, China (Tao et al., 2012). This study observed a subsidence rate larger than 2 cm/year in agreement with survey and leveling measurements.

Dong et al. (2018) proposed a new approach to investigate landslides by combining persistent scatterer targets with distributed scatterer targets called Coherent Scatterer InSAR (CSI) with C-band ENVISAT and L-band ALOS-1 SAR data. This method was conducted in three steps; first, the persistent scatterer targets and distributed scatterer targets were identified, then their optimal phases were estimated, finally, they were processed to calculate the deformation measurements. This study found that the main factor behind Jiaju landslide instability is the fluvial erosion from the Dajinchaum River. The comparison between CSI and traditional InSAR showed that; CSI five times in time-consuming, CSI four times in storage, CSI density points

are ten times, and CSI with L-band data provided high-quality points over vegetated areas. CSI method is facing the challenge of Sentinel-1 huge collection, this research recommended a massive parallelization of the CSI.

2.3.5 Vegetation

Since InSAR techniques rely mainly on identifying pixels that remain coherent, or slowly decorrelated, for a long period of time, vegetation landcover can be considered more complicated than others for InSAR time-series analysis due to its changing in scattering mechanisms rapidly. Thus, InSAR techniques with DSs are most usable over vegetated landcover, and also due to fast change in vegetation SBAS techniques are appropriate to increase the PSs and DSs density.

Wei and Sandwell (2010) assessed the coherency of C-band ERS and L-band ALOS-1 over vegetated areas in California by quantifying the temporal decorrelation for both satellites. Interferograms generated from both satellites were remained coherent over pixels with NDVI (Normalized Difference Vegetation Index) less than 0.3, NDVI was captured from MODIS (Moderate Resolution Imaging Spectroradiometer) satellite data. The comparison between ALOS and ERS showed that ALOS interferograms showed higher coherence than ERS generally, but it was less over sandy surfaces.

Reeves, Knight, and Zebker (2014) investigated the uncertainty of implementing the SBAS technique to estimate surface deformations over agricultural areas in San Luis Valley (SLV), Colorado. This study relied on calculating the coherence for each interferogram using Gaussian distribution, then using these coherence values to estimate the uncertainty in the interferometric phase. The method

proposed in this study allowed to estimate the uncertainty on a pixel by pixel before performing SBAS analysis. This method showed a significant correlation between mean coherence measured by the Gaussian distribution and the mean standard deviation of the estimated deformation.

Liosis et al. (2018) investigated land surface subsidence over an agricultural area south of the Al Ain region, Abu Dhabi, UAE, by utilizing the SBAS technique with C-band ENVISAT and L-band ALOS-1 SAR data. This investigation observed a subsidence rate of -18 cm/year between 2003 and 2010 with a cumulative displacement of more than -1 m in the same period. It suggested future work to include accurate field measurements using GNSS to validate the SAR time-series deformation. Land surface deformations over the Gippsland Basin, Australia, have been studied by (Ng, Ge, and Li, 2015) using the SqueeSAR technique with L-band ALOS-1 SAR data in the period between 2007 and 2011. This research concluded that the basin is relatively stable with displacement rates between -10 mm/year to 10 mm/year at 98% of the measured points. This study represented the capability of the InSAR techniques for large-scale land surface deformations monitoring.

2.3.6 Urban Areas

Applications of InSAR techniques over urban areas are massive due to the severe anthropological effects on urban environments and studying their consequences is inevitable. Another reason for these massive applications can be the coherent aspect of the urban environment that presents a high PS density over most radar frequencies and InSAR techniques.

Normand and Heggy (2015) studied the ground deformation over Montreal city in the period between 2008 and 2010 using the SBAS technique with C-band RADARSAT-2. The observed displacement measurements were ranged from -2 to 1 mm/year and were attributed to the change in the hydraulic conductivity. Pepe et al. (2016) investigated land displacement over Hawaii Island using the SBAS technique with C-band ENVISAT SAR data during the time span between 2003 and 2009. This study decomposed the LOS deformation into up-down, east-west, and north-south components with an accuracy of 8 mm, 9 mm, and 2 cm, respectively. Horst et al. (2018) delineated the subsidence zone in Yangon, Myanmar, using PSI technique with C-band Sentinel-1 SAR data and retrieved a subsidence rate of 120 mm/year.

Scifoni et al. (2016) investigated ground deformations over Rome city using C-band from ERS-1/-2 and ENVISAT with the SBAS technique in the period between 1992 and 2012. This investigation concluded displacements on buildings of recent construction with about 1 cm/year and displacements on historic buildings in central Rome up to a few millimeters per year. Calò et al. (2015) and Aslan et al. (2018) inspected land surface deformations over the city of Istanbul, Turkey, where the former utilized SBAS technique with X-band TerraSAR-X SAR data, while the latter applied PSI technique with C-band from ERS-1/-2, ENVISAT, and Sentinel-1 SAR data. The latter study observed a subsidence rate ranging 5 – 15 mm/year while the former study concluded total subsidence of 3 cm.

X-band TerraSAR-X SAR data have been utilized by Bai et al. (2016) with the StaMPS technique to monitor land surface deformations over Wuhan city, China. This study obtained a deformation rate between -67 to 17 mm/year. Chaussard et al. (2014) and Castellazzi et al. (2018) inspected land surface deformations over the city of

Mexico using L-band ALOS SAR data. The former study implemented the SB technique and retrieved land subsidence with a maximum of 30 cm, whereas the latter study integrated InSAR deformations measurements with GRACE data and observed maximum subsidence of 20 cm. Tong and Schmidt (2016) analyzed L-band ALOS SAR data with the SBAS technique in order to correlate its measurement with landslide over the Cascade Landslide Complex in Washington. This study concluded that the landslide is active in winter with a high correlation between observed deformations and precipitation. A comparison between surface deformations observed using C-band and X-band showed that the latter radar frequency can estimate surface deformations with higher accuracy, furthermore, can detect surface deformations over areas that the former radar frequency assumed its stable (Calò et al., 2014; Costantini et al., 2015; Yu et al., 2017).

Qu et al. (2015) inspected land surface deformations around Houston-Galveston, Texas, by combining C-band ERS and ENVISAT with L-band ALOS SAR data and utilizing the StaMPS technique with PSs and DSs. This study observed land subsidence rate up to 53 mm/year and uplift rate up to 20 mm/year between 1993 and 2000, also a subsidence rate up to 11 mm/year was observed between 2004 and 2011. Land surface fluctuations were attributed to groundwater and hydrocarbon dynamics.

Qu et al. (2014) investigated land surface subsidence over Xi'an city, China, by utilizing X-band TerraSAR-X, C-band ENVISAT, and L-band ALOS SAR data with SBAS technique in the period between 2005 and 2012. This study detected land surface subsidence zones within the study area with a maximum subsidence rate of 9 mm/year. The same approach has been implemented by Haghighi and Motagh (2019) to detect land surface deformations over Tehran plain, Iran, where observed three

dominant subsidence zones mainly occurred over agricultural areas with subsidence up to 25 cm attributed to groundwater overexploitation and sediments load.

Chet et al. (2015) presented experimental results of the Ground-Based Synthetic Aperture RADAR (GBSAR) in surface deformations monitoring at Peninsular Malaysia using Ku-band. GBSAR has proved significant in-ground deformations monitoring by the capability of applied over broad areas, avoiding weather conditions, and high change detection capability (sub-millimeter). The experiment showed that the GBSAR is capable of detecting sub-centimeter changes with an error of 5 mm and could attain a significantly high coherence of more than 0.9 between interferometric image pairs.

2.4 Satellite Interferometry and Big Data Processing

This section dives into the emergence of new technologies for finding faster, cost-effective ways to process big Earth Observation data at scale. The focus of this part of the review is on the processing of big interferometric synthetic aperture radar datasets, rather than on generic remote sensing assets. Emerging technologies can be explored under three axes: (i) the availability of cloud infrastructures and high-Performance computing environments that allow efficient multi-temporal PSI processing, even at a national scale, (ii) the organization of interferometric datasets in advanced geospatial databases called Data Cubes, which allow enhanced management of long time-series of interferometric measurements, and (iii) the prospects of using machine/deep learning algorithms powered by advanced cloud computing infrastructure to either generate more robust radar interferometry products or mine new information hidden within InSAR products and associated land-surface deformations, extract new knowledge and develop novel value-adding processing chains.

2.4.1 Interferometric Processing on the Cloud

The new generation of Earth Observation satellites from the Sentinel missions generate vast amounts of data that are not easily integrated into processing chains outside the ground segments of space agencies. Very often, public and private institutions aiming at delivering end-user services based on Earth Observation data do not possess the computing power and storage capacity to profit from these new data flaws.

The Helix Nebula Initiative[1] started as a Public-Private-Partnership (PPP) to evaluate the needs of European compute-intense scientific research organizations and their exploitation of a Cloud Computing Infrastructure. Through the Helix Nebula Science Cloud initiative, a partnership was established between leading IT providers and some of Europe's biggest research centers that deployed and tested the infrastructure. One of the critical Use Cases of the Helix Nebula initiative is the one led by the European Space Agency (ESA), forming the ESA Super Sites Exploitation Platform (SSEP) Flagship.

SSEP developments comprised an instance of an exploitation platform for radar imagery in the context of geo-hazards, for the sharing of SAR data, and the exploitation of interferometry processing on those data focusing on earthquake and volcano research. A large amount of SAR data is accessible to science communities dealing with interferometry, landslide, and change detection. The SSEP project brings together existing software components and EO data in a portal that allows geohazard scientists to apply their algorithms and tools to analyze the data. Instead of

[1] https://www.helix-nebula.eu/

downloading the data and applying their tools, users are presented with a wide selection of tools that they can apply within the portal, using cloud and grid technologies to achieve high performance and efficient use of communications links.

The SSEP flagship use case enabled Helix Nebula to mature its federated Cloud architecture and ultimately allowed ESA to analyze the feasibility and benefits of cloud deployments and paved the way to the development of the Thematic Exploitation Platform (TEP) initiatives. The TEP's canonical scenarios have moved the processing to the data, rather than the data to the users, thereby enabling ultra-fast data access and processing. This idea is an evolution of the Agency's Grid Processing on Demand (G-POD) system, the SSEP, and the integration of scientific applications and services for the FP7 EC projects (e.g. GEOWOW, SenSyF) and the experience gained with integration and deployment APIs leveraged within the Helix Nebula initiative.

Since 2018 and in order to facilitate and standardize access to data, the European Commission has funded the deployment of five cloud-based platforms providing centralized access to Copernicus data and information, as well as to cloud processing tools (open source and/or on a pay-per-use basis). These platforms are known as the DIAS, or Data and Information Access Services (DIAS). DIAS's objective is to become breeding grounds for innovative applications or "algorithm factories" allowing users to discover, manipulate, process and download Copernicus data and information.

Considering the processing of interferometric stacks on the cloud, there have recently been some research activities to automate PSI and/ or SBAS processing chains. De Luca et al. (2015) have developed G-POD, a web tool for the unsupervised retrieval of Earth's surface deformation velocities using an online Parallel Small

Baseline Subset (P-SBAS) approach (Casu et al., 2014) tailored for ERS and Envisat datasets. The ESA funded G-POD is a generic GRID-based operational environment coupled with high-performance and sizeable computing resources managed by GRID technologies. The architecture of the platform includes over 200 Working Nodes and more than 70 TB of EO data online. There are links with data providers and satellite imagery repositories.

The evolution of G-POD, so that it accommodates Sentinel-1A&B datasets, has been recently published by Manunta et al. (2019). The CNR-IREA team has put into place a methodology to automatically process co-registered interferometric vast swath stacks using enhanced spectral diversity (Fattahi, Agram, and Simons, 2017). It makes use of both multicore and multimode programming techniques and consists of an ad hoc designed distributed storage implementation (Manunta et al., 2019), aimed at providing scalable performances for massive amounts of data to be processed (Zinno et al., 2017; Zinno et al., 2015; Zinno et al., 2016). The approach has been tested for the whole Italian territory consisting of 2740 Sentinel-1 slices, while the results have been validated by nearly 500 GPS stations scattered over Italy.

There are a few other research activities to perform national scale mapping using PSI on the cloud, which has not been published yet. These include the InSAR Norway project[2], managed and coordinated by the Geological Survey of Norway. The project has processed Sentinel-1 SAR data from both ascending and descending orbits to generate deformation rate histories for two lines of sight vectors, therefore, unmixing vertical and horizontal displacements. Besides, the National Observatory of Athens developed a similar application that aims at national scale deformation

[2] https://insar.ngu.no/

mapping in Greece. The observatory has developed implementations of the InSAR Scientific Computing Environment (ISCE) and StaMPS software for interferogram formation and PSI analysis respectively, to be executed in distributed cloud environments (Papoutsis et al., 2020).

Finally, there are two similar applications for mapping land motion over the United Kingdom since 2015, TRE ALTAMIRA and Geomatic Ventures Limited (GVL). TRE ALTAMIRA has processed more than 7000 satellite radar images to generate a nationwide database of displacement measurements, while GVL uses its in-house advanced InSAR analysis of over 2000 Sentinel-1 to generate a relative land motion map[3].

2.4.2 Data Cubes for SAR Interferometry Datasets

EO data cube is a relatively new term, which describes the organization (or "cubing") of raster data into a database-like structure that enables the efficient Spatio-temporal querying and processing of satellite images. EO data, having the 5Vs of big data (Velocity, Volume, Value, Variety, and Veracity), have an inherent challenge; how to optimize information extraction from these data cubes? The opportunity that is addressed by the data cube concept is the exploitation of past and daily satellite observations to learn from the past, identify trends hidden in the big EO data, extract new knowledge, and potentially short-term forecast some environmental variables.

Some of the most successful representations of the EO data cube concept implementations are the Australian Geoscience Data Cube (AGDC[4]), (Lewis et al.,

[3] https://www.geomaticventures.com/uk-map.
[4] http://www.datacube.org.au/.

2017), the EO Data Cube (EODC[5]), the Earth System Data Cube (ESDC[6]), the Swiss Data Cube (Giuliani et al., 2017), the Common Sensing Data Cube (CSDC), the Ghana Data Cube (Haarpaintner, Killough, Ofori-Ampofo, and Boamah, 2018), Earth on Amazon Web Services (EAWS[7]), and Google Earth Engine (GEE[8]). In contrast to traditional database structure, which cannot handle, either at all or not in scale, geospatial data, the AGDC, EODC, and ESDC rely on open source geospatial relational databases (e.g. PostgreSQL/PostGIS and Rasdaman, as by (Baumann, Misev, Merticariu, and Huu, 2019) to implement the EO cube concept. Less scalable GEE adopts a different approach to implement the concept and EAWS, which uses proprietary cloud software and infrastructure to process the data in a file system-based concept.

Currently, most known Data Cube implementations rely on optical imagery (Baumann et al., 2018; Dhu et al., 2017), and only a few of them offer access to SAR products. Currently, two Data Cubes implementations focus exclusively on the use of SAR imagery. These are the SAR-Enabled Australian Data Cube (Ticehurst et al., 2019) and the Swiss Data Cube (Truckenbrodt et al., 2019). Both of them rely on the Open Data Cube (ODC[9]) initiative (Killough, 2018), populated with SAR data following the CEOS Analysis Ready Data (ARD) specifications. ODC is an open-source geospatial data management and analysis software project which has at its core a set of Python libraries and PostgreSQL database to allow working with geospatial raster data.

[5] http://eodatacube.eu/.
[6] http://earthsystemdatacube.net/.
[7] https://aws.amazon.com/earth/.
[8] https://earthengine.google.com/.
[9] https://www.opendatacube.org/.

The Swiss Data Cube, in particular, is based on a cloud computing platform hosting 35 years and several TB of radiometrically terrain corrected SAR gamma naught backscatter data over the entire county. The Australian Data Cube, on the other hand, has created a unique dataset based on satellite interferometry by-products. This consists of multi-temporal coherence layers, which can be used for land-cover change (Plank, 2014) and/or vegetation growth (Tamm, Zalite, Voormansik, and Talgre, 2016) studies.

An excellent example, although still at a concept level, for exploiting Data Cubes for deformation monitoring using interferometric techniques is presented by Lazecky et al. (2016). In this approach, a special geo-database is designed to ingest, store and manage co-registered Sentinel-1 bursts directly. Burst stacks are then processed on demand for user-selected areas of interest, using PSI as implemented by StaMPS software. At a post-processing phase, a data mining approach is applied for detecting deformation outlier estimates (Bakon, Oliveira, Perissin, Sousa, and Papco, 2017) and creating a more reliable ground velocity pattern.

2.4.3 Deep/Machine Learning for Satellite Interferometry

While research on artificial intelligence has experienced significant growth over the last decade and data science has nearly become a commodity in various industries, deep learning has been one of the fastest-growing trends in big data analysis and was deemed one of the ten breakthrough technologies of 2013. In-depth learning research has been extensively pushed by Internet companies, such as Google, Baidu, Microsoft, and Facebook, for several image analysis tasks, including image indexing, segmentation, and object detection. However, it is only very recently that deep learning

technologies were introduced to the EO research community (Zhu et al., 2017) for data mining and information extraction from big satellite data.

According to Soenen (2019), the ever-broadening use of deep learning in remote sensing is due to two trends: 1) availability of cloud computing infrastructure and resources, including Graphic Processing Units (GPUs); 2) the development of easy to use machine learning libraries like Google's Tensorflow[10], AWS SageMaker[11], sci-kit learn[12], and other open-source frameworks; and 3) an expanding ecosystem of services for creating labeled training data (Scale[13], Figure Eight[14]) as well as open-labeled datasets tailored for satellite imagery, like SpaceNet on AWS[15].

The use of deep learning on interferometric synthetic aperture radar data is discussed below. This is a new field that has started to gain increased attention in the past two years, and it is expected that the number of research projects will kick off. There are currently two families of research works related to deep learning on InSAR; the first one focuses on the automatic detection of ground deformation for setting-up an alert mechanism. This is accomplished through the recognition of interferometric phase fringes associated with ground deformation and eliminating background noise and fringes. The second family of deep learning processing chains is motivated by the well-formulated, ill-posed problem of phase unwrapping on satellite interferometry and medical imaging.

[10] https://www.tensorflw.org/.
[11] https://aws.amazon.com/sagemaker/.
[12] https://scikit-learn.org/stable/.
[13] https://scale.com/.
[14] https://www.fiure-eight.com/.
[15] https://spacenetchallenge.github.io/datasets/datasetHomePage.html.

2.4.3.1 Volcanic Ground Deformations Detection

Anantrasirichai et al. (2018) were the first ones ever to use deep learning on SAR interferograms to detect deformation. In their pioneer work, they processed more than 30,000 short-term wrapped interferograms to automatically detect volcanic ground deformation at over 900 volcanic areas around the world. They pre-train the network using an older archive of interferograms for ESA's Envisat satellite. Since most of the interferograms do not contain any deformation and in order to balance the training sample classes through data augmentation, the authors increase the number of positive examples (i.e. interferograms containing volcanic deformation) through shifting, flipping, rotating, and distorting the shape of positive examples. They then employ a transfer learning strategy for the AlexNet Pre-trained Convolutional Neural Network (CNN). The model identified 104 positive results contained concentric fringes around the volcano, and for which even experts were unable to determine from a single interferogram whether the fringes were caused by volcanic deformation or atmospheric artifacts. Overall, the Anantrasirichai et al. (2018) proof-of-concept study demonstrated the ability of CNNs to identify rapidly deforming systems that generate multiple fringes in wrapped interferograms, which for a 12-day C-band interferogram, corresponds to a deformation rate of 1.8 m/year.

Valade et al. (2019) build upon the study of Anantrasirichai et al. (2018) and trained a CNN on synthetically generated interferograms. The main progress is that Valade et al. (2019) is better at augmenting the deformation samples to prevent overfitting. They produce synthetic training data, allowing the generation of an unlimited number of interferograms, and avoiding the time-consuming task of labeling interferograms where deformation is identified through photo-interpretation. Besides,

Valade et al. (2019) output clean phase gradients that can be used directly to quantify volcanic deformation, whereas Anantrasirichai et al. (2018) estimate the probability a certain interferogram contains deformation fringes. Lastly, instead of using AlexNet as a pre-trained network, Valade et al. (2019) were designed from scratch and trained on a synthetic dataset, thereby allowing more flexibility.

Anantrasirichai and colleagues, however, in a new study by Anantrasirichai et al. (2019) also used synthetic interferograms to train the CNN model, however, based on analytic models simulating realistic deformation sources in volcanic settings. The synthetic interferograms in (Anantrasirichai et al., 2019) are generated from i) synthetic deformation signals produced using simple elastic sources for earthquakes, dykes, sills, and point pressure changes at magma chambers, ii) stratified atmospheric interferograms obtained from the Generic Atmospheric Correction Online Service (Yu, Li, and Penna, 2018), and iii) turbulent atmospheric interferograms simulated using the statistical characteristics of correlated noise in real interferograms (Biggs et al., 2007). This enhanced approach achieves better performance than Anantrasirichai et al. (2018) that uses real interferograms alone, decreasing the number of false positives by >80%.

The MATTCH project – Machine Learning methods for SAR-derived Time Series Trend Change Detection – has a similar objective to the research works presented above. MATTCH aims to apply Machine Learning techniques to InSAR data, for identifying persistent scatterers exhibiting displacement time series characterized by a change in trend or, more generally, an “anomalous behavior”. To capture the temporal dependencies in the long displacement time series, the leading

Deep Learning architectures proposed by MATTCH for the analysis are Long Short-term Memory (LSTM) and Gate Recurrent Unit (GRU).

2.4.3.2 Phase Unwrapping

Phase unwrapping is a classic signal processing problem that refers to recovering the original phase value (integer ambiguities) from its wrapped, modulo 2π form. Two-dimensional phase unwrapping problem arises in many applications such as optical measurement techniques (e.g., digital holographic interferometry and fringe projection profilometry, InSAR and Magnetic Resonance Imaging (MRI).

Feng et al. (2019) were one of the first works to train deep neural networks to perform fringe analysis, for a fringe projection profilometry use case. Spoorthi, Gorthi, and Gorthi (2018) propose a new framework for unwrapping the interferometric phase, formulating a semantic segmentation problem, and using deep Fully Convolutional Neural Networks (FCN). Their model, termed PhaseN consists of an encoder network, a corresponding decoder network followed by a pixel-wise classification layer. Training is performed using simulated data of wrapped and the corresponding unwrapped interferograms. This model achieves excellent performance under severe noise conditions and is computationally fast. Zhang et al. (2019), also formulate a semantic segmentation and propose a similar deep CNN, named DeepLabV3þ, the problem for phase unwrapping. Zhang et al. (2019) performed benchmarks and showed that their deep learning model outperforms the conventional path-dependent and path-independent algorithms.

Given these latest advancements, there are new research projects that exploit computing depth and surface orientation maps directly from single images to derive

an automated solution to unwrapping. Using deep networks with linked pipelines working at different spatial scales, the output maps are gradually refined, with information passing down from coarser to more beautiful scales. These research works have not yet published any results.

2.4.4 Semantic Data Mining

Sentinel-1 data for interferometric analysis, on the other hand, have two distinct characteristics: 1) they are made available on a free and open basis and 2) they are big data: indicatively the data volume of one month of Sentinel-1A acquisitions accounts for the entire ERS and Envisat archive. Similarly, Copernicus data sources are variable ranging from raw Sentinel data to in-situ information and model outputs (e.g. CAMS) with different quality standards, and in some instances such as the Sentinel-4 mission, data will arrive at high velocity.

Pure availability and accessibility of the plain interferometric data is only a first step. The EO data gains value only once it is s analyzed, correlated, enriched with other data sources, and turned into information and knowledge. The sheer volume of the interferometric data - both per time and aggregated over time poses data management and analysis challenges that exceed the capabilities of current data management and analysis solutions for EO data.

The next logical step is to describe the data, products, and tools tailored for satellite interferometry, to create in other words ontologies that link different types of resources together, for a specific application. Koubarakis et al. (2016), argue on the use of the linked data paradigm for significant data discovery and integration, using optical remote sensing use cases.

Semantic representation of interferometric data could pave the way for the use of other technologies, such as data mining and semantic querying. These technologies enable semantic-based data mining. Indicatively, using these technologies one could ask the virtual database and retrieve suitable satellite imagery to conduct time-series interferometry, in previously high earthquake hazard areas in Chile, which contain or are close to cities with more than 50,000 inhabitants. Semantics-based data mining can lead the way for employing analytics applications and discovering patterns in the available interferometric data.

Chapter 3: Land Surface Deformations over the United Arab Emirates

3.1 Introduction

This chapter presents the implementation of the InSAR technique over the UAE using the Sentinel-1 SAR dataset to detect the deformed zones. A detailed discussion of implementing the PSI technique over a national scale is also provided within this chapter. There are several studies aimed to implement the InSAR over a national scale; such as mapping surface deformations over the whole Italian territory using ERS, ENVISAT, and COSMO-SkyMed SAR datasets (Costantini et al., 2017), monitoring and mapping surface deformations over Norway (Dehls et al., 2019), mapping ground deformation over Germany (Haghshenas Haghighi and Motagh, 2017), and ground motion using Sentinel-1 data over Greece (Papoutsis et al., 2020).

3.2 The Landscape of the UAE

UAE is located within the Asia continent in the eastern part of the Arabian Peninsula at the edge of the Rub' Al Khali desert with an international border with Saudi Arabia (457 km) in the south and west and Sultanate of Oman (609 km) in the east (Figure 3.1). UAE is bounded from the north by the Arabian Gulf and the northeast by the Oman Sea. Also, it occupies an area of 83,600 km^2 and is characterized by an arid climate with precipitation less than 100 mm per year and average annual evapotranspiration of 2-3 m (Mohamed, 2014).

The terrain of the UAE is varied from the flat barren coastal plain in the west along the coastline to sand dunes in the middle and south of the country while mountains occupy the eastern part. Most cities of the UAE are located at the flat coastal plain area such as Abu Dhabi (The Capital), Dubai, Sharjah, Ajman, Umm Al Quwain,

Ras Al Khaimah, and others. The first three cities represent about 85% of the UAE population. Sand dunes cover the south part of the country and most of the middle part with more than 75% of the total area of the UAE.

Mountains in the UAE are located in the east, specifically in the Al Ain and Fujairah, and northeast, in Ras Al Khaimah. The most known mountain is Jebel Hafit southeast of the Al Ain city with an elevation of 1,250 m and it is shared with Sultanate Oman. This mountain is characterized by a wide cave system. The highest mountain in the UAE is Jebel Yibir, also known as Jebel Al Mebrah, with an elevation of 1,727 m southeast of Ras Al Khaimah. Another known mountain in the Ras Al Khaimah is Jebel Jais which is famous for touristic activities. In addition, other landforms campaign with mountains is hot springs which are located in close distances to the mountains. Two hot springs, Mubazzarah and Al Ain Al Fayda, are located near Jebel Hafit, while Ain Khatt hot spring is located near Jebel Yibir.

Generally, these are the landscapes of the UAE in addition to some islands, natural and artificial, such as Sir Abu Nu'Ayr, Sir Baniyas, and Abu Al Abyad islands. Also, there are oases such as Al Ain and Liwa in Abu Dhabi emirate in addition to wetlands such as Ras Al Khor in Dubai.

There are several agricultural activities distributed around the country where most of these activities are concentrated in the Abu Dhabi Emirate specifically in the Al Ain region, represented by Al Khazna, Remah, Al Araad, and Al Wagan, and in the Al Dhafra region represented by Liwa.

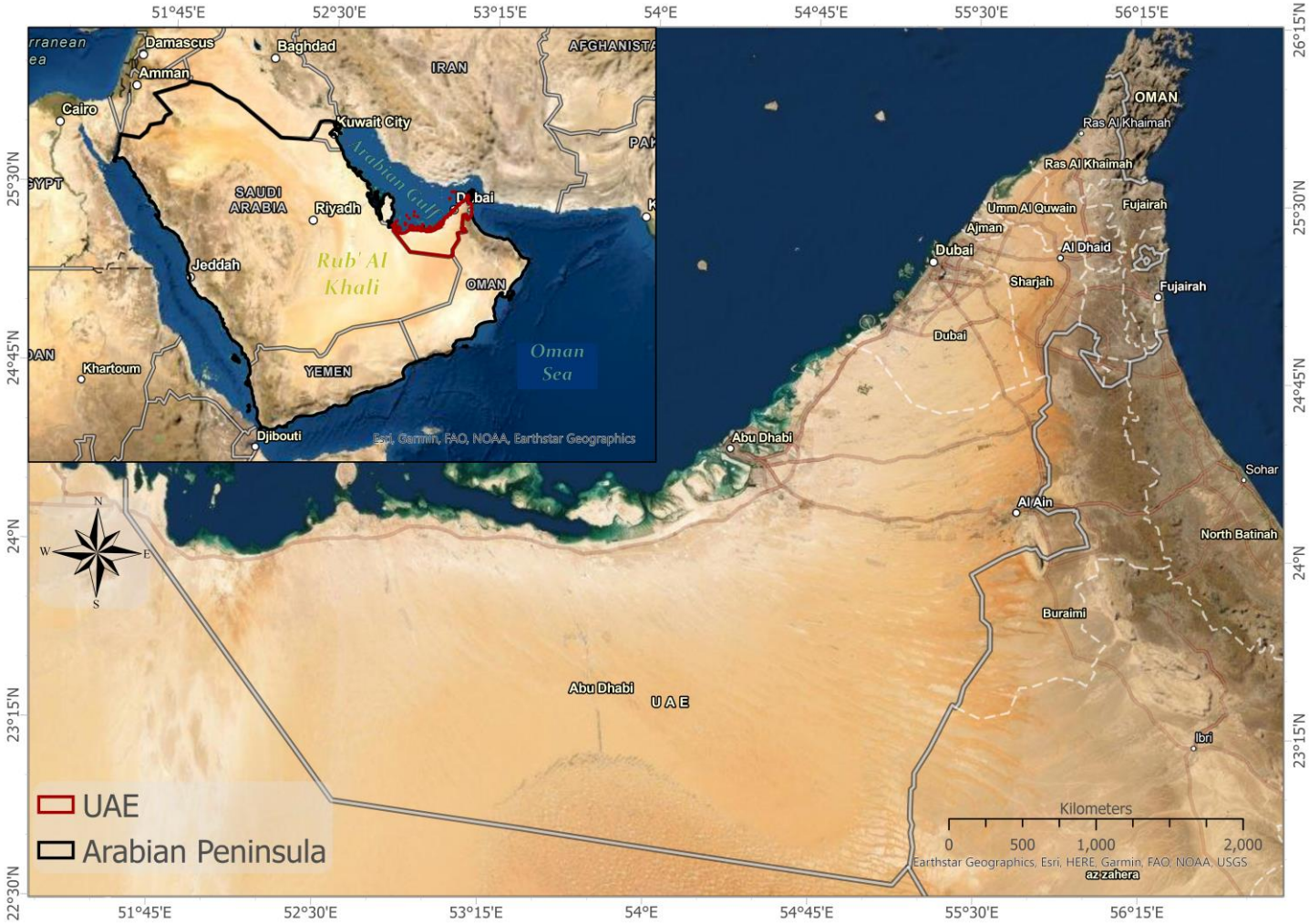

Figure 3.1: Location of United Arab Emirates.

3.3 InSAR Dataset & Analysis

SAR interferometry techniques were widely implemented to detect and monitor land surface deformations over various landcover types as discussed in chapter 2. Also, selecting the SAR dataset and InSAR technique depend on many factors that are related in most cases to the physical characteristics of the area under investigation. As shown in the previous section the UAE is covered mainly by sand dunes with urban and vegetated areas. This supports the idea of utilizing the SBAS technique to ensure that sand dunes will not decorrelate the signal and result in low PS density as in the case of utilizing the PSI technique. But the idea of utilizing the StaMPS technique was still possible due to its success in identifying a significant PS density over desert and vegetation landcover types but it requires a huge series of SAR datasets. Since the free SAR dataset from Sentinel-1 are massive and covered the targeted area for more than 4 years, then implementing the StaMPS technique with the available Sentinel-1 dataset could obtain a high PS density with reliable surface velocity measurements.

3.3.1 Sentinel-1 Dataset

Sentinel-1 remote sensing mission consists of two satellites constellation, Sentinel-1A and Sentinel-1B, at near-polar sun-synchronous orbit at 698 km above the Earth ground. Both satellites are located in the same orbit plane with 180 degrees phased in orbit. The Sentinel-1 mission is operating in C-band (5.405 GHz) with a repeat cycle of 12 days for each satellite and 6 days for the constellation. Sentinel-1 satellites operate in four SAR imaging modes (Figure 3.2); Interferometric Wide Swath (IW), Extra Wide Swath (EW), Stripmap (SM), and Wave mode (WV) with the

IW as the default mode (Yagüe-Martínez et al., 2016). IW and EW are characterized by a wide swath of 250 km and 400 km, respectively, while SM and WV are characterized by a narrower swath of 80 km and 100 km, respectively. The latter modes are characterized by smaller spatial resolution, 5 m for both range and azimuth, while the former modes are characterized by the range and azimuth resolutions of 5 m and 20 m for IW and 20 m and 40 m for EW, respectively. The IW, EW, and SM modes are supported by single polarization (HH or VV) and dual-polarization (HH+HV or VV+VH) while the WV is supported only by single polarization (HH or VV).

The SM mode covers a constant ground coverage and produces a swath width of 80 km with a spatial resolution of 5 by 5 m. This mode is capable of changing the incidence angle and elevation beamwidth to cover a new swath within the same azimuth and further in range. This capability is limited to six beams where six overlapping swaths can be generated to cover a whole range of 375 km.

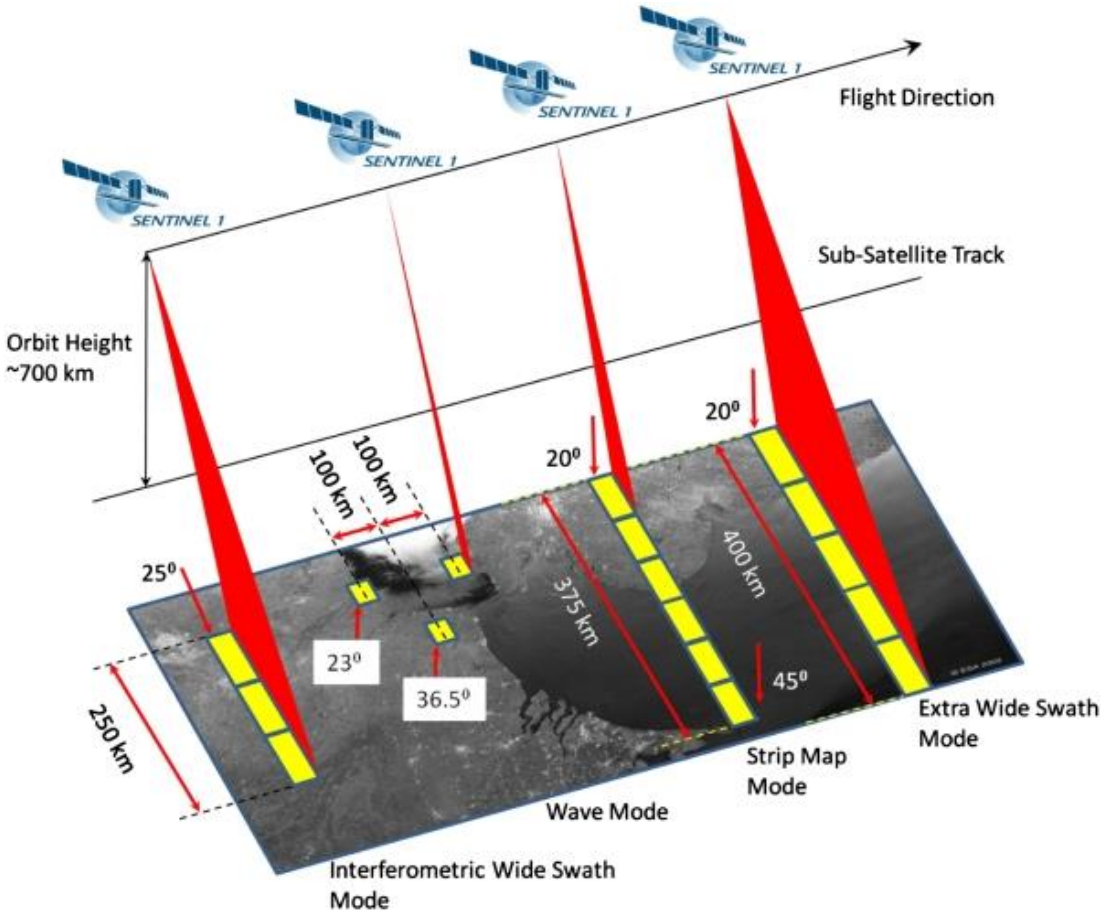

Figure 3.2: Sentinel-1 imaging modes

The IW mode is operating by implementing Terrain Observation with Progressive Scans (TOPS) to provide large swath width as ScanSAR mode with uniform SNR and Distributed Target Ambiguity Ratio (DTAR). TOPS reduces the azimuth resolution and scalloping effects by the antenna footprint effect to the ground target rather than antenna pattern slicing. This enhancement provides a better azimuth resolution because there is only one azimuth look available and balancing the radiometric look is not feasible. The IW mode, the default mode, divides the SAR Sentinel-1 scene into three sub-swaths by steering the antenna in the range direction and divides each sub-swath into nine bursts by steering the antenna electronically in

the azimuth direction. The antenna is switching from burst to burst to capture multiple sub-swaths pseudo-simultaneously (Torres et al., 2012).

In order to utilize TOPS SAR images for interferometry analysis, bursts synchronous is required between repeat-pass datasets. The burst duration for IW TOPS mode is ranging from 0.82 to 0.54 seconds. Antenna steering in azimuth direction results in Doppler Centroid (DC) variations of 5.5 kHz within bursts, so burst synchronous of less than 5 milliseconds is required. This requires a phase de-ramp after the co-registration process because the DC variations cause azimuth phase ramp for small misregistrations.

The EW mode is implementing TOPS, also as IW mode, but to cover a wider area. This mode is more suitable for maritime, e.g., polar regions, while the IW mode is more suitable for land. The WV mode is acquiring several scenes with either HH or VV polarizations as independent images. The same incidence angle scenes are separated in azimuth by 200 km and swath can be taken at near range angle (23º) or far range angle (36.5º). The WV mode is applied over the ocean where longwave mode data is captured per orbit.

3.3.2 InSAR Data Processing

StaMPS technique has been implemented via the StaMPS software package which does not generate the interferograms or pre-process the raw SAR data. For this purpose, another software was implemented, the ISCE developed by NASA at Jet Propulsion Laboratory, California Institute of Technology, in order to process raw SAR data into interferometric products. Pre-processing steps for SAR Sentinel-1 data are more complex than other SAR datasets due to it is imaging mode with TOPS. Sentinel-1 image characterized by three sub-swaths; each swath divided into nine

bursts. The complexity arises from the demand to pre-process each sub-swath individually then merge the three sub-swaths for each Sentinel-1 image in the selected dataset (Figure 3.3).

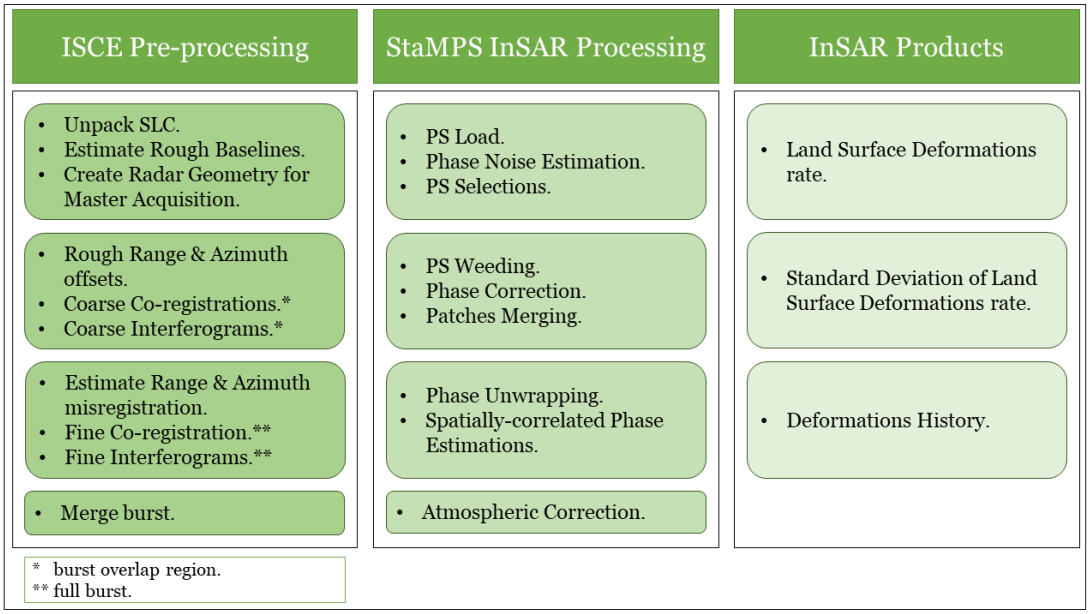

Figure 3.3: The InSAR processing steps using ISCE2 and StaMPS software packages.

The first step in the ISCE software to process Sentinel-1 image was to unpack the Single Look Complex (SLC) images and store each sub-swath in a separate folder that includes files for each burst. Then, define the matched bursts between master image and slaves images to estimate rough baselines. DEM data for the study area is required, along with the orbital information, for the co-registration process. SRTM data was used for this purpose. Since radar remote sensing is imaging in oblique mode, each image is recorded along its Line-of-Sight (LOS) and can be called a radar coordinate system. To avoid mislocation, unifying all images with the DEM into the master image LOS coordinate system was performed by computing pixel-by-pixel latitude, longitude, height, and LOS for master acquisition. Each data category was

stored separately for each burst and categorized in a sub-swath folder. Then, the overlap region between bursts was extracted and stored in a sub-folder to estimate coarse range and azimuth offsets for each burst overlap region. These offset values were implemented for coarse co-registration between master and slave for burst overlap regions only.

Furthermore, interferograms were generated for burst overlap regions, also known as coarse interferograms. In order to refine the co-registration and increase it is accuracy, the Enhanced Spectral Diversity (ESD) method was applied to estimate azimuth misregistration. While the range misregistration was estimated using amplitude correlation of burst overlap regions. The refined range and azimuth misregistration values were used along with the master radar geometry obtained at the beginning of the process to estimate fine offsets for full bursts. Moreover, fine offsets were used to generate fine co-registration between the master image and each slave image then generate fine interferograms. Finally, burst interferograms were merged to generate a full sub-swath interferogram. This process was iterated for the three Sentinel-1 sub-swaths to generate interferograms for the whole Sentinel-1 image scene. Generated interferograms were exported to the StaMPS software package to proceed with the InSAR time-series processing.

The imported interferograms to StaMPS were used in an iterative step to estimate the phase noise by modeling the topographic error. A threshold of 5 m was applied to increase the estimated coherence and the measured reliability. Within one squared kilometer from the selected pixels, 20% of the PSs with random phase were selected as PS candidates. A threshold of 1.0 was selected for the standard deviation of the phase noise for neighboring pixels to preserve PSs with low decorrelation signals. Then, the wrapped phase interferograms were corrected for spatially-

uncorrelated look angle error iteratively, bad interferograms were dropped, by filtering the phase in space to remove spatially-correlated components and re-estimate the spatially-uncorrelated component until the variance converge.

Furthermore, the wrapped phase interferograms were unwrapped using the 3D phase unwrapping technique to estimate the ambiguous cycles number. After that, errors related to spatially-correlated DEM were estimated and removed along with the master atmosphere and orbit error. Finally, the atmospheric phase component was corrected by implementing the open-source Toolbox of Reducing Atmospheric InSAR Noise (TRAIN) by phase-based linear correction (Bekaert, Walters, and Wright, 2015).

Processing huge Sentinel-1 SAR datasets for long time-series can be considered time-consuming and requires high-performance computing and large disk storage. Generally, analysis of a full Sentinel-1 SAR scene to produce time-series land surface displacements can take up to two weeks depending on the running machine. Reducing processing time for the InSAR analysis can be achieved by running the InSAR processing in a parallelized manner as discussed by Papoutsis et al. (2020). The implemented version for SAR dataset pre-processing and interferograms generation was the ISCE2 which uses a topsStack processor to create the co-registered SLC stack (Fattahi et al., 2017). The ISCE2 topsSatack processor creates a set of commands for the required steps for the co-registration processing. These commands can be used in batch processing to facilitate and reduce time processing for a huge SAR dataset. Parallelizing all processing steps is still infeasible due to the dependencies for some steps to complete the previous steps. The estimation of range and azimuth misregistration depends on using the co-registered stack of bursts overlap to create differential overlap interferograms (coarse interferograms). These commands can not

be executed in parallel due to their dependency on the previous steps. Moreover, the co-registration of full bursts (fine co-registration) requires the geometrical offsets and misregistration values for fine co-registration of full bursts. The fine co-registration step uses a subprocess that utilized all the available cores, so executing this step in parallel is infeasible as well.

The StaMPS technique divided the exported data from the ISCE software, the co-registered stack of SLC, into several patches of equal areas with a uniform grid to avoid the memory crashing due to a large number of PS candidates. Nonetheless, these patches are not equal in time processing because the number of PS candidates is different in each patch depending on the underlying landcover type. In most cases construction sites can be located adjacent to vegetated areas or urban areas can be surrounded by a desert and studying the land surface deformations over a specific location with surrounding areas is required, this could result in a big variation between adjacent patches in the PS density and eventually, big time-consuming in processing. The ideal concept to divide the co-registered SLC is by considering the number of the PS candidates so all patches consume almost the same time processing. This approach divides the study area into *n* groups of patches for *n* cores of the running machine which can be executed simultaneously and reduce the processing time. The standard patches division included in the StaMPS was used first to divide the study area into equal areas, then patches were aggregated into groups according to their PS candidates numbers. This approach reduces the time-consuming for StaMPS steps 1-5, but it does not divide the patches into equally sized groups because of the inherent inequalities in the patches division.

StaMPS steps 1-5 can be processed in a parallelized way by running the same procedures simultaneously on the balanced groups of patches. The parallelized

approach showed a significant reduction of time-consuming for the whole SAR interferometry processing from capturing the SAR dataset to obtaining land surface deformations. The InSAR processing for the full Sentinel-1 scene takes about two weeks using the sequential approach, the parallelized approach completed the processing within 6 days. The parallelization approach for the InSAR processing was implemented by Python libraries for controlling process steps in ISCE2 and StaMPS software packages.

3.4 InSAR Investigation over the UAE

Investigations of land surface deformations over the UAE have been performed by implementing the processing chain presented in (Figure 3.3). The investigations have been conducted with the Sentinel-1A SAR dataset, where 3 scenes cover the UAE as shown in Figure 3.4. The UAE territory can be divided, according to the Sentinel-1 frames, into North (Path 130 Frame 78), Center (Path 130 Frame 73), and West (Path 28 Frame 72) frames. The processing chain has been implemented for each frame sequentially. The Sentinel-1 SAR dataset utilized for the processing was 291 SLC images acquired in the period between March 2017 to March 2021.

The North frame covers the northern emirates of the UAE, shown as a green rectangle in Figure 3.4, where land cover types are generally desert, built-up, vegetation, and mountains areas. This frame does not cover any land in the upper left triangle where it covers the Arabian Gulf. The processing succeeds in identifying more than 11 million (11,083,237) PS candidates. The SAR image acquired on March 22, 2019, has been selected as the master because of its smallest geometrical and temporal baselines. Due to the larger part that is covered by the sea, more than half of the frame is covered by the Arabian Gulf, the parallelized processing faced some technical

issues. The original StaMPS package was programmed to divide the area of interest into equal-area patches with at least one PS candidate at each patch. The proposed method to divide the area of interest into patches with a similar number of PS candidates results in generating patches with zero PS candidates.

Also, because the numbering of patches is completely random and does not follow spatial consideration, identifying the empty patches was not straightforward. This issue has been solved by running the parallelized StaMPS iteratively over a group of patches according to their PS candidates. The first iteration of the parallelized StaMPS showed the number of PS candidates at each patch and the empty patches have been excluded from the processing. The rest of the iterations were performed to avoid memory crashing due to high variation between time processing for patches because there was a big difference in the PS candidates between these patches. The variation in the PS candidates between patches occurred at the east and northeast of the North frame where mountains are located, in contrast with the south and southwest of the North frame where the land cover is desert.

The above-mentioned technical issues consumed more time processing than expected for this frame. This results in the longest time consumed between the three frames of 15 days from pre-processing to obtain the LOS deformations rate. The processing of the North frame required disk space of 2 TB including the raw SLC Sentinel-1A images and the intermediate files, but after removing all intermediate files the disk space was 387 GB excluding the raw SLC dataset.

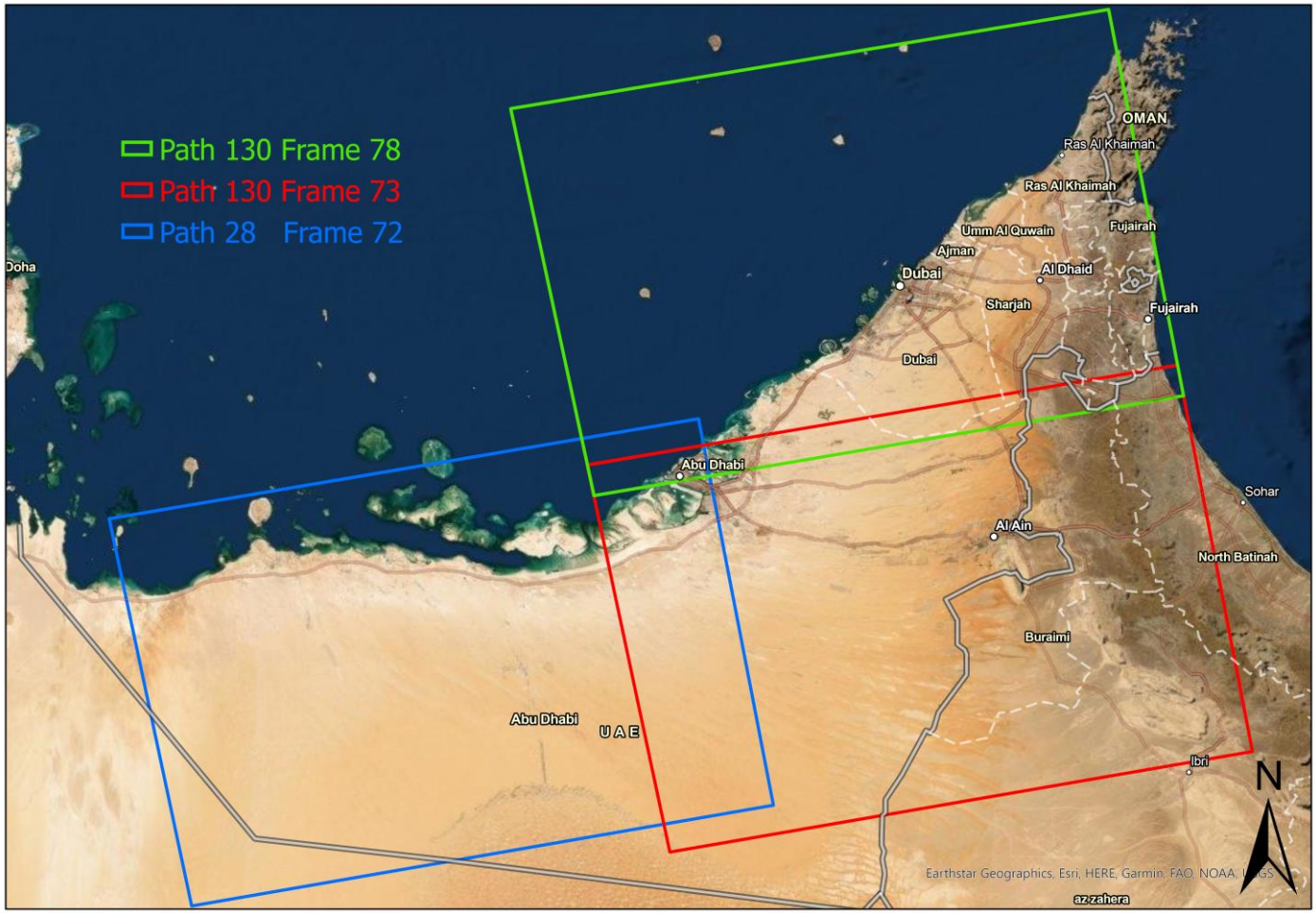

Figure 3.4: Sentinel-1A frames cover the UAE. The North, Center, and West frames are shown as green, red, and blue rectangles, respectively.

The Center frame covers the middle and east parts of the Abu Dhabi Emirate, shown as a red rectangle in Figure 3.4, where Abu Dhabi city is located at the west of the Center frame with the Arabian Gulf and the Al Ain city is located at the east with international border with the Sultanate of Oman. This frame covers land cover types of built-up, vegetation, desert, and mountains areas where the most dominant land cover type is the desert. Mountains are represented by the Jebel Hafit at the east and Oman Mountains where they are located outside of the UAE boundaries.

In the Center frame, more than 15 million (15,991,204) PS candidates have been identified. The selected master image for the Center frame was on the same day as for the North frame (March 22, 2019) for the same reason. The processing of the Center frame faced slow progress due to the huge amount of PS candidates over the Oman mountains. Since these patches are located outside of the targeted area they have been excluded after they have been identified using the iterative procedures as explained in the North frame processing. This iteration increased the time processing for this frame the expected time consuming when it took 12 days from pre-processing to obtain the LOS deformations rate. The processing of the Center frame occupied 2.4 TB of the disk space including the raw SLC Sentinel-1A images and the intermediate files, but after removing all intermediate files the disk space was 592.1 GB excluding the raw SLC dataset.

The West frame covers the Al Dhafra Region of the Abu Dhabi Emirate, shown as a blue rectangle in Figure 3.4, where small cities are located such as Madinat Zayed, Ghayathi, and Al Ruwais. This frame covers a small part of the Arabian Gulf with small islands such as Abu Al Abyad Island at the north and most of the land cover type is the desert with vegetation areas at the south (Liwa).

Finally, the processing of the West frame has identified more than 6 million (6,552,059) PS candidates. For the West frame the image acquired on April 08, 2018, was selected as the master image due to its smallest geometrical and temporal baselines. The processing of this frame was the fastest one with the typically expected time processing of 6 days from pre-processing to obtain the LOS deformations rate. The processing of the West frame occupied disk storage of 2 TB including the raw SLC Sentinel-1A images and the intermediate files, but after removing all intermediate files the disk space was the least one with 109.6 GB excluding the raw SLC dataset.

3.5 Land Surface Deformations over the UAE

The InSAR techniques have been performed using ISCE2 and StaMPS software packages with the Sentinel-1 SAR dataset to detect land surfaced deformations over the UAE in the period between March 2017 and March 2021. The StaMPS technique succeed in identifying more than 30 million (33,626,494) PS candidates over the UAE. The detected land surface deformations showed a significant land surface subsidence in several areas over regional and local scales in the UAE (Figure 3.5).

The detected land surface deformations over a regional scale were land surface subsidence in the Al Ain and Al Dhafra regions at the east and west of the Abu Dhabi Emirate, respectively. The former regional land surface subsidence phenomena were the highest detected land surface deformations with a maximum subsidence rate of -55 mm/year. The later regional land surface subsidence phenomena were medium land surface deformations with a maximum subsidence rate of -20 mm/year.

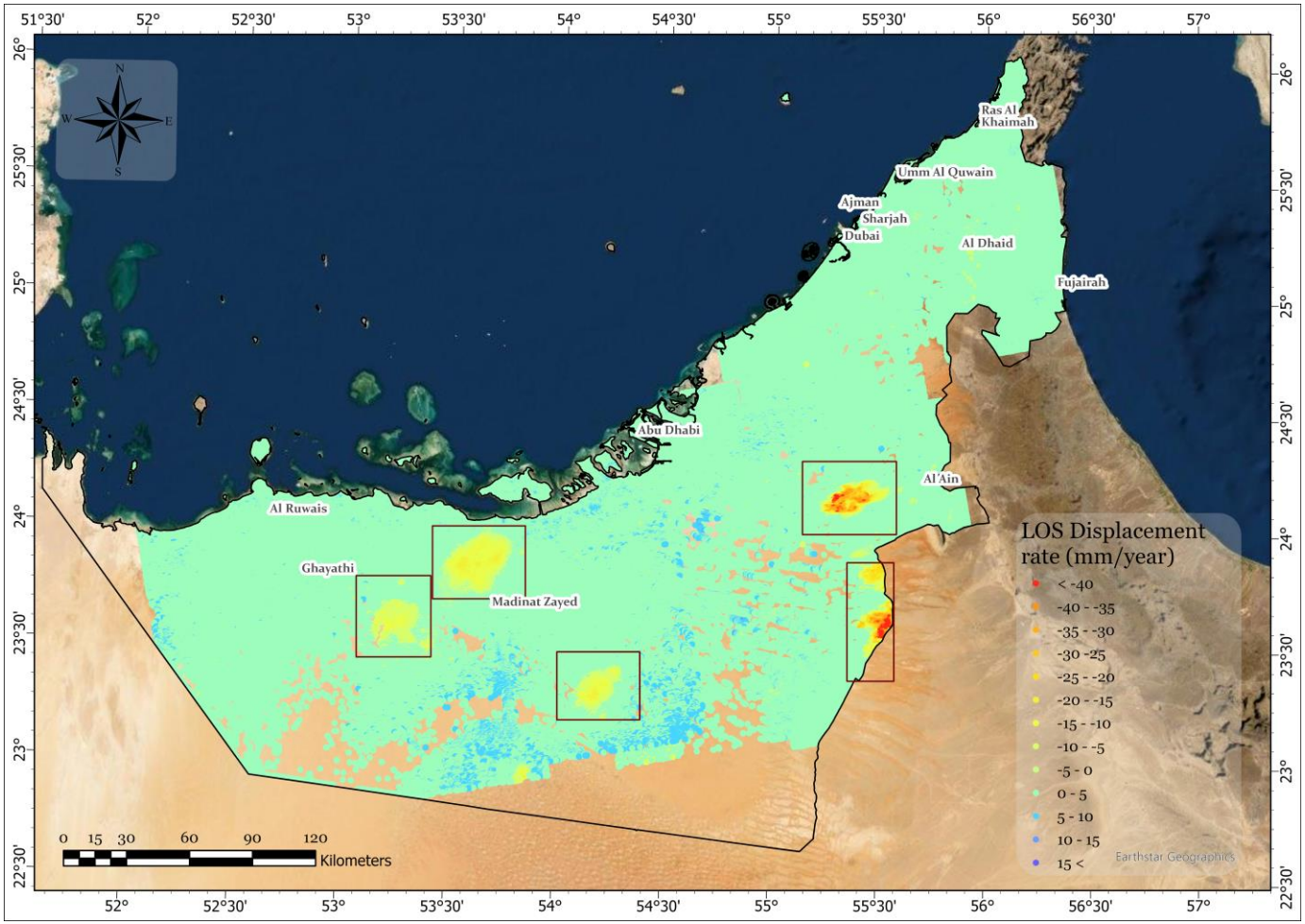

Figure 3.5: LOS displacement over the whole UAE. Yellow and red colors represent land surface subsidence while green and blue colors represent the stable ground. The red rectangles show the regional land surface subsidence.

The maximum land surface subsidence over the Al Ain region has been detected over the Remah, Al Araad, and Al Wagan areas. These areas are characterized by agricultural activity since the 1980s'. Moreover, due to the lack of resources for surface fresh water in these areas, farmers have relied mainly on groundwater resources for irrigation purposes. Deep details are provided in the next chapter where more InSAR investigations with groundwater data and field observations have been conducted over the agricultural areas in the Al Ain region.

The land surface subsidence over the Al Dhafra region has been detected over three distinctive zones; north of Madinat Zayed, east of Ghayathi and west of Madinat Zayed, and Asab at the southwest, as shown in Figure 3.5.

Moreover, smaller land surface subsidence phenomena were observed over different locations in the Northern Emirates such as Al Dhaid, landfill location south of Dubai, and industrial area in Sharjah (Figure 3.6). Al Dhaid is a city in the Sharjah Emirate located in the east part known for its safari park and the craggy outcrop of fossil rock. Also, there are farming activities in the Al Dhaid area where dates palms and fruits were cultivated (SEWA, 2018). The maximum detected land surface subsidence was at a rate of -12 mm/year in the southern part but it extends toward the south of the Al Dhaid city and covers the safari park area (Figure 3.6 (a)).

A faster land surface subsidence rate has been observed over a landfill, known as Al Bayada Landfill, located in the Dubi Emirate near Dubi-Al Ain Road (E66) with a maximum rate of -15 mm/year (Figure 3.6 (b)). Land surface subsidence at a landfill site can be attributed to two mechanisms; mechanical compression and biochemical processes. The former is occurred because of the primary consolidation and secondary compression of the waste material mass. While the latter is occurred due to the organic

matter decomposition. Both mechanisms result in voids and pores collapsing by oxidation, corrosion, or decay of water materials.

Finally, a slow land surface subsidence has been detected over the industrial areas in the Sharjah Emirate, Emirates Industrial City and Sajaa Industria Area. The detected land surface subsidence was in the order of -7 mm/year in the middle of the Industrial area and -4 mm/year around the Industrial area (Figure 3.6 (c)). The main industrial activities in the industrial area are car customizations, auto-used spare parts, and warehouses.

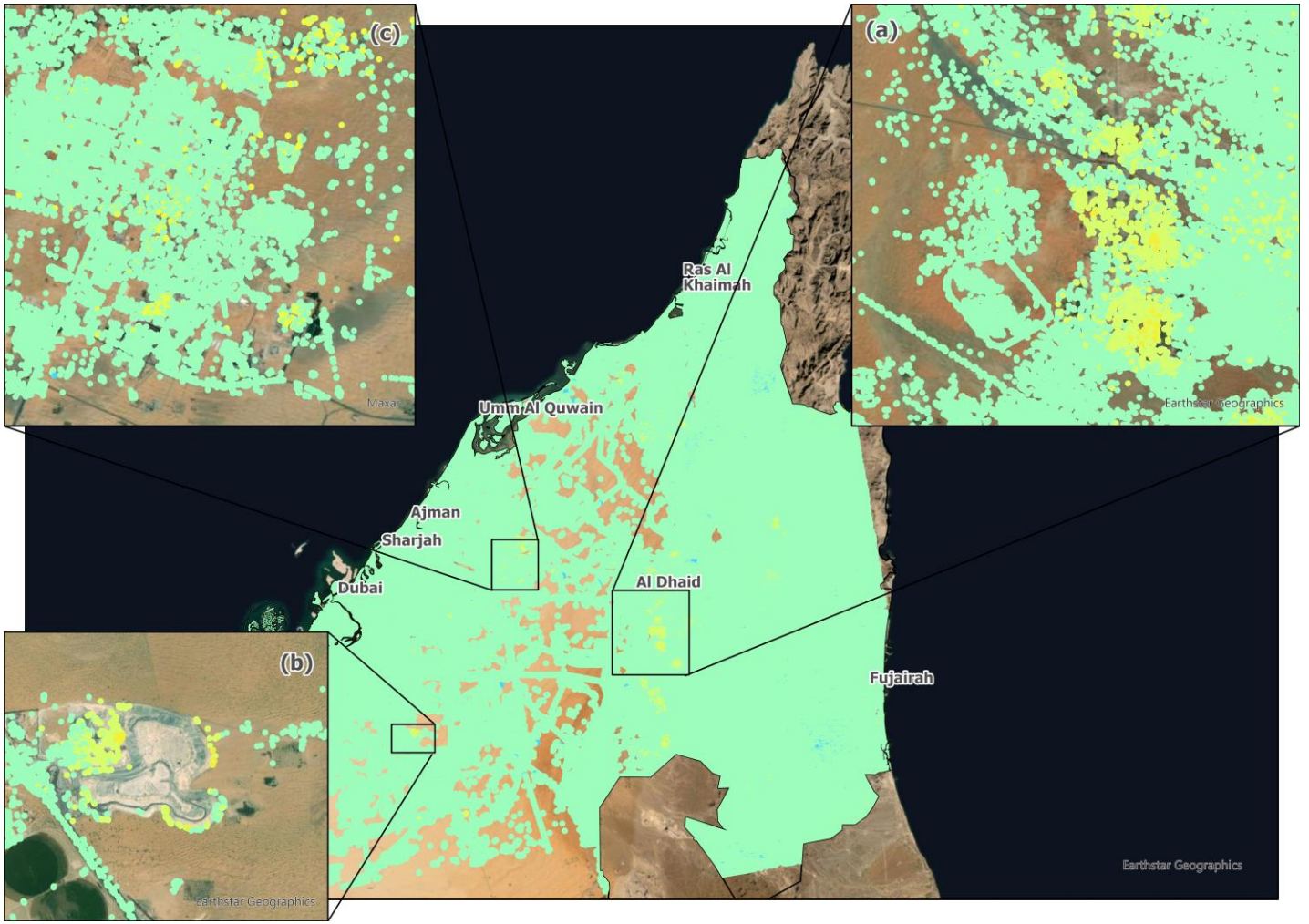

Figure 3.6: Small land surface subsidence over the Northern Emirates. (a) Al Dhaid. (b) Al Bayada Landfill. (c) Sharjah Industrial Areas.

Chapter 4: Land Surface Subsidence over Agricultural Areas

4.1 Introduction

In the Emirate of Abu Dhabi, about 89% of groundwater wells are used for agriculture and forest irrigation. Accordingly, to monitor the change of groundwater level and salinity, the government of the Abu Dhabi Emirate initiated the project Groundwater Wells Inventory and Salinity Mapping for Abu Dhabi Emirate (EAD, 2018).

The big challenge facing the UAE is the overexploitation of groundwater resources which can result in environmental impacts, such as altering the hydrological system, degradation of vegetation, land surface deformations, and water quality deterioration (Zektser, Loáiciga, and Wolf, 2005). Monitoring the groundwater level in the UAE is systematically achieved by establishing a well-distributed network of monitoring wells (Taylor and Alley, 2002). Nevertheless, a corresponding network, or at least random measurements or studies, for detecting possible surface deformations due to overexploitation of the aquifers are not available. Measuring the effect of groundwater change on the land surface has been under investigation for decades with well-known techniques, such as survey leveling, GPS, and InSAR. Utilizing satellite remote sensing, SAR missions, for monitoring land surface deformations provide larger spatial coverage than the traditional techniques with a millimetric resolution of the deformation (Galloway and Burbey, 2011).

This chapter shows a study of assessing and monitoring groundwater storage and its impact on the land surface in the Al Ain region, specifically over the Remah area, in the UAE using primarily remotely sensed and ground truth data.

4.2 Geology & Hydrogeology of Remah Area

Remah is located in the Al Ain region 43 km east of Al Ain city, Emirate of Abu Dhabi. The Remah area is characterized geomorphologically by a desert cover, with elevation ranging from 80 m a.s.l., in the west, up to 200 m a.s.l., in the east. The area illustrates a series of sand dunes disconnected by flat areas known as interdunes. On the east side of the study area, there is high topography represented by the Jabal Ha fit and Al Hajar Mountains, south and east of Al Ain city respectively, while in the west the elevation is decreasing gradually towards the Arabian Gulf.

The Remah area is occupied by three geological formations: the Barzaman formation, Hili formation, and Rub' al Khali formation (EAD, 2018). Beneath the Barzaman formation, a layer of limestone interbedded with anhydrite, dolomite, and mudstone appears in some well lithological profiles (Figure 4.1). This layer is discontinuous through the study area and it is older than the Barzaman formation. The study area is tectonically inactive, as there is no evidence for such activity (Yagoub, 2015).

The Barzaman formation is barely exposed on the surface around Abu Samra. Its thickness is around 200 m in the north of the study area, decreasing consistently towards the south of the study area. The Barzaman formation is composed of fluvial sedimentary rocks with conglomerates as the major constituents. It has four coarse-grain lithofacies; two are conglomerates with different types of clasts. The dominant one contains the minor size of clasts with white carbonate matrix, while the other conglomerate contains boulder brown clasts probably from mafic and ultramafic clasts. The other lithofacies are fine-grain of mottled Dolomitic Mudstone and angular

breccia with high plasticity silt (Thomas, Finlayson, Smith, Arkley, and Farrant, 2012). The Barzaman formation is unconformably overlaid by the Hili formation.

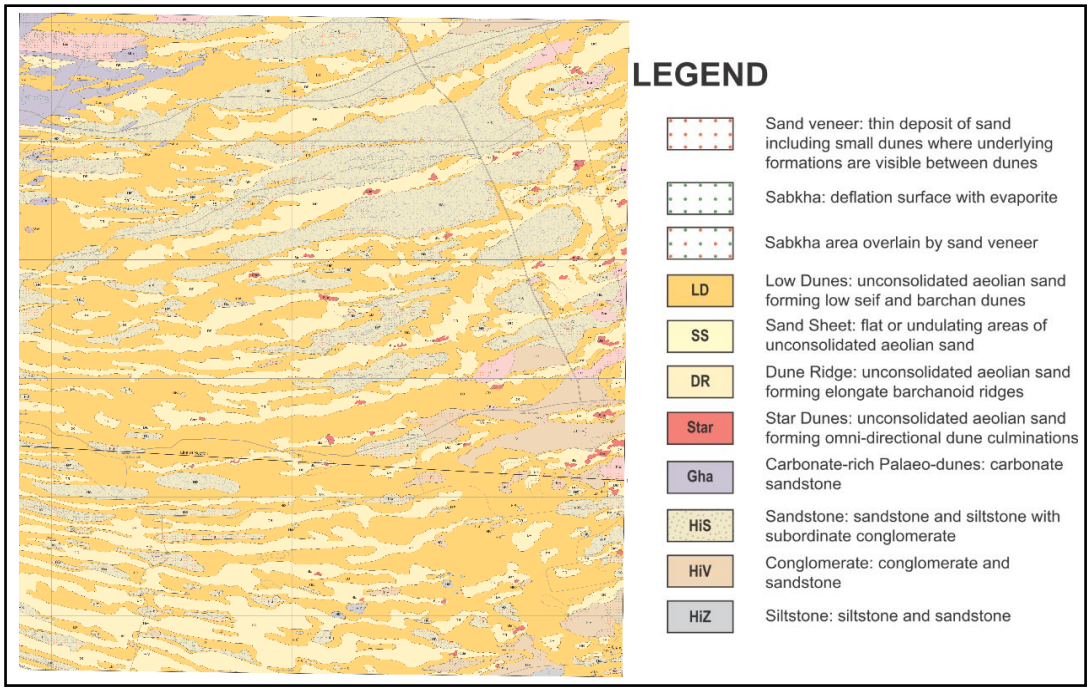

Figure 4.1: Geological map of the Remah area (Thomas et al., 2012).

The Hili formation is clearly observed between sand dunes and it encompasses three lithological units: conglomerate and sandstone, siltstone and mudstone, and sandstone and siltstone with the secondary conglomerate. The Sandstone is characterized by lenses of silty, sandy, gravely, and pebbly conglomerate (Khan, Kalbus, Alshamsi, Mohamed, and Liaqat, 2019). The conglomerates encompass clasts from UAE-Oman ophiolite (Hajar Mountains) which is sub- to well-rounded serpentinite and micro gabbro. The texture of the Hili formation is coarse to fine from the east at the Hajar Mountains to the west, where the depositional environment over sandy covers to deposit siltstone and mudstone. The thickness of the Hili formation is consistent along the Remah area, being less than 100 m.

The most covering formation of the study area, and the UAE in general, is the Rub' al Khali formation, which is sand dunes composed of unconsolidated fine to medium grain sand. The study area contains three types of dunes: Dune ridges, Star Dunes, and Low Dunes (Thomas et al., 2012). Finally, the superficial deposits consist of a thin layer of sands, also called sand veneers, and sabkhas. A sand veneer can accumulate to form low dunes or encroach over the interdune areas.

Generally, it has the same composition as the nearby dunes; carbonate in the west and rich in quartz (dark orange) in the east. Sabkha is the surface where the wind has sagged the ground by erosion above the water-table level within the capillary zone. Due to evaporation, sabkha is composed of secondary gypsum form over superficial deposits.

The geological formations of the wider Abu Dhabi Emirate, according to the United Arab Emirates National Atlas (Embabi, Yahia, and Al Sharhan, 1993), bear four hydrological units: (1) the carbonate aquifers occupying the macro permeable carbonate formations in the east side of the Emirate, along the borders with Oman, (2) the western gravel aquifer, at the high permeability gravel formation along the foothill of the Al Hajar Mountains, also in the east, (3) the sand dune aquifer occupying the sand dunes' area covering most of the Emirate, and (4) the coastal aquifer, at the coastal Sabkhas, in the west.

The narrow study area is located at the sand dune aquifers unit. The unconfined aquifers of the area occupy the coarse grain layers of the above-described formations and they are fed laterally by the carbonate aquifers extending in the east. Practically, the groundwater of the deep carbonate aquifer recharges the sand dune aquifers either directly or through the western gravel aquifer.

Al-Ain region is known as the agricultural region in the Abu Dhabi Emirate, with 50% of the agricultural activities of the emirate located there. The area under investigation holds 553 farms, 524 of which are active, occupying an area of 20.5 and 19.5 km^2, respectively. Generally, farms in the study area plant fruits (figs, mango, pomegranate, etc.) and crops (fodder, cabbage, corn, tomato). Besides farms and crops, there is the forest cover for windbreaks which holds an area of 0.078 km^2 (ADAFSA, 2019).

These agricultural activities are supported by an extensive network of water wells exploiting the underground water. The groundwater, although unsuitable for irrigation due to its high salinity, is the only source of water in the area. The average depth of the water table in the shallow aquifer ranges between 52 and 67 m at the narrow study area, due to overexploitation, with annual water discharge of 244 million m^3 from the aquifers forming a depression cone reaching further down to the depth of 120 m (EAD, 2018).

4.3 Materials & Methods

4.3.1 Dataset

The water level dataset for the Remah area for the period between 2013 and 2019 has been provided by the Environment Agency of Abu Dhabi (EAD). The generated piezometric contours for this dataset uncovered a huge ongoing depression cone as shown in Figure 4.2. The steep decline in water level in 2013 indicates that the water level drawdown was in development before the captured depression cone in 2013. It is clear that the irrigation wells network has been systematically affected the unconfined sand dune aquifers and resulted in declining the groundwater level with a

maximum drawdown up to 50 m at the center of the depression cone. The water level drawdown is gradually decreasing away from the center of the depression cone, but it is steeper toward the east than the west. This drawdown can be controlled by many factors; pumping rate, aquifer characteristics, lithology, and recharge. As the sand dune aquifer is the upper aquifer in the study area, it is expected to have a wide area affected by the depression cone, especially around the irrigation wells, because of the high groundwater discharge (244 million m^3 per year) and the high permeabilities sand formations. EAD reported that 95% of the water wells in the Remah area are used for farming activities and this is in agreement with the depression cone that is extensive over agricultural areas.

The Sentinel-1 SAR datasets have been extended to cover the period between March 2015 and March 2021 to deeply investigate the detected land surface subsidence over the Remah areas, presented in the previous chapter, and to overlap the time period of the provided water level dataset. The available Sentinel-1 SAR datasets for this area are exceeding 130 images and a subset of 97 images was processed. All SAR SLC images processed were acquired along ascending direction because of the low number of acquisitions along the descending direction, only 15 scenes during the same period.

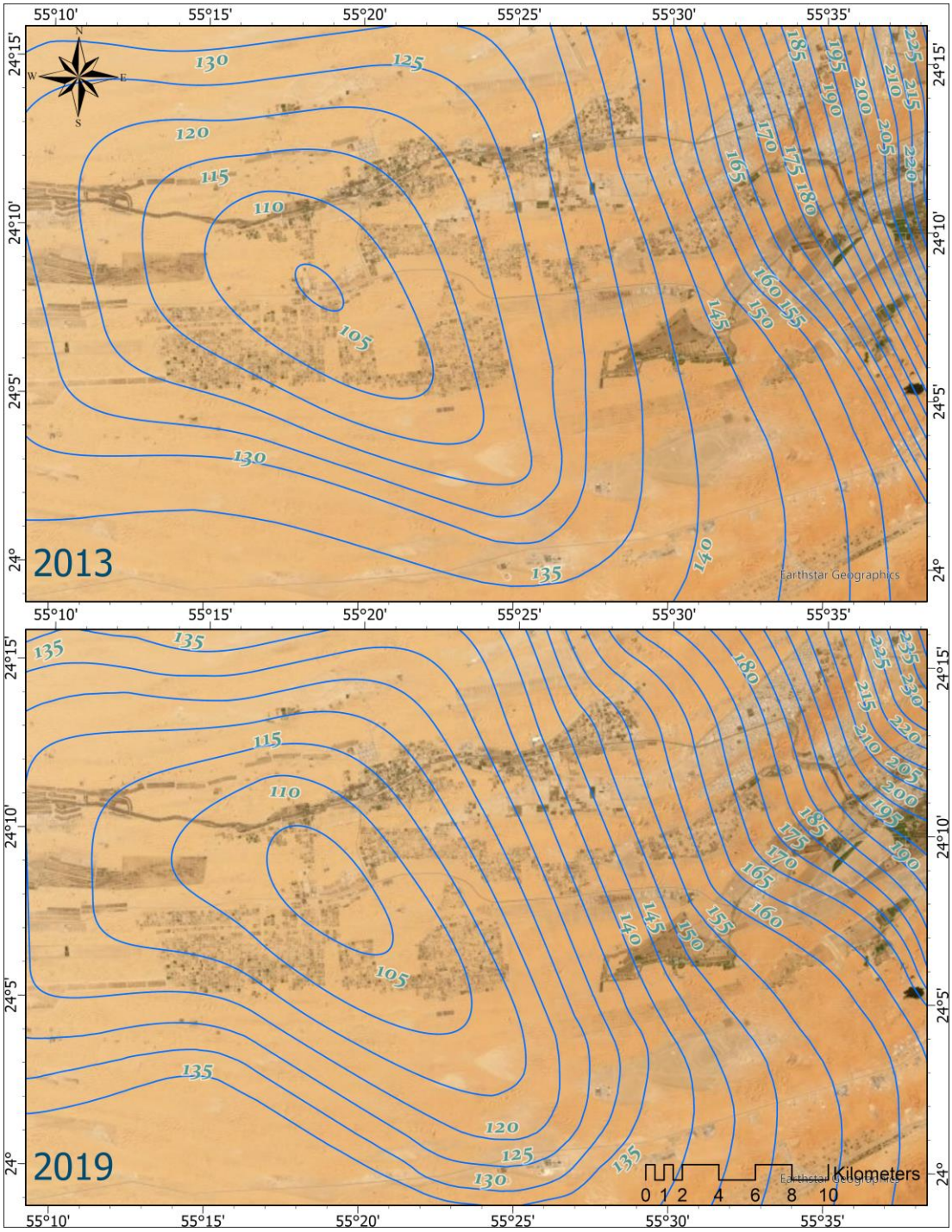

Figure 4.2: Groundwater level contours over the Remah area represented by dotted blue lines in 2013 (top) and 2019 (bottom). The depression extended between 2013 and 2019.

4.3.2 InSAR Data Processing

The InSAR processing chain has been applied as discussed in the previous chapter but for a smaller area to study only the land surface subsidence over the agricultural zones of the study area and their surroundings. The master image was selected that acquired on March 1, 2018, due to its smallest spatial and temporal baselines. The spatial, or perpendicular, baselines have a maximum value of 124 m.

The only change in the pre-processing with the ISCE software package was the definition of the narrow study area to restrict the pre-processing from applying the commands for the entire scene.

Geomorphology of the Remah area showed a generally flat terrain with sand dunes and interdunes. Thus, the threshold for the modeling topographic error can be high because there is not much height variation within the processed area. For this reason, a threshold of 20 m was applied to model the topographic error, and 25 % of PSs with random phase were selected, in order to increase the PS density. This PSs selection has been refined by a threshold for the interferometric noise standard deviation of 1.0 which maintained the PSs selection to pixels with lower decorrelations.

4.3.3 Field Observations

Detecting and monitoring of land surface deformations phenomena require field observation survey because identifying the slow deformation rate is feasible only by noticing the deformations and failures of the constructions over the deformed area. So, field visits have been conducted on January 31, 2020, to the Remah area in order to observe and identify signs for damaged and/or failure constructions. These field

visits concentrated around farms and known water wells, but as well observations were taken over the town to identify the effect over non-agricultural areas (Figure 4.3).

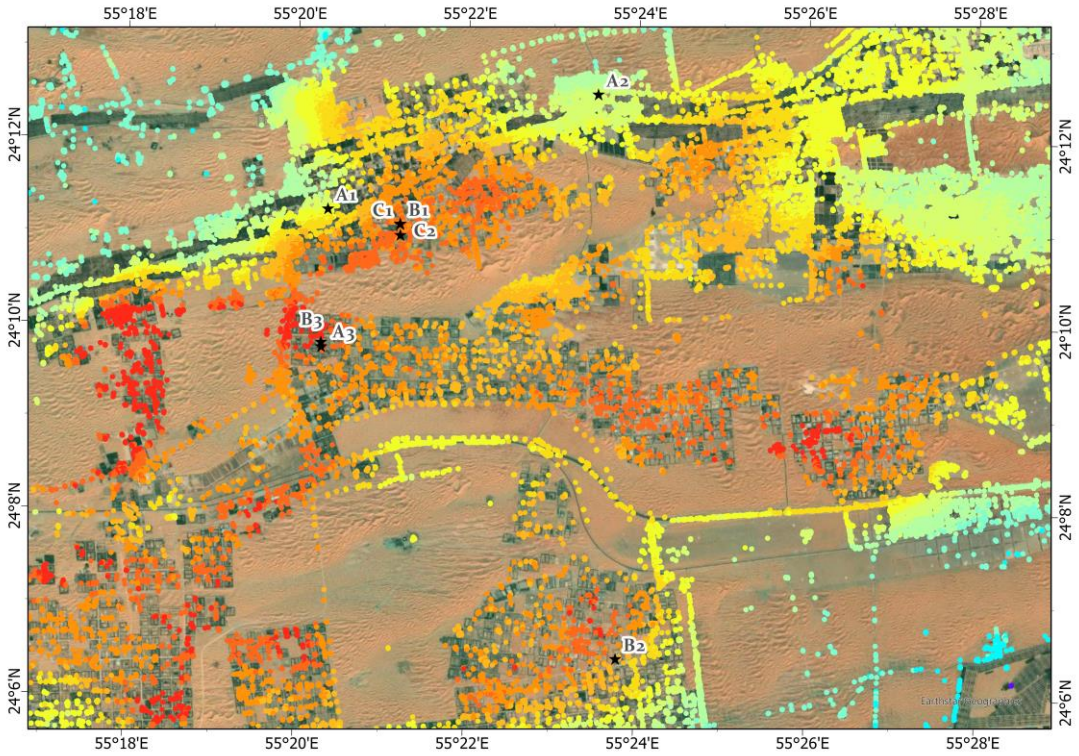

Figure 4.3: Locations of the observed land surface subsidence signs.

The first observed sign for the land surface deformations was the fractured walls of so many constructions as well as leaning walls in some fences (Figure 4.4). This observation can occur due to differential settlements of the construction's foundations. This type of land surface deformation can be evidence of failure at the construction over the deformed area.

The second observed sign was the protrusion of some constructions due to the land surface subsidence. As presented in (Figure 4.5) the concrete bases around the water well casings appear cracked as despite the lowering of the ground surface the water well casings remain stable lifting up and cracking the surrounded concrete, the

casings remain stable because it is based deep down on an undeformed layer. A typical deformation has been observed over a small building as shown in Figure 4.5.

Figure 4.4: Examples of differential settlements of the construction's foundations.

Figure 4.5: Examples of constructions protrusion due to land surface subsidence.

Furthermore, the electrical pillars in the deformed areas have been observed inclined with tension in the wires showing clear evidence for land surface subsidence (Figure 4.6). This can occur as ground lowers in some locations more than others and subsiding electrical pillars stresses the wires and pull other electrical pillars.

Figure 4.6: Examples of inclined electrical pillars.

4.4 Surface Deformations Results

The utilization of the StaMPS technique with the available Sentinel-1 stack over the Remah area, which is characterized by fewer anthropogenic structures, resulted in high PS density (4000 PSs/km^2) as suggested in the processing of the whole UAE. Moreover, this proves the ability of the StaMPS approach in identifying PS scatterers over desert areas even with vegetation landcover. The InSAR processing detected land surface deformations ranging from +5 to -60 mm/year between March 2015 and March 2021 in the LOS direction (Figure 4.7). The detected displacement can be considered vertically with no horizontal displacement due to the absence of the tectonic activities in the Remah area (Yagoub, 2015).

The detected land surface deformations over the Remah area appeared as a land subsidence bowl with its major axis extending from the northeast, at the Al Saad city by 14 km, to the southwest, by 15 km from Remah city. As expected, the maximum subsidence rate was -50 mm/year at the center of the bowl and it decreases gradually towards the edge of the bowl with a subsidence rate of -10 mm/year.

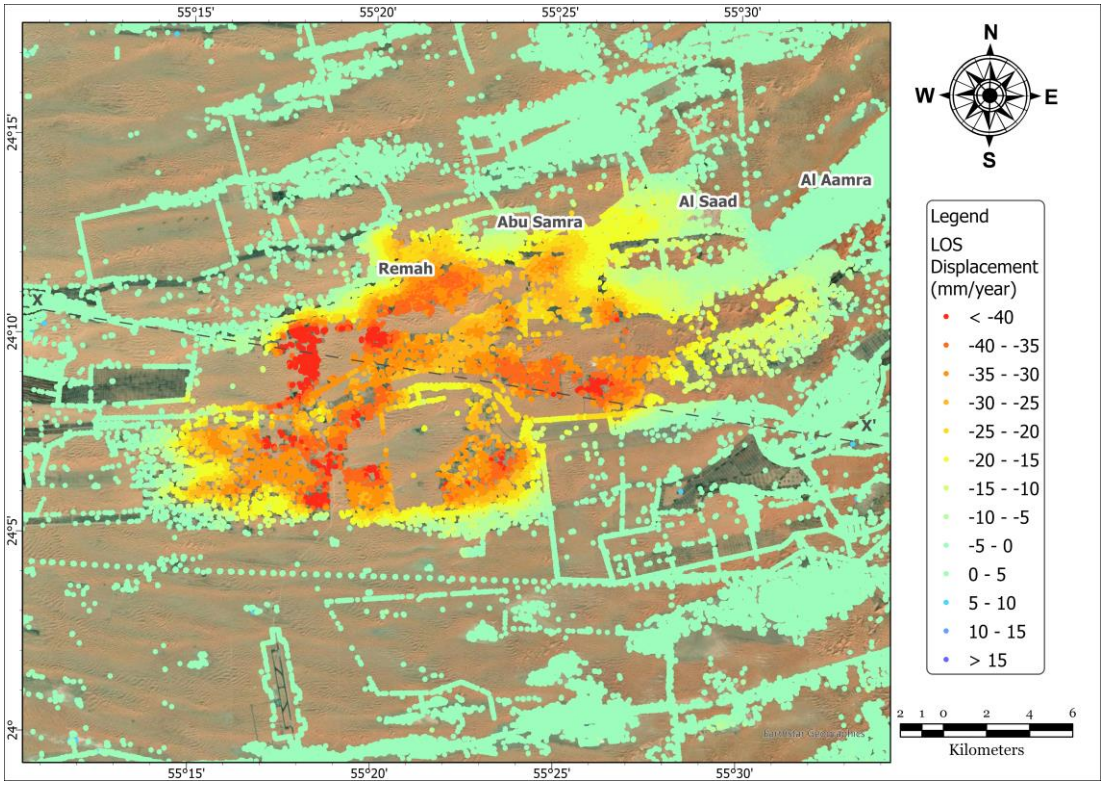

Figure 4.7: Land surface subsidence in LOS direction between over Remah 2015 and 2021 measured in mm/year. The red color represents a higher subsidence rate.

In order to illustrate the subsidence laterally, a cross-section has been generated along X-X' line shown as a grey dashed line in Figure 4.7. This line has been drawn along the longest diameter of the subsidence bowl. The cross-section is trending from the west (X) to the east (X') which is presenting steep subsidence from the east (Figure 4.8), the land subsidence changed from -5 to -60 in 2.7 km, and less steep from the west, the land subsidence changed from -2 to -43 mm in 6.1 km, toward the center. The maximum subsidence was detected toward the west where the subsidence rate was steeper.

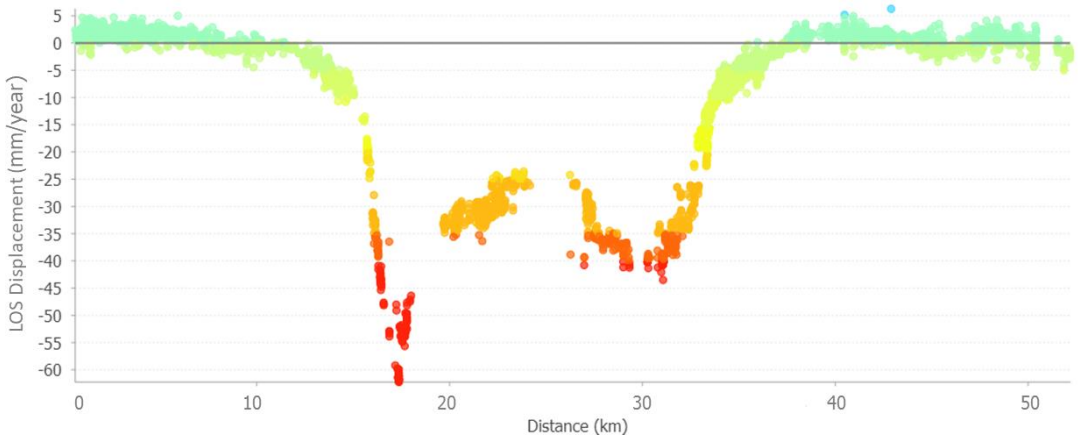

Figure 4.8: Cross-section along X-X' shown as a dotted grey line in Figure 4.7.

4.5 Discussion

Implementing the StaMPS technique showed a significant PS density in the study area which can produce more reliable surface deformations measurements. But StaMPS technique relies on a linear model to estimate the time-series surface deformations for the selected PSs. This means that if the deformations rate is non-linear within the deformed area, then the measured deformations can deviate from its the actual value. In order to assess the measured deformations rate, the standard deviation for the measured deformations rate was computed, which represents a reliable deformations rate measurement when the standard deviation is low. On the other hand, when the standard deviation is high that means either the selected PSs have incorporated a high level of noise or the linear model of the deformation has not fitted well and the estimation of deformations rate by the linear model is not feasible.

In our processing, however, the standard deviation at the subsidence bowl was about 2 mm/year (Figure 4.9) which makes the land surface subsidence rate be expressed as -60 mm/year ±2 mm/year. This indicates that there is no evidence for non-linear deformations over the Remah area during the studied period.

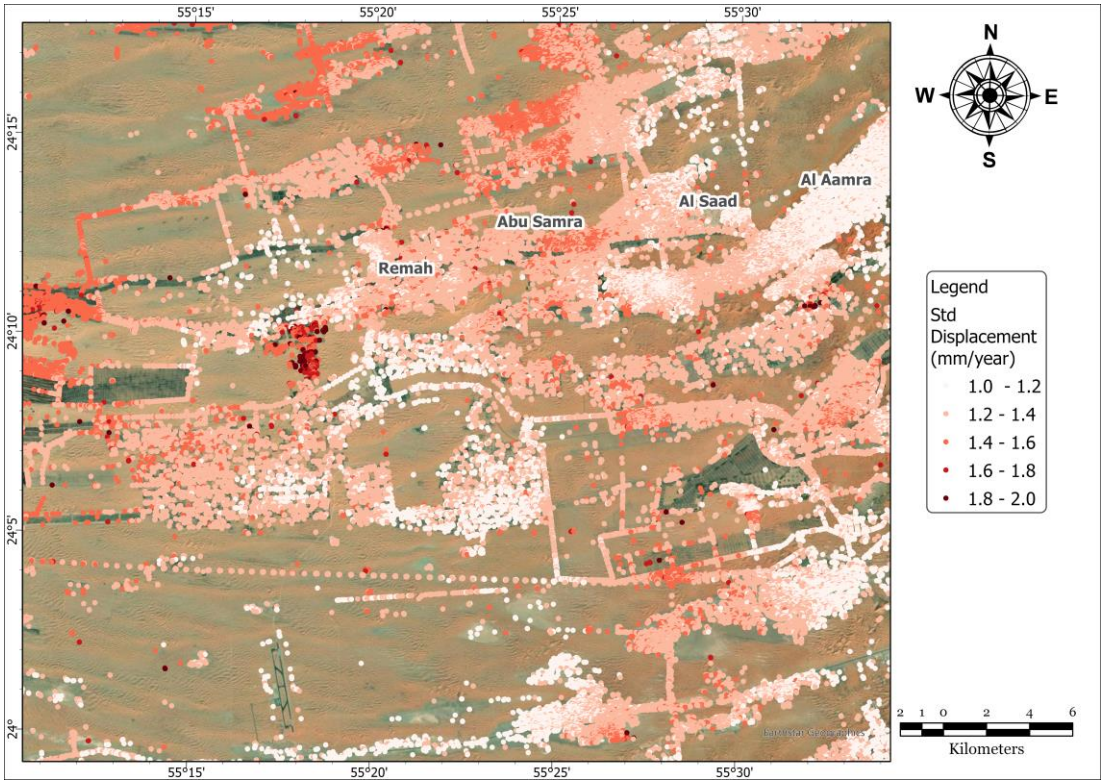

Figure 4.9: Subsidence rate standard deviation for values shown in Figure 4.7.

Since the establishment of the country of the UAE, the Remah area was one of the destinations for crops cultivation. This can be attributed to first the abundant flat areas between sand dunes, known as interdunes, where growing crops are feasible, and second to the available amount of groundwater. In contrast with the surrounded areas, the Remah area is characterized by a higher number of interdunes, higher groundwater saturated thickness, and lower hydraulic conductivity 1 m/day (EAD, 2018). Remah area is located almost in the middle of the UAE where no surface water is available, the closest source of surface water is Al Ain Al Fyadah spring which is located more than 30 km east of the study area (Othman, 2005). Thus, groundwater can be considered the only available source for fresh water. According to EAD reports, the annual abstraction of groundwater from the Remah area is more than 240 million m^3

from more than 6800 operating water wells. Moreover, the low groundwater recharge caused by the low hydraulic conductivity prevented the water table to recover and caused a continuous lowering in the water table. The above-mentioned explanations support the hypothesis that the observed land surface subsidence in the Remah area during the studied period can be attributed to the water level lowering.

Another important finding was the correspondence of the spatial distribution between the detected land subsidence bowl and the depression cone presented in the contour lines of the piezometric water level in 2019. A comparison between the water level drawdown at the GWP-060 monitoring well with the land surface subsidence at the PSs around the same monitoring well showed a continuous decline in both values during the whole studied period (Figure 4.10).

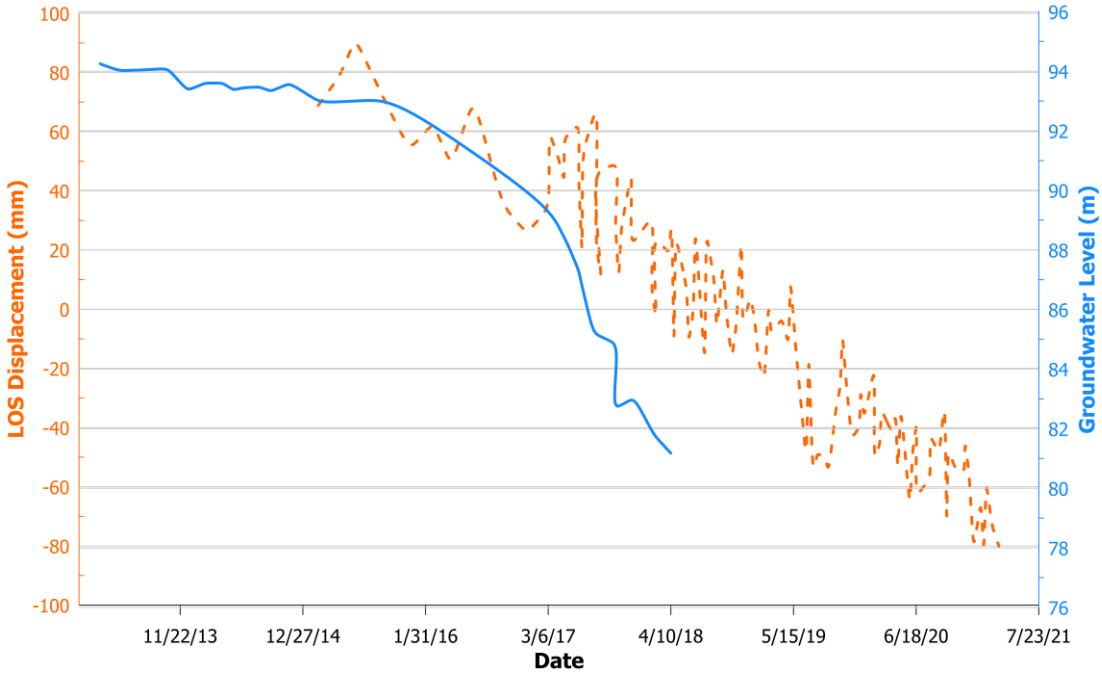

Figure 4.10: The correlation between water level drawdown and land surface displacement shown as blue line and dashed orange line, respectively, at GWP-060 monitoring water well.

Water level changes between 2013 and 2019 have been studied to assess the temporal behavior of the water table in order to investigate if there is any change to the depression cone with time. This investigation showed that the groundwater extraction is growing towards the west of the study area in the above-mentioned period due to the increase of the farming activities in that direction. Therefore, the depression cone is extending in areas with lower deformation rates and specifically in areas that are expected to deform more rapidly in the future if the depression continues extending. Due to the unavailability of any alternative sources for fresh water the land deformations are expected to extend.

4.6 Land Subsidence over Al Wagan

A similar phenomenon has been observed over the Al Wagan area south of the Al Ain city as shown in Figure 3.5. This area includes Bu Kirayyah, Al Araad, Al Wagan, and Al Quaa. This area, also, is characterized by numerous farming activities with 1660 farms and 1604 active farms. These farms are known for planting fruits such as bananas, cider, orange, and others. Also, there are windbreaks composed of forest cover with an area of 0.2 km^2. Similar to the Remah area, the agricultural activities are supported by an extensive network of water wells discharging the underground water with an annual water abstraction of 350 million cubic meters (EAD, 2018).

The implemented processing for the Remah area has been repeated for the Al Wagan area using the same SAR dataset. The Remah and Al Wagan areas are located within the same Sentinel-1 frame but in different sub-swath where the former is located in IW2 and the latter is located in IW3 sub-swath. Moreover, a field survey was conducted to observe land surface deformations signs on February 1, 2020. Unfortunately, there is no available water level data in the Al Wagan area which makes the correlation with land surface deformations is not possible at the moment. The field observations over the Al Wagan showed similar evidence for land surface subsidence to those shown for the Remah area (Figure 4.11). The observed differential settlements of the construction's foundations and inclined electrical pillars are shown in Figure 4.11 (ii) and (iii), respectively.

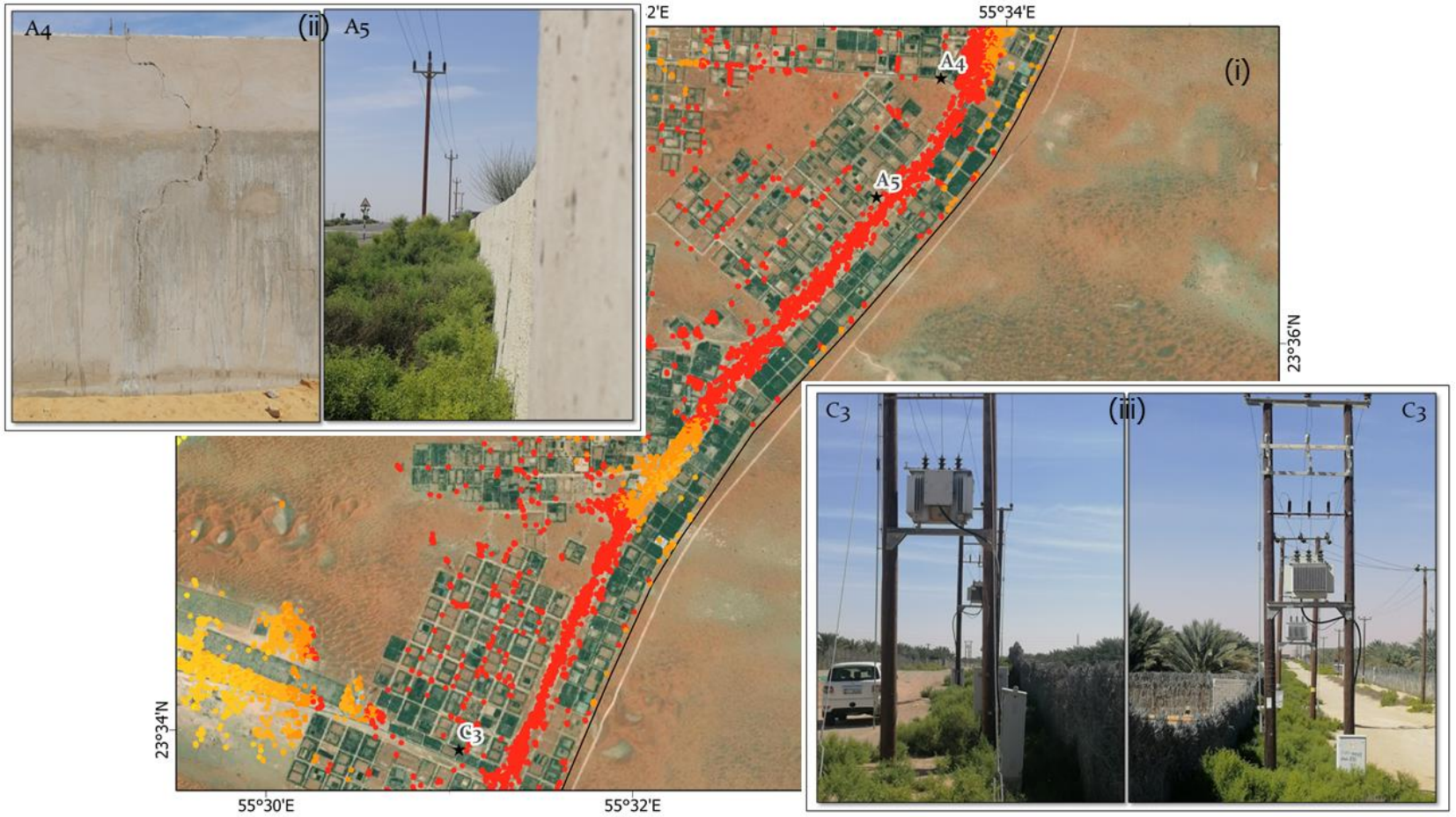

Figure 4.11: Field Observations over Al Wagan area. (i) Locations of land surface subsidence signs over the Al Wagan area. (ii) Differential settlements. (iii) Inclined electrical pillars.

The InSAR processing observed land surface deformations in the range of +5 to -55 mm/year in the same period (Figure 4.12). The maximum deformations rate at the southern area of the Al Ain region was observed in the Al Wagan with -55 mm/year and a lower deformations rate was observed over the Al Araad with -30 mm/year. Also, deformations with -10 mm/year have been observed over the Bu Kirayyah area. The observed land surface subsidence over the Al Wagan area is extending from it is central to the south by 25 km and decreasing gradually before Al Quaa.

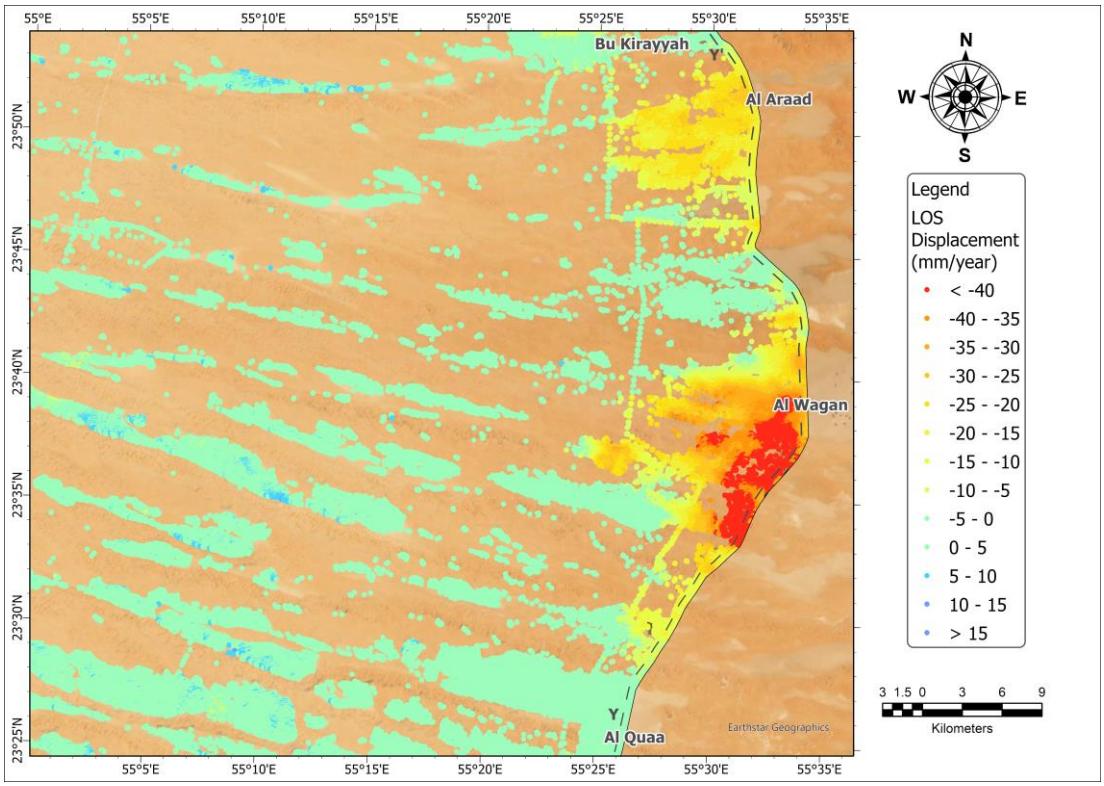

Figure 4.12: Land surface subsidence in LOS direction over Al Wagan between 2015 and 2021 measured in mm/year. The red color represents a higher subsidence rate.

A cross-section of the observed land subsidence was drawn along the Y-Y' line shown as a grey dashed line in Figure 4.12. The cross-section was drawn from the south at the Al Quaa (Y) to the north at the Bu Kirayyah (Y') (Figure 4.13). The cross-section showed a steep land surface subsidence south of the Al Wagan where land

subsidence changed from -14 to -58 mm in a distance of 1.8 km, while more gradual land subsidence was observed north of the Al Wagan where land subsidence changed from -51 to -3 mm in a distance of 9.5 km. The detected land surface subsidence over the Al Araad was gradual which changed from -6 to -31 mm in a distance of 7.6 km and increased again toward the Bu Kirayyah to -0.5 mm in a distance of 4.6 km.

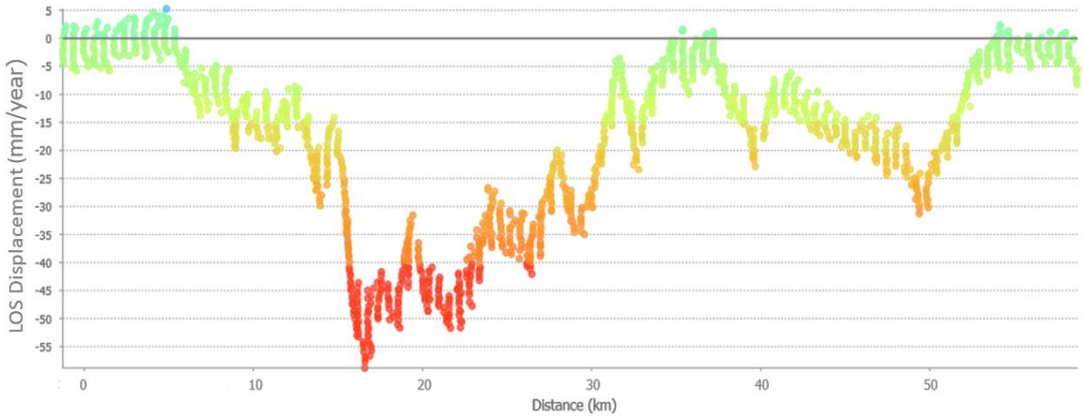

Figure 4.13: Cross-section along Y-Y' shown as a dotted grey line in Figure 4.12.

The uncertainty of this processing was checked by calculating the standard deviation for the detected land surface displacements as conducted for the Remah area. The standard deviation values over the Al Wagan area were within the same range as for the Remah area, within 2 mm/year as shown in Figure 4.14.

The history of the land surface subsidence over the Al Wagan area has been investigated by Liosis et al. (2018) who studied the phenomena in two periods, the first from 2003 to 2010, and the second from 2016 to 2018. For the first period, Liosis et al. (2018) reported that a land surface subsidence rate of -18 cm/year was observed using two SAR datasets, C-band ENVISAT and L-band ALOS-1, with the SBAS technique. This showed a high correlation coefficient, more than 0.9, between the water level drawdown and the land surface subsidence. For the second period, the

Sentinel-1 SAR dataset was implemented with the SBAS technique and detected a land surface subsidence with a rate of -10 cm/year. Noteworthy, the study concluded that the Sentinel-1 results were unreliable due to the small available dataset at the time and the lack of an appropriate method for atmospheric correction.

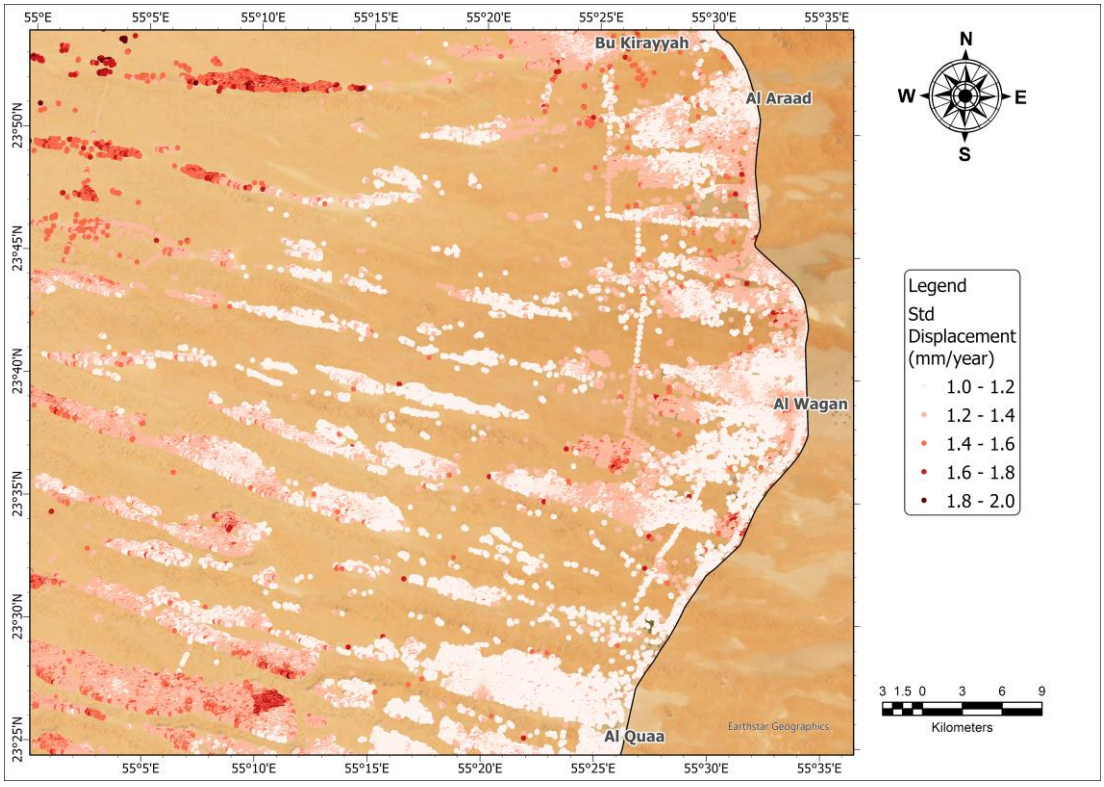

Figure 4.14: Subsidence rate standard deviation for velocity values shown in Figure 4.12.

The investigation of the land surface subsidence over the Al Wagan area using 97 Sentinel-1 images with the StaMPS technique showed a continuity for the land surface subsidence detected in the previous study but with a slower subsidence rate which can be caused by sustainable practices for groundwater resources management controlled by the Environment Agency of Abu Dhabi.

Chapter 5: Integration of InSAR with Geophysical Technique

5.1 Introduction

Land surface monitoring practices include various techniques and choosing the appropriate technique depends mainly on the physiography of the study area and the monitoring purposes. Remote sensing data provides information related to the Earth's surface with small and less certain about the subsurface. While geophysical techniques provide information related to the subsurface strata from shallow to deep depth. The big limitation for the geophysics technique is point data information which collected this type of information everywhere is not feasible. On the other hand, remote sensing data provides wide coverage with continuous recording over the Earth's surface.

The integration between remote sensing and geophysics techniques can fill the space gap and provide new insight on monitoring the land surface. In this chapter, an integration between the InSAR remote sensing and microgravity geophysical techniques is implemented and discussed over the Al Ain city, Abu Dhabi Emirate.

Integration of these two techniques can unveil unknown behaviors for land surface deformations and underground fluid movement (oil, gas, or water). Also, the effect of precipitation on the underground mechanism and density distribution can be seen from this integration. Furthermore, a better understanding of the relationship between microgravity measurements and land surface deformations can be achieved.

5.2 Geomorphology & Geology of Al Ain Area

Al-Ain area is located in the eastern part of the Abu Dhabi emirate on the UAE-Oman border (Figure 5.1). Its elevation varies from more than 300 m in the east

to about 200 m in the west. The area is characterized geomorphologically by three main features: mountains, gravel plains, and sand dunes. The mountains are represented by Jabal Hafit and Oman Mountains located southeast and east of the Al Ain city, respectively. Jabal Hafit extends northwest-southeast is 29 km long, 5 km wide, and with an elevation of 1240 m a.s.l. The gravel plains occupy the western side of the Oman Mountains and consist of alluvial fans formed by transported sand and gravel through wadis from Oman Mountains. The sand dunes cover almost 76% of the UAE and this feature occupies the western part of the Al Ain area. The sand dunes can be divided according to the pattern into dune ridges, low dunes, and star dunes.

Figure 5.1: Location of Al Ain city within the UAE.

The geology of the study area can be divided into six main units (Figure 5.2): Rus Formation, Dammam Formation, Asmari Formation, Lower Fars Formation, Barzaman Formation, and Quaternary Deposits. The Rus Formation, from the Early Eocene epoch, is exposed on the top of Jabal Hafit at the core of the anticline fold. It consists mainly of limestone with two units, the lower is generally pale grey nummulitic massive limestone with clasts of coral and gastropods, while the upper is thinly bedded pale yellow lime mudstone with chert nodules (Ministry of Energy, 2006). This formation also is characterized by a dolomitization process that occurred in the upper part and appears as pale-brown weathering (Saibi, Amrouche, and Fowler, 2019).

The Dammam Formation, with a maximum thickness of 600 m, overlies the Rus Formation and is exposed in the northern part of Jabal Hafit. This formation is dominated by limestone and lime mudstone. The base part consists of creamy grey, thickly bedded lime mudstone with marl fillings between the beds. The main unit in this formation is composed of grey, poorly bedded pseudonodular nummulitic limestone with corals (Ministry of Energy, 2006). In the eastern limb of Hafit anticline, two more units are exposed that are believed to belong to the Dammam Formation; they are a greenish-brown lime mudstone and a pale brown nummulitic limestone.

The Dammam Formation is unconformably overlain by the Asmari Formation of the Early Oligocene age. El Tokhi et al. (2012) divided this formation into three units: the base consists of greenish-grey bedded mudstone with marl formed between the beds, while the middle unit consists of poorly bedded to massive dolomitic and chalky limestone rich in fossils, and the top consists of massive chalky limestone which contains huge amounts of coral heads and nummulites.

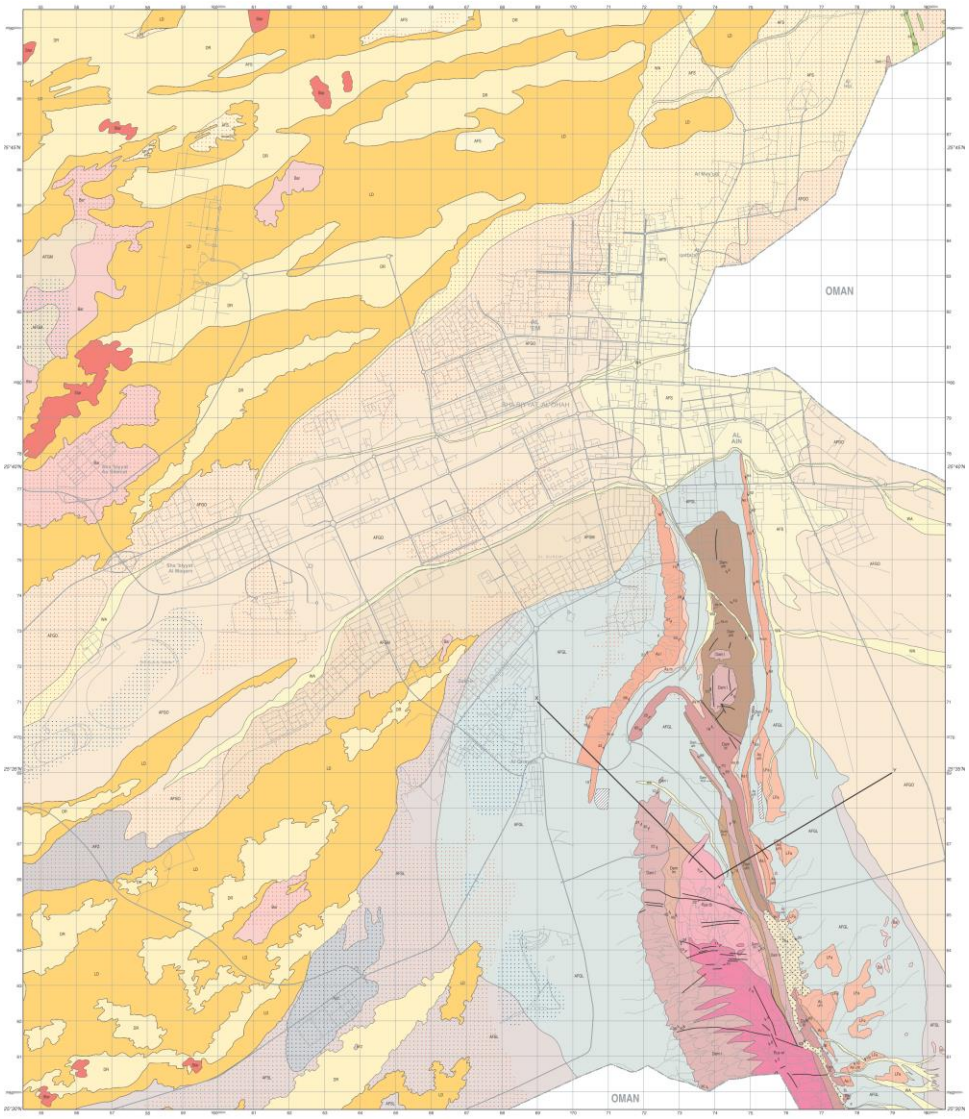

	Worked Ground		Sand Veneer
	Scree and Rockfall	Bar	Barzaman Formation
	Sabkha (Dry)	LFa	Lower Fars Formation
WA	Wadi Alluvium	As um	Asmari Formation, upper mudstone
AFGM	Alluvial Fan Gravel, Mixed	As l	Asmari Formation, limestone
AFGL	Alluvial Fan Gravel, Limestone	As m	Asmari Formation, mudstone
AFGO	Alluvial Fan Gravel, Ophiolite	Dam bl	Dammam Formation, brown limestone
AFS	Alluvial Fan Sand	Dam um	Dammam Formation, upper mudstone
AFSL	Alluvial Fan Sand, Limestone	Dam l	Dammam Formation, limestone
AFZ	Alluvial Fan Silt	Dam m+l	Dammam Formation, mudstone and limestone
DR	Dune Ridge	Dam lm	Dammam Formation, lower mudstone
LD	Low Dunes	Rus tb	Rus Formation, thin bedded unit
Star	Star Dune	Rus wl	Rus Formation, white limestone
	Sand Veneer	Sim	Simsima Formation

Figure 5.2: Geological map of Al Ain area (Ministry of Energy, 2006)

The Lower Fars Formation, from the Early Miocene epoch, is conformably overlays the Asmari Formation and is well exposed 1 km east of Jabal Hafit with a small outcrop west of Jabal Hafit. The thickness of this formation is estimated at 330 m (Ministry of Energy, 2006) and it consists of creamy brown celestite, lime mudstone with gypsum veins, lithic sandstones, and pebble conglomerates with clasts of quartz, chert, and the Oman-UAE ophiolite (Saibi et al., 2019).

The overlying formation is the Barzaman Formation from the Middle Miocene to Pliocene epoch and it crops out east of Jabal Hafit in the interdune areas, beneath Al Jaww plain, and Quaternary deposits. The base of the formation is composed of gabbro and harzburgite conglomerates. At the west, where it mostly underlies sand dunes, it consists of an interbedded sequence of mudstones, sandstones, and conglomerates (EAD, 2018). The mudstones are blocky, pale white with iron and manganese. The conglomerates are massive poorly sorted, poorly bedded with clasts composed of gabbro, harzburgite, limestone, and chert. Sandstones are soft, variegated, cross-bedded, and finning upwards (Ministry of Energy, 2006).

Quaternary deposits cover more than 76% of the UAE. Quaternary deposits in the Al Ain are can be divided into aeolian deposits, alluvial fan deposits, wadi deposits, and inland sabkha deposits. Aeolian deposits cover most of the northwestern part and southwestern part of the Al Ain area. The aeolian deposits can be divided into dune ridges, low dunes, star dunes, and sand veneers. The aeolian sand consists of moderately to well-sorted fine sand with sub-rounded quartz grains (El-Sayed, 1999). The aeolian deposits vary in color depending on their location. Near the Hajar mountains, the aeolian deposits appear darker, a pale to burnt orange, due to the increase of dark Fe-Mg rich lithics. While around Jabal Hafit the aeolian deposits tend

to appear lighter, pale orange to cream, due to the increase of carbonate grains from the erosion of limestone alluvial from Jabal Hafit.

The alluvial fan deposits occupy most of the east part of the Al Ain area with some coverage in central areas. The alluvial fan deposits vary with the distance from the mountains and in the Al Ain area, the units vary between differentiated gravels, sand, and silt while wadi alluvium consists of unconsolidated very poorly sorted fluvial sand and gravel deposits. This unit also contains clasts of ophiolite, limestone, or mixed lithology depending on the source area (Ministry of Energy, 2006).

The hydrogeology of the UAE consists of four main aquifers as shown in Figure 5.3: limestone aquifers, ophiolite aquifers, gravel aquifers, and sand dune aquifers (Elmahdy and Mohamed, 2015). Limestone aquifers are located in the north at Jabal Jais and in the east at Jabal Hafit. The ophiolite aquifer is located at the east, and the gravel aquifers can be divided into the east aquifer (east of the ophiolite) and the west aquifer (west of the ophiolite). The sand dune aquifer is located in the south and west (Rizk and Alsharhan, 2003). The Al Ain area is located within the western gravel aquifer which comprises a sequence of alluvial deposits of the piedmont plains (Murad, Nuaimi, and Hammadi, 2007).

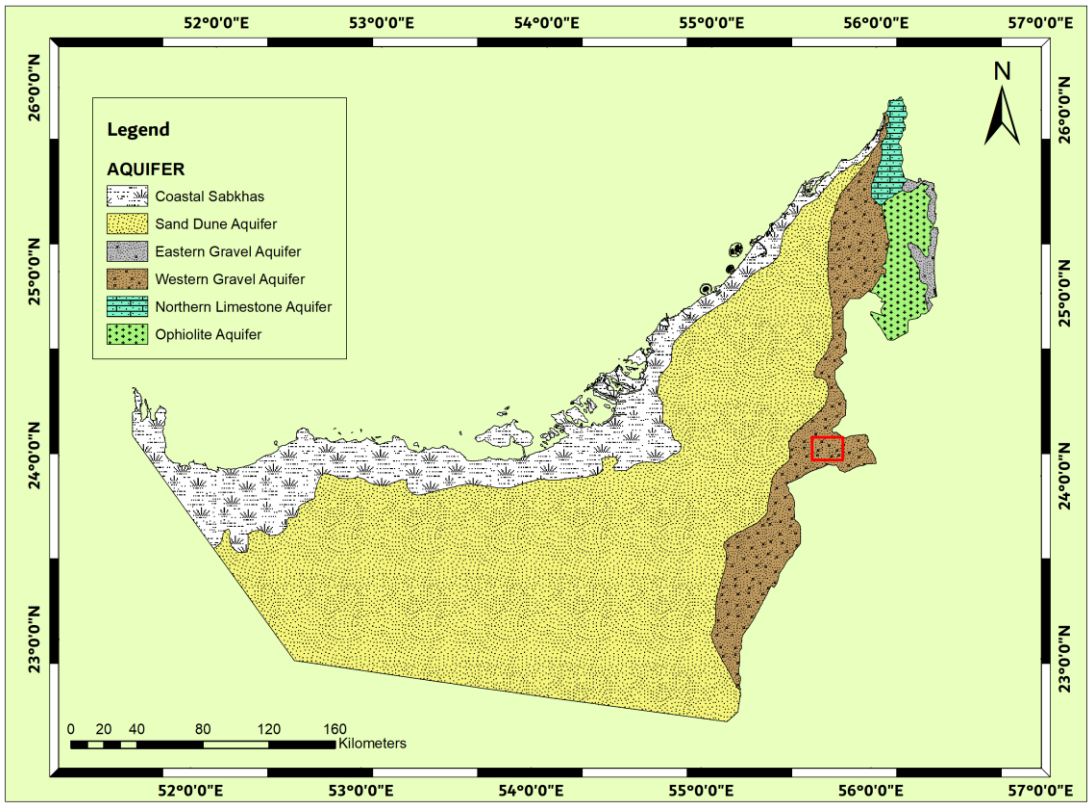

Figure 5.3: The main groups of groundwater aquifers in the UAE. The red rectangle shows the position of the study area located over the Western Gravel Aquifer.

The western gravel aquifer consists, at the top section, of sand and gravel with thin silt and clay interbedding with thickness ranging from 30 to 60 m. Whereas, alluvium deposits from Oman-UAE ophiolite occupy the bottom section. The western gravel aquifer in the Al Ain area is underlain by the Lower Fars Formation at the east (Al Jaww Plain) and by tectonically thrusted marls and shales (EAD, 2018). Hydraulic conductivity in the Al Ain region ranges between 1 and 10 m/day with an average of 4 m/day.

The recharge of the aquifer is due to rainfall from the Northern Oman Mountains. The recharge mechanism begins with infiltration of rainfall and surface flow along Wadis that drain the Oman Mountains, then subsurface flows from lateral flow in alluvial channels at the mouths of the drainage basins along the mountain front,

and finally lateral flow through fractured bedrock along the mountain front. Three main types of groundwater flow systems generated from these mechanisms include local flow, intermediate flow, and regional flow. Also, the whole groundwater flow system drains from mountains at the east through the plains towards the coast at the west (Mohamed, 2014). Al-Ain area is within the local groundwater flow system where the hydrologic cycle is fast and the groundwater has a short residence time (Rizk and Alsharhan, 2003).

5.3 Gravity Method

The gravity geophysical method is a non-destructive geophysical method that measures variations in the Earth's field of gravity between two locations. The field of gravity variations depends primarily on the density variations of the subsurface materials from one location to another. The gravity geophysical method is based on the Universal Law of Gravitation and the Law of Motion. The acceleration due to the gravity unit is 1 cm/s^2 also known as Gal, named after Galileo, and the gravitational acceleration value at the Earth's surface is almost 980 cm/s^2, or 980 Gal. But this value varies slightly between locations due to the Earth's shape.

It is believed that the Earth's shape is a flattened sphere, ellipsoid, with the major axis towards the equator and the minor axis towards the poles from the Earth's center. This means that the points at the poles are closer to the Earth's center of mass than the points at the equator, therefore, theoretically, the gravity is greatest at the poles and decreases toward the equator. This decreasing is occurred due to the centrifugal acceleration resulting from the Earth's rotation around its north-south axis.

The density of the subsurface rocks plays a pivotal role in the resultant gravity at a specific location. Rock densities vary depending generally on the material made and the degree of consolidation, this means that sedimentary rocks have a lower density than igneous and metamorphic rocks. The density of the sedimentary rocks can be affected by their composition, cementation, depth, tectonic process, porosity, and pore-fluid type. While for the igneous rocks the silica content controls the density variations, where the density increases with the silica content decreases. This means that basic igneous rocks have a higher density than acidic ones (Gabbro is denser than Granite), and intrusive igneous rocks have a higher density than their volcanic equivalents (Gabbro is denser than Basalt). The density variations between metamorphic rocks appear chaotic with a general trend to increase with increasing grade of metamorphism.

There are two types of gravity measurements, absolute gravity measurements which is the measurement of the entire gravity field at a specific location, and relative gravity measurements which is the measurement of gravity differences between two locations. Therefore, there are two types of gravity meter, also known as the gravimeter, absolute gravity meter and relative gravity meter. Absolute gravity measurement requires specific experiment processes and uses either falling body or swinging pendulum methods. While relative gravity measurement conducts over a network of gravity stations and all gravity data measured during the survey is relative to a specific location called the base station. Relative gravimeter is spring-based where a specified mass hangs over a very sensitive spring that stretches relatively to the mass gravitational acceleration. Gravimeter measures a meter reading that is multiplied by an instrumental calibration factor to produce an observed gravity value. Gravity data

measurements need to be corrected before they can be interpreted or integrated with other measurements.

The corrections to gravity measurements include instrumental drift, tide, latitude, free-air, Bouguer, and terrain corrections. The first two corrections are varied with time while the other corrections are varied with location. The instrumental drift occurred due to the elastic creep of the spring which changes the gravimeter readings with time. The instrumental drift is determined by measuring the gravity at the same station repeatedly at various times during the day. Tides' effect on gravimeter measurements can be large enough to produce a significant change in 12 hours. The tide effect can be corrected by repeated measurements at the same station similar to the instrumental drift correction.

The latitude correction is performed to compensate for the gravity field increases away from the equator and closer to the poles. The latitude correction is conducted by subtracting the theoretical gravity calculated via the International Gravity Formula (Equation 5.1) from the measured gravity.

$$g_{\varphi} = g_0(1 + \alpha \sin^2 \varphi - \beta \sin^2 2\varphi) \tag{5.1}$$

where g_{φ} is the theoretical gravity at φ latitude, g_0 is the gravity field at the equator, and α, β are parameters related to the flattening model approximation of the Earth. The latitude correction is negative towards poles and positive towards the equator.

The free-air correction (ΔG_F) is the difference between the gravity field measured at the sea level and the gravity field measured at h elevation without rocks in the distance between the sea level and h. This correction is performed by using a

gradient of 308.6 µGal/m where it is positive for locations above the sea level and negative for locations below the sea level. The free-air gravity gradient is increasing marginally from the equator to the poles by 0.5 µGal/m. Noteworthy that the elevation precision should be around 1-2 cm.

The Bouguer correction (ΔG_B) is the compensation for the extra gravitational field resulting from the rock mass (ρ) between the gravity station elevation (h) and the sea level (Equation 5.2). The Bouguer correction factor is subtracted from the observed gravity for stations located above sea level.

$$\Delta G_B = 2\pi G \rho h \tag{5.2}$$

where G is the gravitational constant.

The two latter corrections are related to elevation of the gravity station measurement and usually, these two corrections are processed in one equation, as shown in Equation 5.3, to avoid misinterpretation

$$\Delta G_E = \Delta G_F - \Delta G_B = (3.086 - 0.4192\rho)h \tag{5.3}$$

To be able to compare the gravity field measurements between gravity stations these measurements should be referred to the same base station. This value is called the Bouguer Anomaly which is the difference between the corrected measured gravity at each station and the gravity measured at the base station.

5.3.1 Gravity Survey

Gravity geophysical survey visits have been conducted over Al Ain city in the period between March 2019 and March 2020. The purpose of the gravity survey was

to monitor land surface deformations and groundwater dynamics around monitoring water wells. The performed gravity geophysical technique for the monitoring purpose was the Time-lapse Microgravity (TLMG) technique, also known as 4D microgravity which measures gravity in micro values and the fourth dimension is time. TLMG is performed by repeated gravity measurements over the same gravity stations for some time (Kadir, Santoso, and Alawiyah, 2007). Gravity signals that can be attributed to the land surface deformations and groundwater dynamics are very small, therefore, the TLMG requires a specific instrument that has a resolution of micro-measurement. The gravimeter used for the gravity survey was the Scintrex CG-6 Autograv (Figure 5.4), which it is characteristics are listed in Table 5.1.

Figure 5.4: Scintrex CG-6 Autograv

The Scintrex CG-6 Autograv is characterized by 1 µGal resolution and less than 5 µGal standard deviations. This instrument is portable according to its dimension, 21.5 x 21x 24 cm, and lightweight of 5.2 kilograms. Moreover, some gravity corrections are incorporated automatically, including tide, instrument tilt, temperature, and drift corrections (Scintrex, 2018).

Table 5.1: Scintrex CG-6 Autograv specifications

Dimension	21.5 cm(H) x21 cm x 24 cm
Weight	5.2 Kg (11.5 lbs) including batteries
Reading Resolution	1 microGal
Standard Deviation	<5 microGal
Automated Corrections	Tide, instrument tilt, temperature, noisy sample filter, seismic noise filter, drift
Touch-free operation	Handheld Tablet with Bluetooth
Battery Capacity	2 X 6.8 Ah (10.8 V) rechargeable lithium smart batteries. Full day operation at 25°C (77°F)
Data Output	USB and Bluetooth

The gravity field measurements have been taken from 10 locations distributed over Al Ain city in order to unveil the fluctuations of the land surface and groundwater level during one year. The measurements that have been taken of each station along with the gravimeter reading were the position (longitude and latitude) and instrument height above the Earth's surface (in millimeter accuracy). The gravity survey has been designed to start from the base station, where it is located at the United Arab Emirates University in building E4 as labeled with a red star shown in Figure 5.5 and end at the base station.

Figure 5.5: Locations of the gravity monitoring sites over Al Ain city.

The gravity survey began with measuring gravity at the base station then visited the first gravity station and took a gravity field measurement. At every gravity station, the gravity measurements have been taken in a two-way measurements protocol, where the gravity field was measured in the go direction and the back direction as shown in Figure 5.6. The two-way measurement protocol has been performed to reduce the reading error (Saibi, 2017). For each measurement, the gravimeter was placed over a tripod in a consistent direction to avoid any error related to the instrument azimuth. Then the tripod was balanced horizontally for the measurement and the height of the gravimeter above the ground was taken. After that, the gravimeter was started the gravity field reading and for each measurement, an average of 120 readings was taken over two minutes with one reading every second. After measurements have been taken over the ten specified gravity stations a final gravity field measurement has been taken

at the base station to close the loop. Noteworthy that each loop has been completed in less than 4 hours and before midday to reduce the spring creep sensitivity to the change in temperature. The gravity survey has been conducted in 11 loops, or visits, in the period between March 2019 and March 2020 and the gravity stations have been visited in the same order for the eleven loops to keep the consistency.

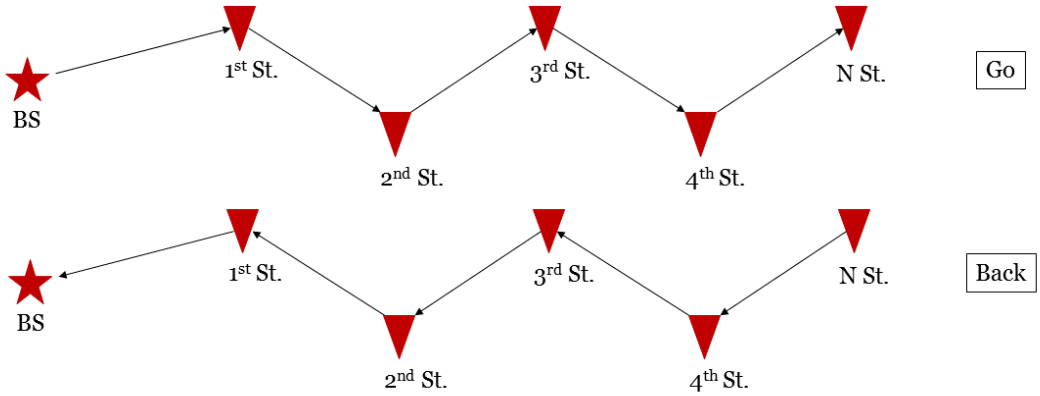

Figure 5.6: Go & Back measurement protocol.

5.3.2 Gravity Data Processing

After each gravity survey, the measured values have been stored in a separate table for further data processing. Each table contains corrected gravity measurements (go and back), latitude, longitude, and instrument height for each gravity station. As above mentioned in the gravity survey section each gravity survey started and ended at the base station, so all gravity measurements should be referred to the base station. This has been achieved by subtracting the measured corrected gravity at each gravity station ($g_{x,t}$) from the measured corrected gravity at the base station ($g_{BS,t}$) within the same gravity survey (Equation 5.4). This process has been applied for each gravity

survey dataset and named the corrected gravity at time t ($\Delta g_{x,t}$), which is the time when the gravity survey has been conducted.

$$\Delta g_{x,t} = g_{x,t} - g_{BS,t} \quad (5.4)$$

The first gravity survey has been conducted in March 2019 and the dataset of this survey has been considered the baseline for the TLMG analysis. Therefore, the corrected gravity at the first survey is the corrected gravity at the baseline. TLMG anomalies have been generated by subtracting the corrected gravity at each gravity survey ($\Delta g_{x,t}$) from the corrected gravity at the baseline ($\Delta g_{x,t_0}$) (Equation 5.5The subtraction process has been performed between the correspondence gravity station (e.g., the corrected gravity at station A in time t has been subtracted from the corrected gravity at station A in time t_0).

$$\Delta g_{x,\Delta t} = \Delta g_{x,t} - \Delta g_{x,t_0} \quad (5.5)$$

The TLMG anomalies ($\Delta g_{x,\Delta t}$) have been generated to monitor the gravity signals due to land surface deformations and groundwater dynamics.

In order to reveal the spatial and temporal variation of gravity, TLMG anomalies have been interpolated using the Kriging interpolation technique to generate ten surfaces for all gravity survey measurements. Also, temporal gravity changes for each gravity site have been plotted on a linear graph to facilitate the interpretation process.

5.4 InSAR Dataset & Processing

In order to utilize InSAR processing, a stack of Sentinel-1 images provided by the ESA has been captured from the Alaska Satellite Facility (https://search.asf.alaska.edu). Thirty Sentinel-1 scenes over Al Ain city in the same

period as the gravity survey have been acquired. Sentinel-1 is characterized by a temporal resolution and wavelength of 12 days and 5.6 cm (C-band), respectively. Moreover, Sentinel-1 images were acquired with high image quality and wide swath due to the imaging mode of Interferometric Wide swath mode (IW) (Torres et al., 2012). The Sentinel-1 images were co-registered to a single master image acquired on the 18th of November 2019. This image was selected as a master image because it is the shortest perpendicular and temporal baselines.

The pre-processing steps have been performed by utilizing the open software SeNtinel Application Platform (SNAP) which includes applying orbit information, co-registration, interferogram generation, and spatial subset. The interferometry analysis was performed using the StaMPS MT-InSAR software package, so the final step of the pre-processing was to export the interferograms to StaMPS (Figure 5.7). The pre-processing steps have been iterated automatically using a combination of python scripts and XML files to facilitate the pre-processing. Ancillary data used in the co-registration process includes DEM and orbit data. For DEM data, 1 arc-second SRTM data was used while precise orbit data have been accessed via SNAP software.

The PSs have been initially selected with the method of amplitude dispersion proposed by (Ferretti et al., 2001). A threshold of 0.4 was chosen to select the PS candidates; any pixel with an amplitude dispersion value less than the threshold was not be considered as a PS candidate. The topographic error was modeled at a threshold of 5 m with a maximum spatial density of 20 PSs/km2 from random phase pixels to reduce the uncertainty of the PSs. In order to maintain a low signal decorrelation in the PS candidates, the interferometric phase noise standard deviation for all pairs was limited to a threshold of 1.0. Then, the topographic phase was estimated from the

SRTM data and removed from the interferograms to generate the differential interferograms. The remaining interferometric phase was unwrapped using Statistical-Cost Network-Flow Algorithm for Phase Unwrapping (SNAPHU). The phase unwrapping process is the most complicated in InSAR processing as it attempts to solve the integer number of the wave cycles between the sensor and each pixel. Then, the phase component of the signal delayed in the atmosphere was corrected by performing the open-source TRAIN (Bekaert et al., 2015).

The InSAR processing resulted in a set of PS pixels with an estimated surface displacement time-series after removing flat-Earth, elevation, and atmospheric components. The estimated displacement is the LOS velocity for each PS and it is expressed in mm/year.

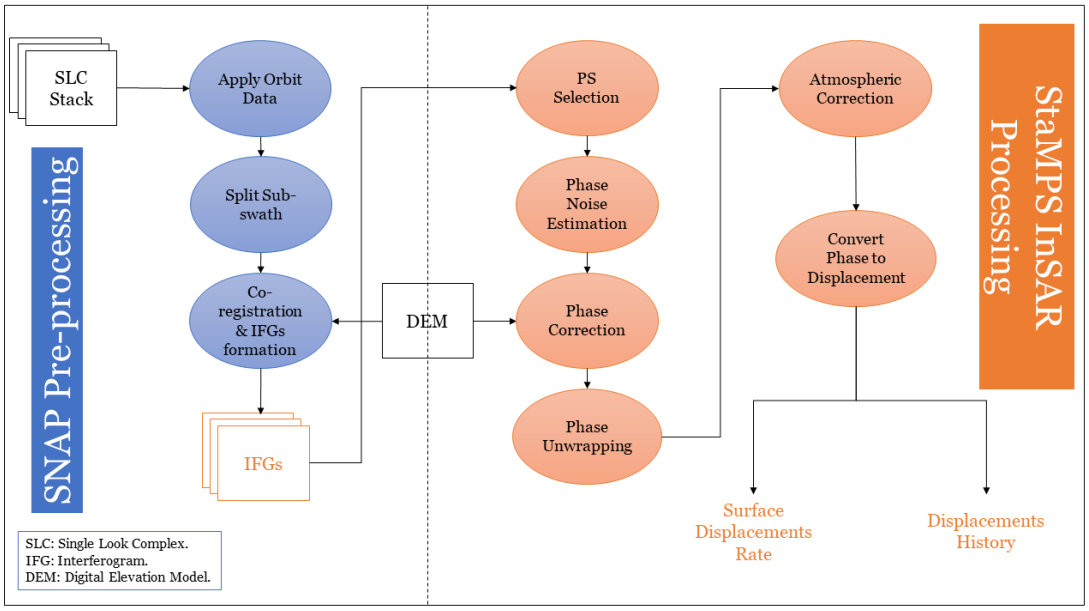

Figure 5.7: Flowchart for the InSAR processing steps of SNAP and StaMPS.

5.5 Results

The computed TLMG anomalies revealed significant fluctuations in space and time as shown in Figure 5.8. The TLMG anomalies varied temporally in a periodic shape where the anomaly was at its minimum during summer, dry season, from May through August then it was increased in September and October to reach its maximum in November. After that, the TLMG anomalies were decreased slowly from December through March. On the other hand, the TLMG anomalies were distributed spatially with the higher anomalies located at the eastern part (stations B, C, D, E, and F) and the lower anomalies located at the southern part (station G) of the study area. The minimum TLMG anomaly has been recorded at a station (G) in June 2019 with -36 μGal while the maximum TLMG anomaly has been recorded at a station (H) in November 2019 with 365 μGal.

Minimum and maximum values of the TLMG anomaly for each gravity survey have been listed in Table 5.2. The second and third gravity surveys contain the shortest and longest range, respectively, among all gravity surveys. Both gravity surveys were recorded the only negative TLMG anomalies for the entire period with -36 and -21 at stations (G) and (I) in June and August, respectively.

Moreover, minimum and maximum TLMG anomalies for each gravity station have been listed in Table 5.3. It has been noticed that all the maximum values listed in Table 5.3 were measured in November 2019 while the minimum values were measured in June 2019 except for station (I) whose minimum was measured in August 2019.

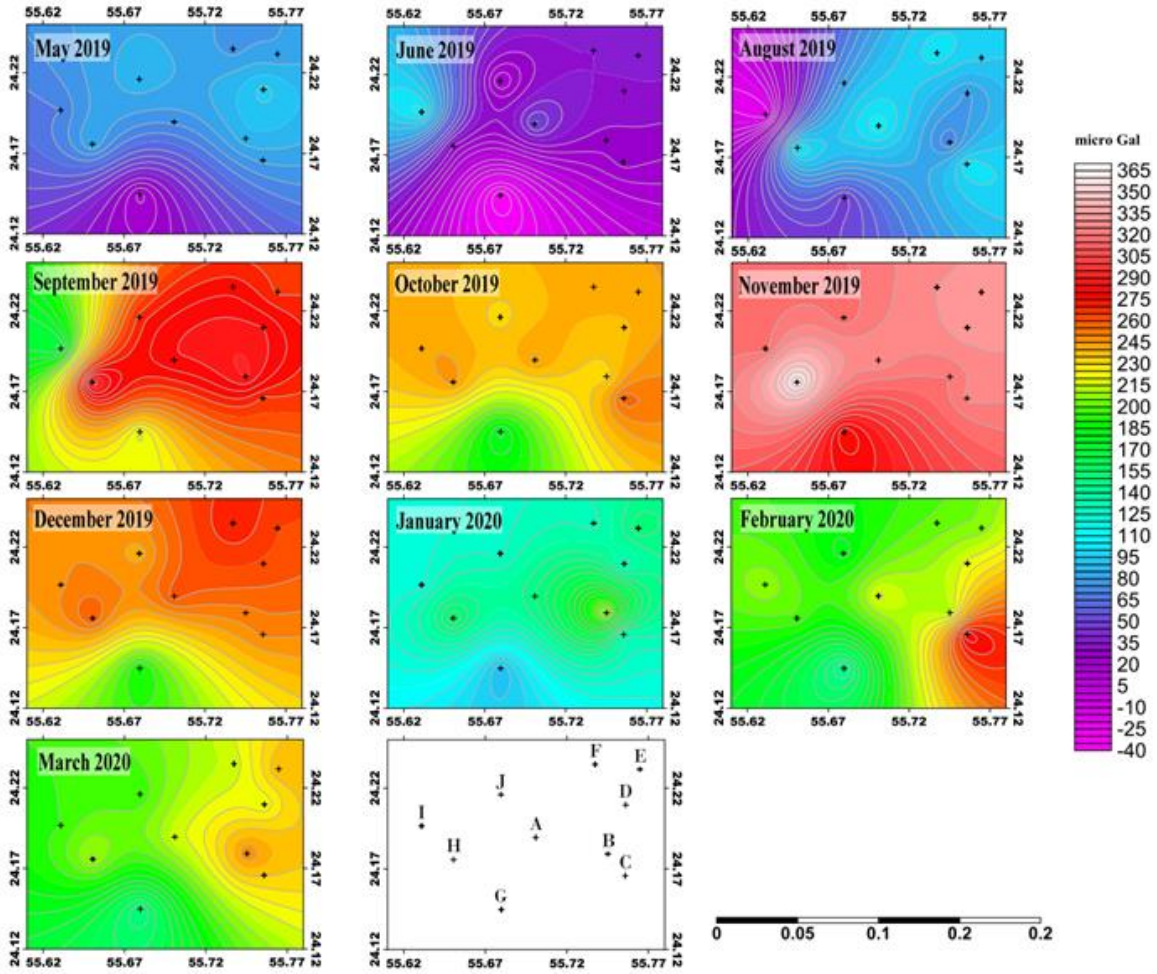

Figure 5.8: Time-lapse microgravity anomalies over Al Ain city measured with March 2019 as a reference time. July data were not gathered.

The groundwater level in Al Ain city shows a trend of the shallower water table in the east than in the west of the city as reported by the Environment Agency of Abu Dhabi (EAD, 2018). TLMG anomalies are controlled by many factors such as the general elevation of the area under investigation and the depth to the water table. Shallow water table zones reflect higher TLMG anomalies than deeper water table zones. The computed TLMG anomalies followed this scenario where the high TLMG anomalies are combined with a shallow groundwater table at the eastern part of the city while the low TLMG anomalies are combined with a deep groundwater table at the western part of the city.

Table 5.2: Minimum and maximum TLMG anomalies for each gravity survey.

Measurement	**Minimum (µGal)**	**Maximum (µGal)**
May 2019	17	96
June 2019	-36	108
August 2019	-21	108
September 2019	168	290
October 2019	177	257
November 2019	274	365
December 2019	187	274
January 2020	89	213
February 2020	143	283
March 2020	148	249

There are several sources for the signals that generated the TLMG anomalies, which include surface sources, such as ground elevation change, and subsurface

sources, such as underground fluid movement (e.g., groundwater, oil, gas) or changes in the subsurface physical properties (e.g., density). There is an ambiguity in identifying the source of the TLMG anomalies source, i.e. where the signal is coming from. For example, the TLMG anomaly signal from lowering the ground surface (ground subsidence) is similar to the anomaly signal from increasing the subsurface density, and the TLMG anomaly signal from groundwater level drawdown is similar to the anomaly signal from decreasing the subsurface density (Santoso et al., 2011).

Table 5.3: Minimum and maximum TLMG anomalies for each gravity station.

Station	**Minimum (µGal)**	**Maximum (µGal)**
A	52	328
B	27	319
C	27	325
D	33	332
E	39	330
F	35	329
G	-36	274
H	30	365
I	-21	317
J	14	316

The TLMG anomalies and LOS displacement velocity over Al Ain city showed a land surface subsidence in combination with a high TLMG anomaly at the northeastern part of the city (stations E and F). Also, a land surface uplift was noticed in combination with a low TLMG anomaly at the southern part of the city (station G). However, as above-mentioned these combinations can be more complicated as the high TLMG anomaly at the eastern part can be related to the shallow groundwater.

Statistical correlations between TLMG anomalies and LOS deformations values have been generated in order to better understand the contribution of the land

surface deformations to the observed gravity signal (Table 5.4). The significant negative correlation coefficients were presented in stations (D, E, H, and G), where the first three gravity stations were located at the land surface subsidence zones (northeast and west) and the last one was located at the land surface uplift at the south. This correlation is in good correspondence with the major findings of the SAR interferometry analysis where other locations have detected no significant land surface movement. Note that due to many factors contributing to the TLMG anomalies we did not expect to find high correlation values between TLMG anomalies and LOS deformations.

Table 5.4: Correlation coefficient between LOS displacement and TLMG over the gravity monitoring sites.

Station	Correlation
A	0.15
B	0.25
C	0.12
D	-0.55
E	-0.43
F	-0.2
G	-0.39
H	-0.44
I	0.07
J	-0.31

Al-Ain city is characterized by precipitation events during winter, between October and January. During the investigated period the precipitation started in October 2019 and increased slowly to reach its maximum in January 2020. The TLMG response to the precipitation event can be observed in February 2020 when the TLMG anomalies increased significantly from those in January 2020 in all gravity stations

(Figure 5.9). Therefore, this can be interpreted as increasing in the subsurface density and can lead to rising in the groundwater level. This interpretation can be supported by the increasing values of LOS displacement velocity at eight stations in February 2020 which means this increase in the TLMG anomalies is unattached to land surface subsidence.

Land surface deformations of 1 cm produce a change in the gravity field of 3.4 µGal where for subsidence it is positive and for uplift it is negative. On the other hand, decreasing subsurface density in the amount of 1.94 gr/cc produces a change in the gravity field of -0.79 µGal (Allis and Hunt, 1986). Therefore, the contribution of the land surface deformation is greater than that for the change in the subsurface density. The land surface subsidence zone is located close to Al Ain Oasis where a huge amount of groundwater is extracted for irrigation purposes via falajs and boreholes. Therefore, groundwater overexploitation can be considered as the driving mechanism for land surface subsidence, and due to a contribution from both sources, groundwater table drawdown and land surface subsidence, with the above-mentioned explanation, the TLMG anomalies include a signal of land surface subsidence with an opposite signal from subsurface density increase of return irrigation. The signal separation of all these contributions is a big challenge for TLMG anomaly interpretation and yet all proposed approaches are not reliable or contain a high level of uncertainty.

Land surface deformations showed land subsidence (negative measurements) at the western part of the study area, while the TLMG anomalies showed low values at the same zone. This zone is a typical example of the ambiguity presented with TLMG anomalies interpretation where the gravity signal was not followed by the land surface deformations. The Environment Agency of Abu Dhabi reported there was a

water level drawdown by 3 m at the same zone during the investigated period. Hence, the contribution of the groundwater level on the TLMG signal was greater than the contribution of the land surface deformations at this zone. Same TLMG anomalies signals have been observed at the central part of the study area with no significant signal for land surface deformations. These observations have been noticed during summer, therefore, can be interpreted also as groundwater level drawdown, it is noteworthy that there were no available groundwater level measurements at the central part of the study area.

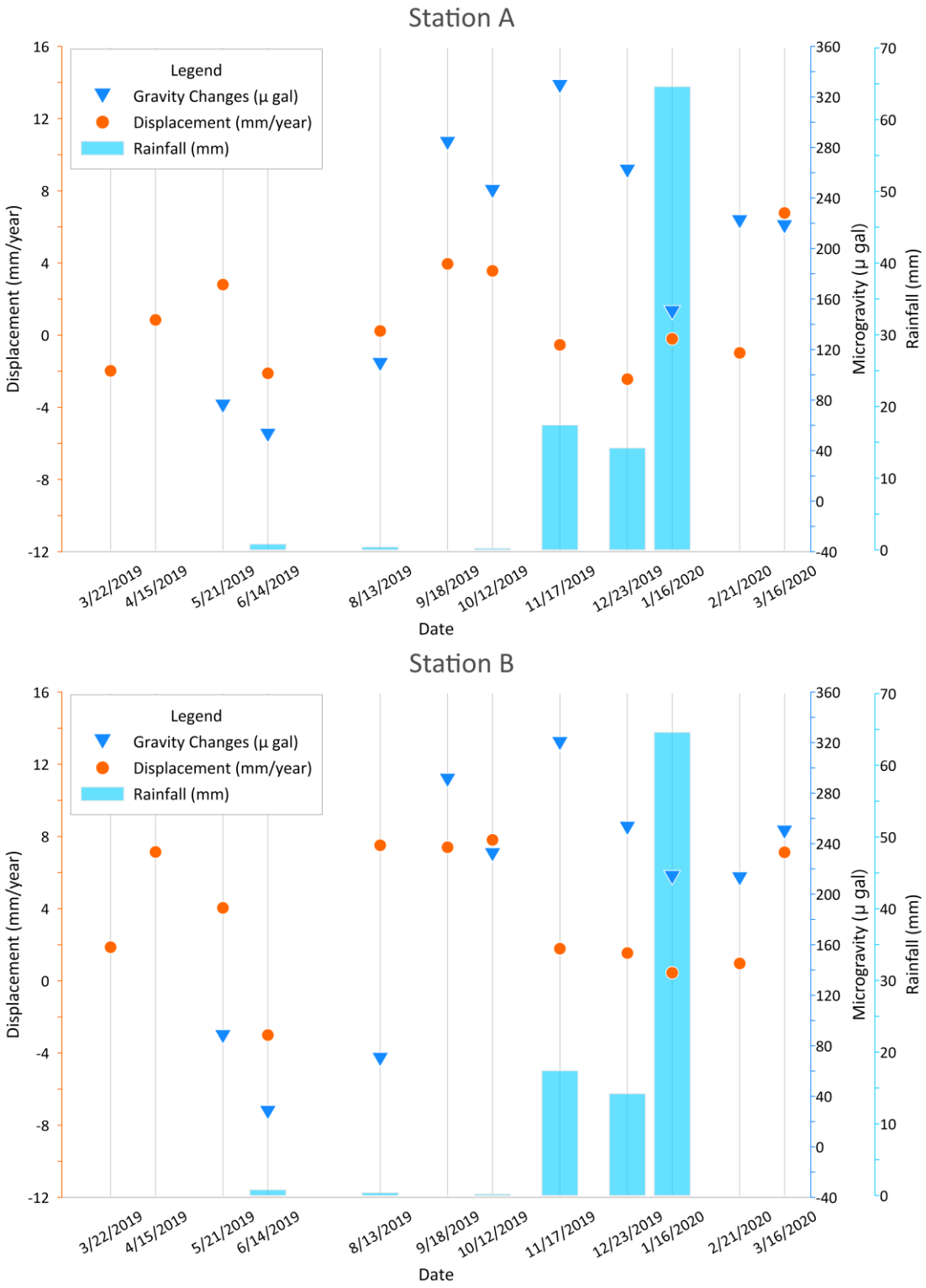

Figure 5.9: TLMG anomalies, LOS deformations, and precipitation are shown in the graph in blue triangles, orange circles, and light blue bars, respectively, for the gravity sites.

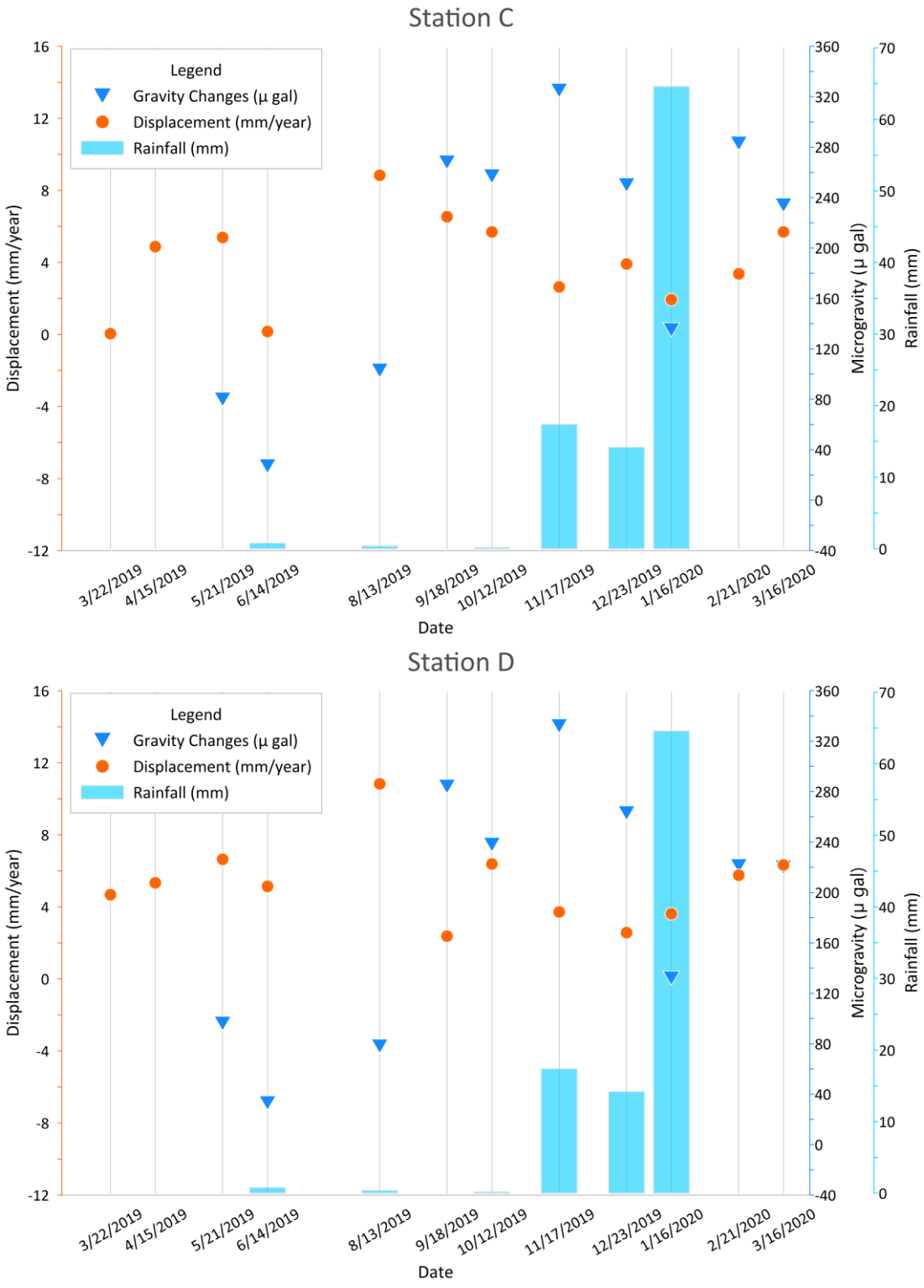

Figure 5.9: TLMG anomalies, LOS deformations, and precipitation are shown in the graph in blue triangles, orange circles, and light blue bars, respectively, for the gravity sites. (Continuted)

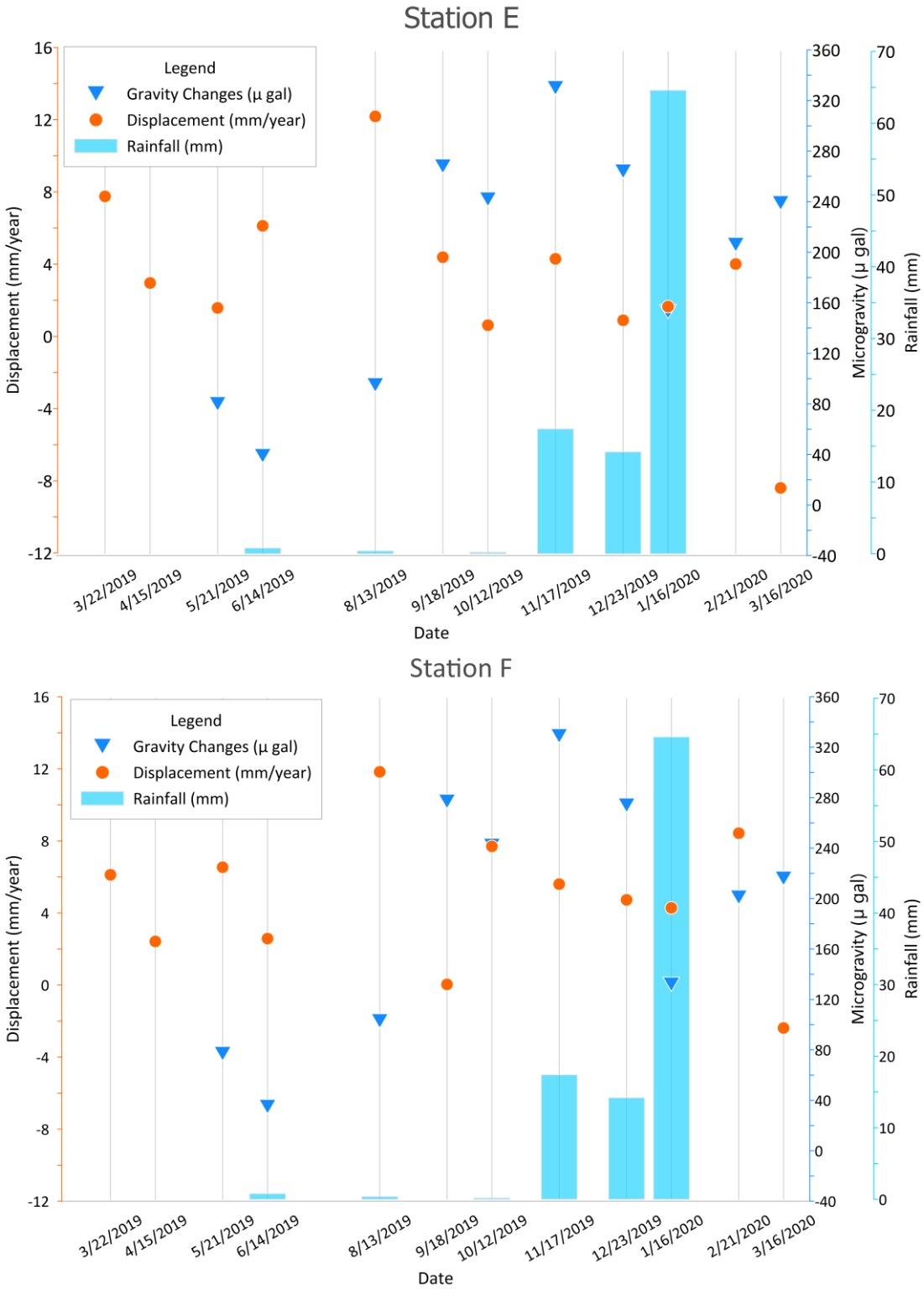

Figure 5.9: TLMG anomalies, LOS deformations, and precipitation are shown in the graph in blue triangles, orange circles, and light blue bars, respectively, for the gravity sites. (Continuted)

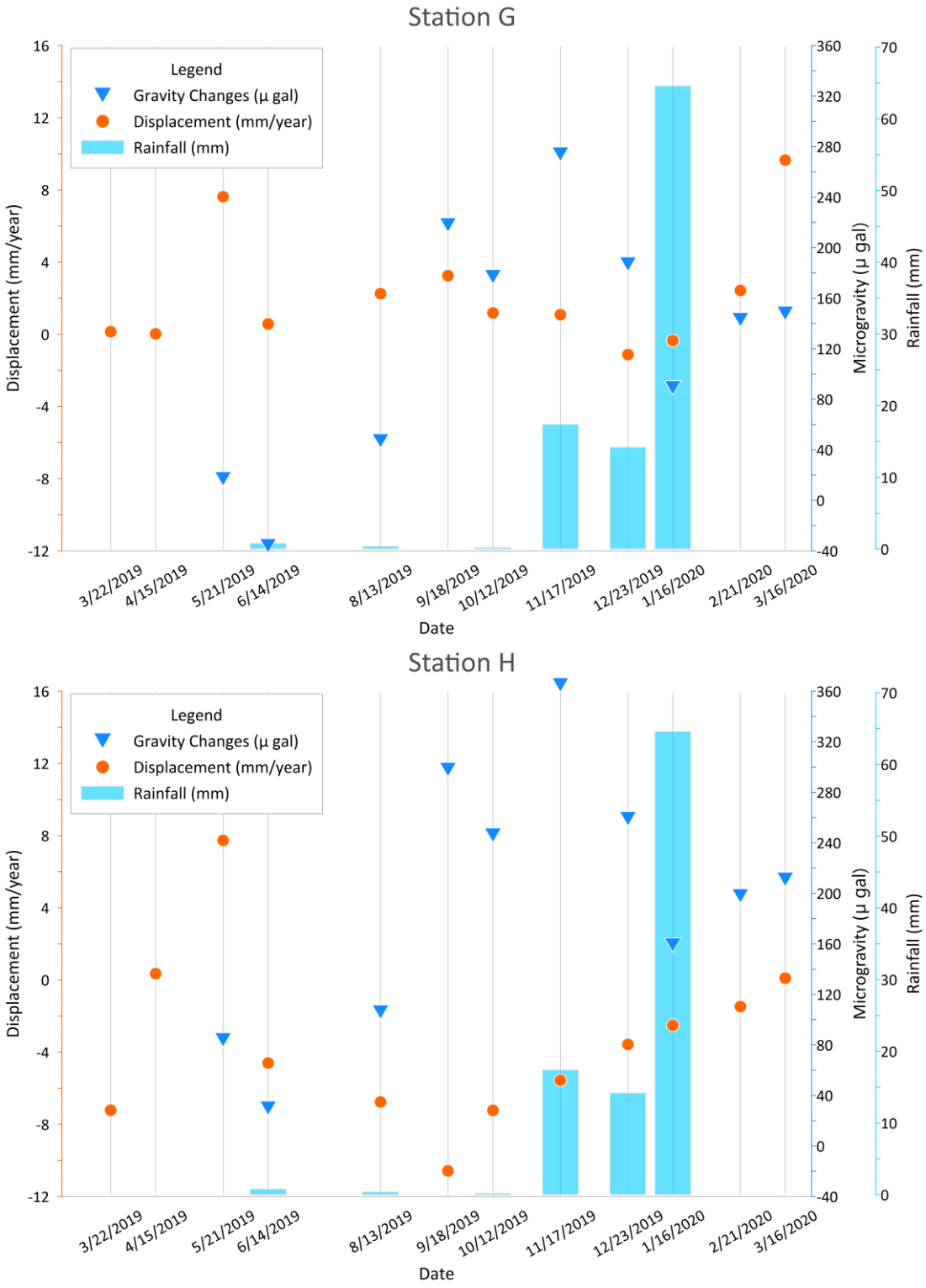

Figure 5.9: TLMG anomalies, LOS deformations, and precipitation are shown in the graph in blue triangles, orange circles, and light blue bars, respectively, for the gravity sites. (Continuted)

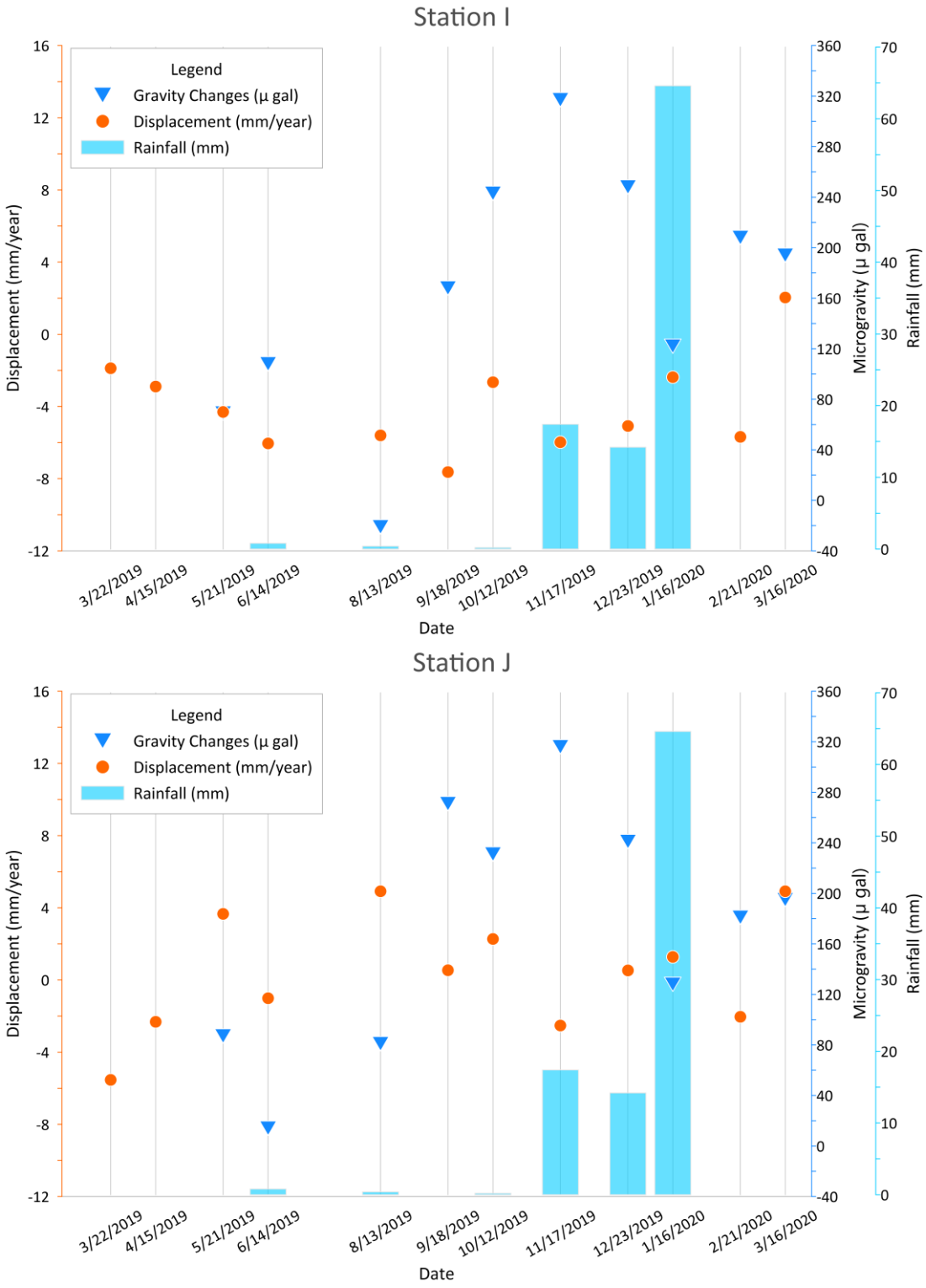

Figure 5.9: TLMG anomalies, LOS deformations, and precipitation are shown in the graph in blue triangles, orange circles, and light blue bars, respectively, for the gravity sites. (Continuted)

Chapter 6: Conclusion

Land surface deformations analysis has been exploited over the whole UAE using the interferometric processing of the massive available Sentinel-1 SAR dataset in the period between March 2017 and March 2021. UAE is characterized geomorphologically by flat barren along the coastline, sand dunes over most of the country with flat areas in between known as interdunes, and mountains in the east and northeast. The exploited InSAR processing for the first time over the whole UAE showed a regional land surface subsidence over the Al Ain and Al Dhafra regions, in Abu Dhabi Emirate, with smaller land surface subsidence in the Northern Emirates. The implemented approach of InSAR parallelism showed a significant reduction in time-consuming for the overall procedure from pre-processing of the SLC SAR image to obtain the final land surface displacement map. Also, big InSAR data processing was implemented by processing 291 Sentinel-1 SAR datasets for the whole UAE divided into three different frames.

The extensive land surface subsidence cases were detected over the Remah and Al Wagan areas. These areas are cultivated land farmed for growing fruits and vegetable crops using greenhouses. The time-series for the land surface deformations were correlated with the water level measurements at the nearby wells. The detected subsidence region from the interferometry processing was found in coincidence with the spatial distribution of the irrigated farms. This correlation supports the hypothesis that groundwater overexploitation is the main driving mechanism for land surface subsidence. The detected land surface subsidence cases have been confirmed with the ground truth data of groundwater level data and field observations for constructions failures and deformations.

A gravity geophysical survey has been conducted over Al Ain city to study the seasonal subsurface change between March 2019 and March 2020. InSAR processing has been exploited over the same area within the same time frame to integrate both satellite and geophysical measurements. This integration showed an agreement between the two measurements over some locations. Geophysical measurements contain signals related to surface and subsurface changes whereas InSAR measurements can be utilized to separate these signals with the help of water level data.

With the shortage of some data as geotechnical and pumping test data, estimating seasonal deformations and determining which layers control the subsidence was unfeasible. Nevertheless, this study provides a valuable tool for integrating groundwater level measurements with SAR interferometry measurement to monitor the environmental impacts of groundwater overexploitation and implement an essential tool to control groundwater abstraction.

Future research will focus on the following points

- Gathering the missing data either from local agencies or by field data collection. These data will help to build a geomechanical model that can generate different scenarios for groundwater exploitation and the impact on surface and subsurface structure.
- Investigating the aquifer compaction over the agricultural areas will complete the model and guide the practices for groundwater abstraction to avoid depleting the aquifer.

- Investigate land surface subsidence within cities using other SAR data with smaller wavelengths such as X-band to study the smaller displacement over constructions.
- Deep investigation over the detected land surface subsidence over the Al Dhafra region where there is no available in-situ information for these subsidence zones.

References

ADAFSA. (2019). Statistical Year Book. Retrieved from Abu Dhabi, United Arab Emirates: https://www.adfca.ae/arabic/mediacenter/publications/pages/mta.aspx

Allis, R. G., and Hunt, T. M. (1986). Analysis of exploitation-induced gravity changes at Wairakei Geothermal Field. *Geophysics, 51*(8), 1647-1660. doi:10.1190/1.1442214

Amighpey, M., & Arabi, S. (2016). Studying land subsidence in Yazd province, Iran, by integration of InSAR and levelling measurements. *Remote Sensing Applications: Society and Environment, 4*, 1-8.

Anantrasirichai, N., Biggs, J., Albino, F., & Bull, D. (2019). A deep learning approach to detecting volcano deformation from satellite imagery using synthetic datasets. *Remote Sensing of Environment, 230*, 111179.

Anantrasirichai, N., Biggs, J., Albino, F., Hill, P., & Bull, D. (2018). Application of Machine Learning to Classification of Volcanic Deformation in Routinely Generated InSAR Data. *Journal of Geophysical Research: Solid Earth, 123*(8), 6592-6606. doi:https://doi.org/10.1029/2018JB015911

Aslan, G., Cakir, Z., Ergintav, S., Lasserre, C., & Renard, F. (2018). Analysis of secular ground motions in istanbul from a long-term InSAR time-series (1992-2017). *Remote Sensing, 10*(3), 408-425. doi:10.3390/rs10030408

Baek, W.-K., Jung, H.-S., & Chae, S.-H. (2018). Feasibility of ALOS2 PALSAR2 Offset-Based Phase Unwrapping of SAR Interferogram in Large and Complex Surface Deformations. *IEEE Access, 6*, 45951-45960.

Bai, L., Jiang, L., Wang, C., & Sun, Q. (2016). Spatiotemporal Characterization of Land Subsidence and Uplift (2009–2010) over Wuhan in Central China Revealed by TerraSAR-X InSAR Analysis. *Remote Sensing, 8*(4), 350-363. doi:10.3390/rs8040350

Bakon, M., Oliveira, I., Perissin, D., Sousa, J. J., & Papco, J. (2017). A Data Mining Approach for Multivariate Outlier Detection in Postprocessing of Multitemporal InSAR Results. *IEEE Journal of Selected Topics in Applied Earth Observations and Remote Sensing, 10*(6), 2791-2798. doi:10.1109/JSTARS.2017.2686646

Baumann, P., Misev, D., Merticariu, V., & Huu, B. P. (2019). Datacubes: Towards space/time analysis-ready data. In *Service-oriented mapping* (pp. 269-299): Springer.

Baumann, P., Rossi, A. P., Bell, B., Clements, O., Evans, B., Hoenig, H., . . . Wagemann, J. (2018). Fostering Cross-Disciplinary Earth Science Through Datacube Analytics. In P.-P. Mathieu & C. Aubrecht (Eds.), *Earth Observation Open Science and Innovation* (pp. 91-119). Cham: Springer International Publishing.

Baumhoer, C. A., Dietz, A. J., Dech, S., & Kuenzer, C. (2018). Remote sensing of antarctic glacier and ice-shelf front dynamics—A review. *Remote Sensing, 10*(9), 1445.

Bekaert, D. P. S., Walters, R. J., Wright, T. J., Hooper, A. J., & Parker, D. J. (2015). Statistical comparison of InSAR tropospheric correction techniques. *Remote Sensing of Environment, 170*, 40-47. doi:https://doi.org/10.1016/j.rse.2015.08.035

Berardino, P., Fornaro, G., Lanari, R., & Sansosti, E. (2002). A new algorithm for surface deformation monitoring based on small baseline differential SAR interferograms. *IEEE Transactions on Geoscience and Remote Sensing, 40*(11), 2375-2383. doi:https://doi.org/10.1109/TGRS.2002.803792

Biggs, J., Wright, T., Lu, Z., & Parsons, B. (2007). Multi-interferogram method for measuring interseismic deformation: Denali Fault, Alaska. *Geophysical Journal International, 170*(3), 1165-1179. doi:10.1111/j.1365-246X.2007.03415.x

Bikeeva, L., Safarov, Z. K., Yuldasheva, M., Akramova, N., & Umarov, S. A. (2021). *Integrated geological interpretation of remote sensing data (Boysun structural-tectonic zone).* Paper presented at the IOP Conference Series: Earth and Environmental Science.

Calò, F., Abdikan, S., Görüm, T., Pepe, A., Kiliç, H., & Şanli, F. B. (2015). The Space-Borne SBAS-DInSAR Technique as a Supporting Tool for Sustainable Urban Policies: The Case of Istanbul Megacity, Turkey. *Remote Sensing, 7*, 16519-16536.

Calò, F., Ardizzone, F., Castaldo, R., Lollino, P., Tizzani, P., Guzzetti, F., . . . Manunta, M. (2014). Enhanced landslide investigations through advanced DInSAR techniques: The Ivancich case study, Assisi, Italy. *Remote Sensing of Environment, 142*, 69-82. doi:10.1016/j.rse.2013.11.003

Castellazzi, P., Longuevergne, L., Martel, R., Rivera, A., Brouard, C., & Chaussard, E. (2018). Quantitative mapping of groundwater depletion at the water management scale using a combined GRACE/InSAR approach. *Remote Sensing of Environment, 205*, 408-418. doi:10.1016/j.rse.2017.11.025

Casu, F., Elefante, S., Imperatore, P., Zinno, I., Manunta, M., Luca, C. D., & Lanari, R. (2014). SBAS-DInSAR Parallel Processing for Deformation Time-Series Computation. *IEEE Journal of Selected Topics in Applied Earth Observations and Remote Sensing, 7*(8), 3285-3296. doi:10.1109/JSTARS.2014.2322671

Chang, L., Ku, O., & Hanssen, R. F. (2018). Identification of deformation pattern changes caused by enhanced oil recovery (EOR) using InSAR. *International Journal of Remote Sensing*. doi:10.1080/01431161.2018.1526426

Chaussard, E., Wdowinski, S., Cabral-Cano, E., & Amelung, F. (2014). Land subsidence in central Mexico detected by ALOS InSAR time-series. *Remote Sensing of Environment, 140*, 94-106.

Chen, B., Gong, H., Chen, Y., Li, X., Zhou, C., Lei, K., . . . Zhao, X. (2020). Land subsidence and its relation with groundwater aquifers in Beijing Plain of China. *Science of The Total Environment*, 139111. doi:https://doi.org/10.1016/j.scitotenv.2020.139111

Chet, K. V., Siong, L. C., Hsin, W. H. H., Wei, L. L., Guey, C. W., Yam, C. M., . . . Kit, C. Y. (2015). *Ku-band ground-based SAR experiments for surface deformation monitoring*. Paper presented at the IEEE 5th Asia-Pacific Conference on Synthetic Aperture Radar (APSAR), , Singapore.

Costantini, M., Ferretti, A., Minati, F., Falco, S., Trillo, F., Colombo, D., . . . Costabile, S. (2017). Analysis of surface deformations over the whole Italian territory by interferometric processing of ERS, Envisat and COSMO-SkyMed radar data. *Remote Sensing of Environment, 202*, 250-275. doi:https://doi.org/10.1016/j.rse.2017.07.017

Costantini, M., Minati, F., Ciminelli, M. G., Ferretti, A., & Costabile, S. (2015). Nationwide ground deformation monitoring by persistent scatterer interferometry. *IEEE International Geoscience and Remote Sensing Symposium (IGARSS)*, 1472-1475.

De Luca, C., Cuccu, R., Elefante, S., Zinno, I., Manunta, M., Casola, V., . . . Casu, F. (2015). An On-Demand Web Tool for the Unsupervised Retrieval of Earth's Surface Deformation from SAR Data: The P-SBAS Service within the ESA G-POD Environment. *Remote Sensing, 7*(11). doi:10.3390/rs71115630

Dehls, J. F., Larsen, Y., Marinkovic, P., Lauknes, T. R., Stødle, D., & Moldestad, D. A. (2019, 28 July-2 Aug. 2019). *INSAR.No: A National Insar Deformation Mapping/Monitoring Service In Norway -- From Concept To Operations.* Paper presented at the IGARSS 2019 - 2019 IEEE International Geoscience and Remote Sensing Symposium.

Dhu, T., Dunn, B., Lewis, B., Lymburner, L., Mueller, N., Telfer, E., . . . Phillips, C. (2017). Digital earth Australia – unlocking new value from earth observation data. *Big Earth Data, 1*(1-2), 64-74. doi:10.1080/20964471.2017.1402490

Dong, J., Zhang, L., Liao, M., & Gong, J. (2019). Improved correction of seasonal tropospheric delay in InSAR observations for landslide deformation monitoring. *Remote Sensing of Environment, 233*, 111370. doi:https://doi.org/10.1016/j.rse.2019.111370

Dong, J., Zhang, L., Tang, M., Liao, M., Xu, Q., Gong, J., & Ao, M. (2018). Mapping landslide surface displacements with time series SAR interferometry by combining persistent and distributed scatterers: A case study of Jiaju landslide in Danba, China. *Remote Sensing of Environment, 205*, 180-198.

Dong, S., Samsonov, S., Yin, H., Ye, S., & Cao, Y. (2014). Time-series analysis of subsidence associated with rapid urbanization in Shanghai, China measured with SBAS InSAR method. *Environmental Earth Sciences, 72*(3), 677-691.

Dwivedi, R., Narayan, A. B., Tiwari, A., Singh, A. K., & Dikshit, O. (2017). Optimal estimation of interferometric phase for measuring surface deformation. *International Journal of Remote Sensing, 38*(5), 1339-1349. doi:10.1080/01431161.2017.1280627

EAD. (2018). *Groundwater Atlas of Abu Dhabi Emirate; Groundwater Wells Inventory and Soil Salinity Mapping of Abu Dhabi Emirate Project*. Retrieved from Abu Dhabi, United Arab Emirates:

El-Sayed, M. I. (1999). Sedimentological characteristics and morphology of the aeolian sand dunes in the eastern part of the UAE, a case study from Ar Rub' Al Khali. *Sedimentary Geology, 123*(3), 219-238. doi:https://doi.org/10.1016/S0037-0738(98)00116-X

El Jazouli, A., Barakat, A., Khellouk, R., Rais, J., & El Baghdadi, M. (2019). Remote sensing and GIS techniques for prediction of land use land cover change effects on soil erosion in the high basin of the Oum Er Rbia River (Morocco). *Remote Sensing Applications: Society Environmental Earth Sciences, 13*, 361-374.

El Tokhi, M., Arman, H., Abdelghany, O., Hashem, W., & El Saiy, A. (2012). Isotope Stratigraphy of Oligocene Limestone in Al-Ain City, United Arab Emirates. *Arabian Journal for Science and Engineering, 37*(5), 1439-1449. doi:10.1007/s13369-012-0253-y

Elmahdy, S. I., & Mohamed, M. M. (2015). Groundwater of Abu Dhabi Emirate: a regional assessment by means of remote sensing and geographic information system. *Arabian Journal of Geosciences, 8*(12), 11279-11292. doi:10.1007/s12517-015-1932-2

Embabi, N. S., Yahia, M. A., & Al Sharhan, A. S. (Cartographer). (1993). The national atlas of the United Arab Emirates

Euillades, L. D., Euillades, P. A., Riveros, N. C., Masiokas, M. H., Ruiz, L., Pitte, P., . . . Balbarani, S. (2016). Detection of glaciers displacement time-series using SAR. *Remote Sensing of Environment, 184*, 188-198. doi:10.1016/j.rse.2016.07.003

Fang, W., Huang, S., Huang, Q., Huang, G., Wang, H., Leng, G., . . . Guo, Y. (2019). Probabilistic assessment of remote sensing-based terrestrial vegetation vulnerability to drought stress of the Loess Plateau in China. *Remote Sensing of Environment, 232*, 111290.

Fattahi, H., Agram, P., & Simons, M. (2017). A Network-Based Enhanced Spectral Diversity Approach for TOPS Time-Series Analysis. *IEEE Transactions on Geoscience and Remote Sensing, 55*(2), 777-786. doi:10.1109/TGRS.2016.2614925

Feng, S., Chen, Q., Gu, G., Tao, T., Zhang, L., Hu, Y., . . . Zuo, C. (2019). Fringe pattern analysis using deep learning. *Advanced Photonics, 1*(2), 025001.

Ferretti, A., Fumagalli, A., Novali, F., Prati, C., Rocca, F., & Rucci, A. (2011). A New Algorithm for Processing Interferometric Data-Stacks: SqueeSAR. *IEEE Transactions on Geoscience and Remote Sensing, 49*(9), 3460-3470. doi:https://doi.org/10.1109/TGRS.2011.2124465

Ferretti, A., Prati, C., & Rocca, F. (2001). Permanent scatterers in SAR interferometry. *IEEE Transactions on Geoscience and Remote Sensing, 39*(2), 8–20. doi:https://doi.org/10.1109/36.898661

Fokker, P., Wassing, B., Van Leijen, F., Hanssen, R., & Nieuwland, D. (2016). Application of an ensemble smoother with multiple data assimilation to the Bergermeer gas field, using PS-InSAR. *Geomechanics for Energy the Environment, 5*, 16-28.

Frutuoso, R., Lima, A., & Teodoro, A. C. (2021). Application of remote sensing data in gold exploration: Targeting hydrothermal alteration using Landsat 8 imagery in northern Portugal. *Arabian Journal of Geosciences, 14*(6), 1-18.

Galloway, D. L., & Burbey, T. J. (2011). Review: Regional land subsidence accompanying groundwater extraction. *Hydrogeology Journal, 19*(8), 1459-1486. doi:https://doi.org/10.1007/s10040-011-0775-5

Gama, F. F., Cantone, A., Mura, J. C., Pasquali, P., Paradella, W. R., Santos A. R., & Silva, G. G. (2017). Monitoring subsidence of open pit iron mines at Carajأ،s Province based on SBAS interferometric technique using TerraSAR-X data. *Remote Sensing Applications: Society and Environment, 8*, 211-219.

Giuliani, G., Chatenoux, B., De Bono, A., Rodila, D., Richard, J.-P., Allenbach, K., . . . Peduzzi, P. (2017). Building an Earth Observations Data Cube: lessons learned from the Swiss Data Cube (SDC) on generating Analysis Ready Data (ARD). *Big Earth Data, 1*(1-2), 100-117. doi:10.1080/20964471.2017.1398903

Gonnuru, P., & Kumar, S. (2018). PsInSAR based land subsidence estimation of Burgan oil field using TerraSAR-X data. *Remote Sensing Applications: Society and Environment, 9*, 17-25.

Haarpaintner, J., Killough, B., Ofori-Ampofo, S., & Boamah, E. (2018). *Advanced sentinel-1 analysis ready data for the ghana open data cube and environmental monitoring.* Paper presented at the Proceedings of the International Workshop on Retrieval of Bio-& Geo-physical Parameters from SAR Data for Land Applications, Oberpfaffenhofen, Germany.

Haghighi, M. H., & Motagh, M. (2019). Ground surface response to continuous compaction of aquifer system in Tehran, Iran: Results from a long-term multi-sensor InSAR analysis. *Remote Sensing of Environment, 221*, 534-550.

Haghshenas Haghighi, M., & Motagh, M. (2017). Sentinel-1 InSAR over Germany: Large-scale interferometry, atmospheric effects, and ground deformation mapping. *ZFV - Zeitschrift fur Geodasie, Geoinformation und Landmanagement, 142*, 245-256. doi:10.12902/zfv-0174-2017

He, Y., Wang, W., Yan, H., Zhang, L., Chen, Y., & Yang, S. (2020). Characteristics of surface deformation in Lanzhou with Sentinel-1A TOPS. *Geosciences Journal, 10*(3), 99.

Holzer, T. L., & Galloway, D. L. J. H. a. g. a. (2005). Impacts of land subsidence caused by withdrawal of underground fluids in the United States. *16*, 87-99.

Hooper, A. (2008). A multi-temporal InSAR method incorporating both persistent scatterer and small baseline approaches. *Geophysical Research Letters, 35, 2008 ; doi:10.1029/2008GL034654, 35*. doi:https://doi.org/10.1029/2008GL034654

Hooper, A., Segall, P., & Zebker, H. (2007). Persistent scatterer interferometric synthetic aperture radar for crustal deformation analysis, with application to Volcán Alcedo, Galápagos. *Journal of Geophysical Research: Solid Earth, 112*(B7). doi:https://doi.org/10.1029/2006jb004763

Hooper, A., & Zebker, H. (2007). Phase unwrapping in three dimensions with application to InSAR time series. *Journal of the Optical Society of America A, 24*(9), 2737-2747. doi:10.1364/JOSAA.24.002737

Hooper, A., Zebker, H., Segall, P., & Kampes, B. (2004). A new method for measuring deformation on Volcanoes and other natural terrains using InSAR Persistent Scatterers. *Geophyiscal Research Letters, 31*, 1-5. doi:https://doi.org/10.1029/2004GL021737

Horst, T. v. d., Rutten, M. M., Giesen, N. C. v. d., & Hanssen, R. F. (2018). Monitoring land subsidence in Yangon, Myanmar using Sentinel-1 persistent scatterer interferometry and assessment of driving mechanisms. *Remote Sensing of Environment, 217*, 101-110.

Hue, J., Ding, X. L., Zhang, L., Sun, Q., Li, Z. W., Zhu, J., & Lu, Z. (2017). Estimation of 3-D Surface Displacement Based on InSAR and Deformation Modeling. *IEEE Transactions on Geoscience and Remote Sensing, 55*(4), 2007-2016.

Imamoglu, M., Kahraman, F., Cakir, Z., & Sanli, F. B. (2019). Ground deformation analysis of Bolvadin (W. Turkey) by means of multi-temporal InSAR techniques and Sentinel-1 data. *Remote Sensing, 11*(9), 1069.

Jo, M.-J., Jung, H.-S., & Won, J.-S. (2017). Measurement of precise three-dimensional volcanic deformations via TerraSAR-X synthetic aperture radar interferometry. *Remote Sensing of Environment, 192*, 228-237. doi:10.1016/j.rse.2017.02.022

Kadir, W. G. A., Santoso, D., & Alawiyah, S. (2007). Principle and Application of 4D Microgravity Survey for Engineering Purpose, Case Example: Groundwater Level Lowering and Subsidence in Residential Area of Jakarta. In *Symposium on the Application of Geophysics to Engineering and Environmental Problems 2007* (pp. 378-386): Environment and Engineering Geophysical Society.

Khan, Q., Kalbus, E., Alshamsi, M. D., Mohamed, M. M., & Liaqat, U. M. (2019). Hydrochemical Analysis of Groundwater in Remah and Al Khatim Regions, United Arab Emirates. *Hydrology, 6*(3). doi:https://doi.org/10.3390/hydrology6030060

Killough, B. (2018, 22-27 July 2018). *Overview of the Open Data Cube Initiative.* Paper presented at the IGARSS 2018 - 2018 IEEE International Geoscience and Remote Sensing Symposium.

Kim, J.-s., Kim, D.-J., Kim, S.-W., Won, J.-S., & Moon, W. M. J. G. J. (2007). Monitoring of urban land surface subsidence using PSInSAR. *11*(1), 59-73.

Kimura, H. (2017). *Three-dimensional surface deformation mapping from multi-directional SAR interferograms*. Paper presented at the IEEE International Geoscience and Remote Sensing Symposium (IGARSS), Fort Worth, TX.

Koubarakis, M., Kyzirakos, K., Nikolaou, C., Garbis, G., Bereta, K., Dogani, R., . . . Michail, D. (2016). Managing Big, Linked, and Open Earth-Observation Data: Using the TELEIOS\/LEO software stack. *IEEE Geoscience and Remote Sensing Magazine, 4*(3), 23-37. doi:10.1109/MGRS.2016.2530410

Kureel, N., Sarup, J., Matin, S., Goswami, S., & Kureel, K. (2021). Modelling vegetation health and stress using hypersepctral remote sensing data. *Modeling Earth Systems Environment, Development Sustainability*, 1-16.

Lanari, R., Mora, O., Manunta, M., Mallorqui, J. J., Berardino, P., & Sansosti, E. (2004). A small-baseline approach for investigating deformations on full-resolution differential SAR interferograms. *IEEE Transactions on Geoscience and Remote Sensing, 42*(7), 1377-1386. doi:10.1109/TGRS.2004.828196

Lazecky, M., Comut, F. C., Bakon, M., Qin, Y., Perissin, D., Hatton, E., . . . Ustun, A. (2016). Concept of an Effective Sentinel-1 Satellite SAR Interferometry System. *Procedia Computer Science, 100*, 14-18. doi:https://doi.org/10.1016/j.procs.2016.09.118

Lewis, A., Oliver, S., Lymburner, L., Evans, B., Wyborn, L., Mueller, N., . . . Wang, L.-W. (2017). The Australian Geoscience Data Cube — Foundations and lessons learned. *Remote Sensing of Environment, 202*, 276-292. doi:https://doi.org/10.1016/j.rse.2017.03.015

Liang, L., Li, X., & Zheng, F. (2019). Spatio-temporal analysis of ice sheet snowmelt in Antarctica and Greenland using microwave radiometer data. *Remote Sensing, 11*(16), 1838.

Liosis, N., Marpu, P. R., Pavlopoulos, K., & Ouarda, T. B. M. J. (2018). Ground subsidence monitoring with SAR interferometry techniques in the rural area of Al Wagan, UAE. *Remote Sensing of Environment, 216*, 276-288.

Manunta, M., Luca, C. D., Zinno, I., Casu, F., Manzo, M., Bonano, M., . . . Lanari, R. (2019). The Parallel SBAS Approach for Sentinel-1 Interferometric Wide Swath Deformation Time-Series Generation: Algorithm Description and Products Quality Assessment. *IEEE Transactions on Geoscience and Remote Sensing, 57*(9), 6259-6281. doi:10.1109/TGRS.2019.2904912

Massonnet, D., Rossi, M., Carmona, C., Adragna, F., Peltzer, G., Feigl, K., & Rabaute, T. (1993). The displacement field of the Landers earthquake mapped by radar interferometry. *Nature, 364*(6433), 138-142. doi:10.1038/364138a0

Ministry of Energy. (2006). *Geology of the Al Ain 1:50 000 map sheet, 50-6, United Arab Emirates*. Abu Dhabi: Ministry of Energy, Department of Geology and Mineral Resources (UAE).

Mohamed, M. M. (2014). An integrated water resources management strategy for Al-Ain City, United Arab Emirates. *Proceedings of the International Association of Hydrological Sciences, 364*, 273-278. doi:https://doi.org/10.5194/piahs-364-273-2014

MohanRajan, S. N., Loganathan, A., & Manoharan, P. (2020). Survey on Land Use/Land Cover (LU/LC) change analysis in remote sensing and GIS environment: Techniques and Challenges. *Environmental Science Pollution Research, 27*(24), 29900-29926.

Murad, A. A., Nuaimi, H., & Hammadi, M. (2007). Comprehensive assessment of water resources in the United Arab Emirates (UAE). *Water Resources Management, 21*(9), 1449-1463. doi:http://dx.doi.org/10.1007/s11269-006-9093-4

Ng, A.-H., Ge, L., & Li, X. (2015). Assessments of land subsidence in the Gippsland Basin of Australia using ALOS PALSAR data. *Remote Sensing of Environment, 159*, 86-101.

Normand, J. C. L., & Heggy, E. (2015). InSAR Assessment of Surface Deformations in Urban Coastal Terrains Associated with Groundwater Dynamics. *IEEE Transactions on Geoscience and Remote Sensing, 53*(12), 6356-6371.

Olorunfemi, I. E., Fasinmirin, J. T., Olufayo, A. A., & Komolafe, A. A. (2020). GIS and remote sensing-based analysis of the impacts of land use/land cover change (LULCC) on the environmental sustainability of Ekiti State, southwestern Nigeria. *Environment, Development Sustainability, 22*(2), 661-692.

Othman, A. K. (2005). *Quantitative and Qualitative Assessment of Groundwater Resources in Al-Khatim Area, UAE.* (Master), United Arab Emirates University,

Papoutsis, I., Kontoes, C., Alatza, S., Apostolakis, A., & Loupasakis, C. (2020). InSAR Greece with Parallelized Persistent Scatterer Interferometry: A National Ground Motion Service for Big Copernicus Sentinel-1 Data. *Remote Sensing, 12*(19), 3207.

Papoutsis, I., Kontoes, C., & Paradissis, D. (2017). Multi-Stack Persistent Scatterer Interferometry Analysis in Wider Athens, Greece. *Remote Sensing, 9*(3). doi:https://doi.org/10.3390/rs9030276

Papoutsis, I., Papanikolaou, X., Floyd, M., Ji, K. H., Kontoes, C., Paradissis, D., & Zacharis, V. (2013). Mapping inflation at Santorini volcano, Greece, using GPS and InSAR. *Geophysical Research Letters, 40*(2), 267-272. doi:10.1029/2012gl054137

Pawluszek-Filipiak, K., & Borkowski, A. (2020). Integration of DInSAR and SBAS Techniques to determine mining-related deformations using sentinel-1 data: The case study of Rydułtowy mine in Poland. *Remote Sensing, 12*(2), 242.

Peng, M., Zhao, C., Zhang, Q., Lu, Z., & Li, Z. (2019). Research on spatiotemporal land deformation (2012–2018) over Xi'an, China, with multi-sensor SAR datasets. *Remote Sensing, 11*(6), 664.

Pepe, A., Solaro, G., Calo, F., & Dema, C. (2016). A Minimum Acceleration Approach for the Retrieval of Multiplatform InSAR Deformation Time Series. *IEEE Journal of Selected Topics in Applied Earth Observations and Remote Sensing, 9*(8), 3883-3898. doi:10.1109/jstars.2016.2577878

Pepe, S., De Siena, L., Barone, A., Castaldo, R., D'Auria, L., Manzo, M., . . . Tizzani, P. (2019). Volcanic structures investigation through SAR and seismic interferometric methods: The 2011–2013 Campi Flegrei unrest episode. *Remote Sensing of Environment, 234*, 111440. doi:https://doi.org/10.1016/j.rse.2019.111440

Petersen, L. K. (2018). Real-time prediction of crop yields from MODIS relative vegetation health: A continent-wide analysis of Africa. *Remote Sensing, 10*(11), 1726.

Plank, S. (2014). Rapid Damage Assessment by Means of Multi-Temporal SAR — A Comprehensive Review and Outlook to Sentinel-1. *Remote Sensing, 6*(6). doi:10.3390/rs6064870

Polcari, M., Montuori, A., Bignami, C., Moro, M., Stramondo, S., & Tolomei, C. (2017). Using multi-band InSAR data for detecting local deformation phenomena induced by the 2016–2017 Central Italy seismic sequence. *Remote Sensing of Environment, 201*, 234-242.

Qu, F., Lu, Z., Zhang, Q., Bawden, G. W., Kim, J. W., Zhao, C., & Qu, W. (2015). Mapping ground deformation over Houston-Galveston, Texas using multi-temporal InSAR. *Remote Sensing of Environment, 169*, 290-306. doi:10.1016/j.rse.2015.08.027

Qu, F., Zhang, Q., Lu, Z., Zhao, C., Yang, C., & Zhang, J. (2014). Land subsidence and ground fissures in Xi'an, China 2005–2012 revealed by multi-band InSAR time-series analysis. *Remote Sensing of Environment, 155*, 366-376.

Rajan Girija, R., & Mayappan, S. (2019). Mapping of mineral resources and lithological units: A review of remote sensing techniques. *International Journal of Image Data Fusion, 10*(2), 79-106.

Raucoules, D., Cartannaz, C., Mathieu, F., & Midot, D. (2013). Combined use of space-borne SAR interferometric techniques and ground-based measurements on a 0.3km2 subsidence phenomenon. *Remote Sensing of Environment, 139*, 331-339.

Raucoules, D., Michele, M. D., Malet, J., & Ulrich, P. (2013). Time-variable 3D ground displacements from high-resolution synthetic aperture radar (SAR). application to La Valette landslide (South French Alps). *Remote Sensing of Environment, 139*, 198-204. doi:10.1016/j.rse.2013.08.006

Reeves, J. A., Knight, R., & Zebker, H. A. (2014). An Analysis of the Uncertainty in InSAR Deformation Measurements for Groundwater Applications in Agricultural Areas. *IEEE Journal of Selected Topics in Applied Earth Observations and Remote Sensing, 7*(7), 2992-3001. doi:10.1109/jstars.2014.2322775

Rizk, Z. S., & Alsharhan, A. S. (2003). Water resources in the United Arab Emirates. In A. S. Alsharhan & W. W. Wood (Eds.), *Developments in Water Science* (Vol. 50, pp. 245-264): Elsevier.

Saibi, H. (2017). Microgravity and Its Applications in Geosciences. In T. Zouaghi (Ed.), *Gravity - Geoscience Applications, Industrial Technology and Quantum Aspect* (pp. 41-72): InTech.

Saibi, H., Amrouche, M., & Fowler, A.-R. (2019). Deep cavity systems detection in Al-Ain City, UAE, based on gravity surveys inversion. *Journal of Asian*

Earth Sciences, 182, 103937. doi:https://doi.org/10.1016/j.jseaes.2019.103937

Sansosti, E., Berardino, P., Bonano, M., Calò, F., Castaldo, R., Casu, F., . . . Lanari R. (2014). How second generation SAR systems are impacting the analysis of ground deformation. *International Journal of Applied Earth Observation and Geoinformation, 28*, 1-11. doi:10.1016/j.jag.2013.10.007

Santoso, D., Kadir, W. G. A., Alawiyah, S., Setianingsih, Wahyudi, E. J., Sarkowi, M., & Sarkowi, M. (2011). Understanding the Time-Lapse Microgravity Response due to Subsidence and Groundwater Level Lowering. In *The Contributing of Geosciences to Human Security* (pp. 27-48). Deutscehe Nationalbiblithek, Berlin.

Sasgen, I., Konrad, H., Helm, V., & Grosfeld, K. (2019). High-resolution mass trends of the Antarctic ice sheet through a spectral combination of satellite gravimetry and radar altimetry observations. *Remote Sensing, 11*(2), 144.

Scifoni, S., Bonano, M., Marsella, M., Sonnessa, A., Tagliafierro, V., Manunta, M., . . . Sciotti, M. (2016). On the joint exploitation of long-term DInSAR time series and geological information for the investigation of ground settlements in the town of Roma (Italy). *Remote Sensing of Environment, 182*, 113-127.

Scintrex. (2018). *CG-6 Autograv Gravity Meter Operation Manual - P/N 115370001*. Concord, Canda: Scintrex Ltd.

SEWA. (2018). *Annual Statistical Report*. Retrieved from Sharjah, United Arab Emirates:

Short, N., Leblanc, A.-M., Sladen, W., Oldenborger, G., Mathon-Dufour, V., & Brisco, B. (2014). RADARSAT-2 D-InSAR for ground displacement in permafrost terrain, validation from Iqaluit Airport, Baffin Island, Canada. *Remote Sensing of Environment, 141*, 40-51.

Singhroy, V., & Li, J. (2015, 26-31 July 2015). *InSAR deformation monitoring of the Canadian oil sands from RADARSAT 2 and COSMO SkyMed images.* Paper presented at the 2015 IEEE International Geoscience and Remote Sensing Symposium (IGARSS).

Singhroy, V., Li, J., Samsonov, S., Shen, L., & Pearse, J. (2014, 13-18 July 2014). *InSAR monitoring of surface deformation induced by steam injection in the Athabasca oil sands, Canada.* Paper presented at the 2014 IEEE Geoscience and Remote Sensing Symposium.

Soenen, S. (2019). Deep Learning and SAR Applications A short overview of advancements and challenges in earth observation applications. *Towards Data Science*.

Spoorthi, G., Gorthi, S., & Gorthi, R. (2018). PhaseNet: A deep convolutional neural network for two-dimensional phase unwrapping. *IEEE Signal Processing Letters, 26*(1), 54-58.

Staniewicz, S., Chen, J., Lee, H., Olson, J., Savvaidis, A., Reedy, R., . . . Hennings, P. (2020). InSAR Reveals Complex Surface Deformation Patterns Over an 80,000 km2 Oil-Producing Region in the Permian Basin. *Geophysical Research Letters, 47*(21), e2020GL090151.

Strozzi, T., Antonova, S., Günther, F., Mätzler, E., Vieira, G., Wegmüller, U., . . . Bartsch, A. (2018). Sentinel-1 SAR Interferometry for Surface Deformation Monitoring in Low-Land Permafrost Areas. *Remote Sensing, 10*. doi:10.3390/rs10091360

Strozzi, T., Klimeš, J., Frey, H., Caduff, R., Huggel, C., Wegmüller, U., & Rapr, A. C. (2018). Satellite SAR interferometry for the improved assessment of the state of activity of landslides: A case study from the Cordilleras of Peru. *Remote Sensing of Environment, 217*, 111-125.

Svigkas, N., Papoutsis, I., Loupasakis, C., Tsangaratos, P., Kiratzi, A., & Kontoes, C. H. (2017). InSAR time-series monitoring of ground displacement trends in an industrial area (Oreokastro—Thessaloniki, Greece): detection of natural surface rebound and new tectonic insights. *Environmental Earth Sciences, 76*(5), 195. doi:https://doi.org/10.1007/s12665-017-6517-9

Tamm, T., Zalite, K., Voormansik, K., & Talgre, L. (2016). Relating Sentinel-1 Interferometric Coherence to Mowing Events on Grasslands. *Remote Sensing, 8*(10). doi:10.3390/rs8100802

Tao, L., Zhang, H., Wang, C., & Tang, Y. (2012). Ground deformation retrieval using quasi coherent targets DInSAR, with application to suburban area of Tianjin, China. *IEEE Journal of Selected Topics in Applied Earth Observations and Remote Sensing, 5*(3), 867-873. doi:10.1109/JSTARS.2012.2189374

Taylor, C., & Alley, W. (2002). *Ground-Water-Level Monitoring and the Importance of Long-Term Water-Level Data*.

Thomas, R. J., Finlayson, A., Smith, R. A., Arkley, S. L. B., & Farrant, A. R. (2012). *Geology of the Sweihan and Remah 1:100 000 map sheet, 100-7, United Arab Emirates*. Nottingham, UK: British Geological Survey.

Ticehurst, C., Zhou, Z.-S., Lehmann, E., Yuan, F., Thankappan, M., Rosenqvist, A., . . . Paget, M. (2019). Building a SAR-Enabled Data Cube Capability in Australia Using SAR Analysis Ready Data. *Data, 4*(3). doi:10.3390/data4030100

Tong, X., & Schmidt, D. (2016). Active movement of the Cascade landslide complex in Washington from a coherence-based InSAR time series method. *Remote Sensing of Environment, 186*, 405-415. doi:10.1016/j.rse.2016.09.008

Torres, R., Snoeij, P., Geudtner, D., Bibby, D., Davidson, M., Attema, E., . . . Rostan, F. (2012). GMES Sentinel-1 mission. *Remote Sensing of Environment, 120*, 9-24. doi:https://doi.org/10.1016/j.rse.2011.05.028

Truckenbrodt, J., Freemantle, T., Williams, C., Jones, T., Small, D., Dubois, C., . . . Giuliani, G. (2019). Towards Sentinel-1 SAR Analysis-Ready Data: A Best Practices Assessment on Preparing Backscatter Data for the Cube. *Data, 4*(3). doi:10.3390/data4030093

Valade, S., Ley, A., Massimetti, F., D'Hondt, O., Laiolo, M., Coppola, D., . . . Walter, T. R. (2019). Towards Global Volcano Monitoring Using Multisensor Sentinel Missions and Artificial Intelligence: The MOUNTS Monitoring System. *Remote Sensing, 11*(13). doi:10.3390/rs11131528

Wei, M., & Sandwell, D. T. (2010). Decorrelation of L-Band and C-Band Interferometry Over Vegetated Areas in California. *IEEE Transactions on Geoscience and Remote Sensing, 48*(7), 2942-2952. doi:10.1109/tgrs.2010.2043442

Yagoub, M. M. (2015). Spatio-temporal and hazard mapping of Earthquake in UAE (1984–2012): Remote sensing and GIS application. *Geoenvironmental Disasters, 2*(1), 13. doi:https://doi.org/10.1186/s40677-015-0020-y

Yagüe-Martínez, N., Prats-Iraola, P., González, F. R., Brcic, R., Shau, R., Geudtner, D., . . . Bamler, R. (2016). Interferometric Processing of Sentinel-1 TOPS Data. *IEEE Transactions on Geoscience and Remote Sensing, 54*(4), 2220-2234. doi:10.1109/TGRS.2015.2497902

Yang, K., Yan, L., Huang, G., Chen, C., & Wu, Z. (2016). Monitoring Building Deformation with InSAR: Experiments and Validation. *Sensors, 16*(12). doi:10.3390/s16122182

Yu, C., Li, Z., & Penna, N. T. (2018). Interferometric synthetic aperture radar atmospheric correction using a GPS-based iterative tropospheric decomposition model. *Remote Sensing of Environment, 204*, 109-121. doi:https://doi.org/10.1016/j.rse.2017.10.038

Yu, L., Yang, T., Zhao, Q., Liu, M., & Pepe, A. (2017). The 2015–2016 Ground Displacements of the Shanghai Coastal Area Inferred from a Combined COSMO-SkyMed/Sentinel-1 DInSAR Analysis. *Remote Sensing, 9*(11), 1194-1212. doi:10.3390/rs9111194

Zektser, S., Loáiciga, H. A., & Wolf, J. T. (2005). Environmental impacts of groundwater overdraft: selected case studies in the southwestern United States. *Environmental Geology, 47*(3), 396-404. doi:https://doi.org/10.1007/s00254-004-1164-3

Zhang, R., Liu, G., Li, T., Huang, L., Yu, B., Chen, Q., & Li, Z. (2014). An Integrated Model for Extracting Surface Deformation Components by PSI Time Series. *IEEE Geoscience and Remote Sensing Letters, 11*(2), 544-548.

Zhang, T., Jiang, S., Zhao, Z., Dixit, K., Zhou, X., Hou, J., . . . Yan, C. (2019). Rapid and robust two-dimensional phase unwrapping via deep learning. *Optics Express, 27*(16), 23173-23185. doi:10.1364/OE.27.023173

Zhao, C., Liu, C., Zhang, Q., Lu, Z., & Yang, C. (2018). Deformation of Linfen-Yuncheng Basin (China) and its mechanisms revealed by Π-RATE InSAR technique. *Remote Sensing of Environment, 218*, 221–230. doi:10.1016/j.rse.2018.09.021

Zheng, M., Deng, K., Fan, H., & Du, S. (2018). Monitoring and analysis of surface deformation in mining area based on InSAR and GRACE. *Remote Sensing, 10*(9). doi:10.3390/rs10091392

Zhu, X. X., Tuia, D., Mou, L., Xia, G. S., Zhang, L., Xu, F., & Fraundorfer, F. (2017). Deep Learning in Remote Sensing: A Comprehensive Review and List of Resources. *IEEE Geoscience and Remote Sensing Magazine, 5*(4), 8-36. doi:10.1109/MGRS.2017.2762307

Zinno, I., Casu, F., Luca, C. D., Elefante, S., Lanari, R., & Manunta, M. (2017). A Cloud Computing Solution for the Efficient Implementation of the P-SBAS DInSAR Approach. *IEEE Journal of Selected Topics in Applied Earth Observations and Remote Sensing, 10*(3), 802-817. doi:10.1109/JSTARS.2016.2598397

Zinno, I., Elefante, S., Mossucca, L., Luca, C. D., Manunta, M., Terzo, O., . . . Casu, F. (2015). A First Assessment of the P-SBAS DInSAR Algorithm Performances Within a Cloud Computing Environment. *IEEE Journal of Selected Topics in Applied Earth Observations and Remote Sensing, 8*(10), 4675-4686. doi:10.1109/JSTARS.2015.2426054

Zinno, I., Mossucca, L., Elefante, S., Luca, C. D., Casola, V., Terzo, O., . . . Lanari, R. (2016). Cloud Computing for Earth Surface Deformation Analysis via Spaceborne Radar Imaging: A Case Study. *IEEE Transactions on Cloud Computing, 4*(1), 104-118. doi:10.1109/TCC.2015.2440267

List of Publications

El Kamali, M., Papoutsis, I., Loupasakis, C., Abuelgasim, A., Omari, K., and Kontoes, C., 2021. Monitoring of land surface subsidence using persistent scatterer interferometry techniques and ground truth data in arid and semi-arid regions, the case of Remah, UAE. Science of The Total Environment. 776, 145946. https://doi.org/10.1016/j.scitotenv.2021.145946

El Kamali & Yagoub (2020) - Transformation of a Village: Case of Wad Al Abbas, Sennar State, Sudan. Int. Arch. Photogramm. Remote Sens. Spatial Inf. Sci. XLIII-B3-2020, 1527-1531. https://doi.org/10.5194/isprs-archives-XLIII-B3-2020-1527-2020

El Kamali, M., Abuelgasim, A., Papoutsis, I., Loupasakis, C., and Kontoes, C., 2020. A reasoned bibliography on SAR interferometry applications and outlook on big interferometric data processing. Remote Sensing Applications: Society and Environment. 19, 100358. https://doi.org/10.1016/j.rsase.2020.100358

Saibi, H., Mia, M.B., Bierre, M., El Kamali, M., 2021. Application of remote sensing techniques to geothermal exploration at geothermal fields in the United Arab Emirates. 14 https://doi.org/10.3986/ac.v43i1.579

Abuelgasim, A., & El Kamali, M., Time-series analysis of groundwater levels using Geographic Information Systems in Al Ain region, in the UAE. Asian Conference on Remote Sensing, Daejeon, Korea.

UAEU

جامعة الإمارات العربية المتحدة
United Arab Emirates University

UAE UNIVERSITY DOCTORATE DISSERTATION NO. 2022:1

This dissertation shows a detailed study about land surface movement over the whole territory of the United Arab Emirates (UAE). This dissertation utilizes the radar remote sensing interferometry techniques to map land surface deformations over the UAE. The utilization of this technique showed that the main land surface deformation is the land subsidence and it has been located in five distinctive zones. These zones are considered extensive land subsidence due to their higher subsidence rate and extended for several kilometers. This study concluded that the land surface subsidence was occurred due to

Muhagir Elkamali received his PhD from the Department of Geography and Urban Sustainability, College of Humanities & Social Sciences at UAE University, UAE. He received his Master of GIS and Remote Sensing from the College of Geographical and Environmental Sciences, University of Khartoum, Sudan.

www.uaeu.ac.ae

Online publication of dissertation:
https://scholarworks.uaeu.ac.ae/etds/

جامعة الإمارات العربية المتحدة
United Arab Emirates University
UAEU
Mervat Al Waked
UAEU Libraries
DigitizationDepatment
United Arab Emirates

Digitally signed by Shrieen
DN: cn=Shrieen, o=United Arab Emirates University, ou=UAEU Library Digitizatio, email=shrieen@uaeu.ac.ae, c=AE
Date: 2022.06.06 10:10:19 +04'00'